RESERVOIR QUALITY CHARACTERIZATION OF THE LOWER JURASSIC STØ FORMATION IN THE SOUTHWESTERN BARENTS SEA

Role of Sedimentary and Diagenetic processes

Libanos Tesfau Girmay

Master Thesis: Petroleum Geology & Petroleum Geophysics Discipline

Department of Geosciences

Faculty of Mathematics and Natural Sciences

UNIVERSITY OF OSLO

01.12.2017

RESERVOIR QUALITY CHARACTERIZATION OF THE LOWER JURASSIC STØ FORMATION IN THE SOUTHWESTERN BARENTS SEA

Role of Sedimentary and Diagenetic processes

Libanos Tesfau Girmay

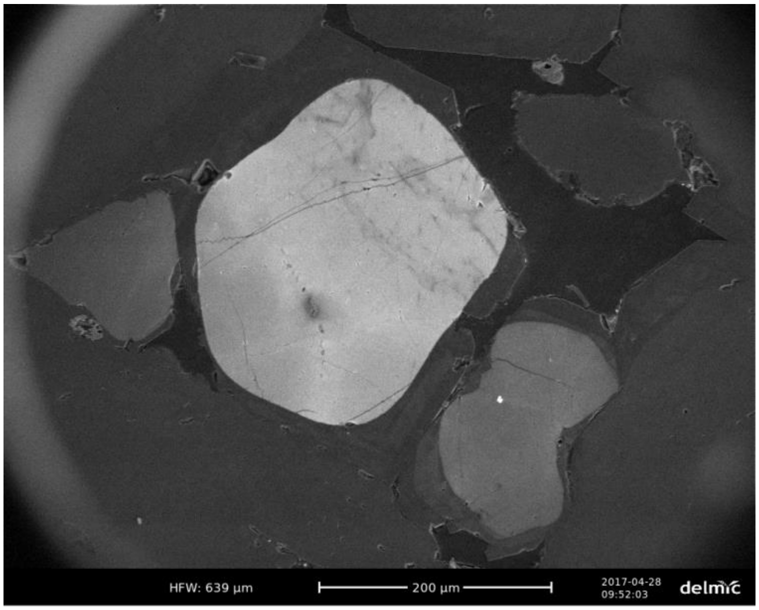

Master Thesis: Petroleum Geology & Petroleum Geophysics Discipline

Department of Geosciences

Faculty of Mathematics and Natural Sciences

UNIVERSITY OF OSLO

01.12.2017

2017

Reservoir quality characterization of the lower Jurassic Stø Formation in the southwestern Barents Sea

Libanos T. Girmay

http://www.duo.uio.no/

Press: Reprosentralen, University of Oslo

Acknowledgements

I wish to express my gratitude to the government of Norway for I was glad to have an opportunity to study in the University of Oslo under the quota scheme programme. I wish to thank the University of Oslo for all necessary data, materials, and facilities provided by, and to the Norwegian Petroleum Directorate Core Store (Stavanger) for I have access to the sediment core samples.

I would like to thank especially my supervisor Professor Jens Jahren and co-supervisor PhD student Beyene Girma Haile for the guidance and support throughout the development of this master thesis.

I wish to thank Berit Løken Berg for technical support and guidance in the SEM lab, Thanusha Naidoo in the XRD lab, and PhD student Lina Hedvig Line for the guidance and support during core logging.

I would like to appreciate fellow students in the department of Geosciences, and friends for sharing of ideas, discussions, and encourage me during the development of this thesis.

Finally yet importantly I want to thank my loving family who have helped me tirelessly and made me reach where I am today with the help of God.

30.11.2017

Libanos T. Girmay

ABSTRACT

The Norwegian Barents Sea is an emerging petroleum province in the Norwegian continental shelf since it has been opened partly for exploration in the 1979. Since then important discoveries has been made in the area such as Snøhvit gas field, and Goliat, Johan Castberg, Wisting central, and Gohta oil fields. The aim of this study is to characterize the reservoir quality of the lower Jurassic Stø Formation, which is the most important reservoir rock in the area. This study is based on two exploration wells: well 7119/9-1 (situated on the Ringvassøy-Loppa fault complex) and well 7119/12-2 (located on the Hammerfest basin) from the southwestern Barents Sea. The southwestern Barents Sea comprises petroleum-bearing Triassic to Jurassic potential reservoir quality sandstones deposited in varied depositional environments. The Lower Jurassic Stø Formation is one among these potential reservoir quality sandstones. This study therefore examined the reservoir quality of Stø Formation using data obtained from the two exploration wells. An integrated characterization approach including petrographic, sedimentological, x-ray diffraction, and petrophysical properties of the Stø sandstones were performed using drilled cores and geophysical well logs.

Three facies associations were recognized during the study of drill cores. Facies Association-1 is characterized by fine to medium-grained sand, mud and organic draped plane parallel and cross stratification structures, wavy mud drapes, and intermediate bioturbation in the finer intervals. It dominantly occurs in the lower sand unit of well 7119/12-2. Facies Association-2 is characterized by dominantly structureless, friable, lighter sand that occurs in the upper sand unit of well 7119/12-2. It is cemented, massive, containing conglomeratic lag in the top part of well 7119/9-1. Facies Association-3 is intercalation of strongly bioturbated, very fine, muddy sand with cemented, massive units, usually stylolitized at the interfaces. It occurs at the lower part of the upper sand unit in well 7119/9-1. Depositional environment of varying between high energy regimes of tidal influence, near shoreline surf zone, and proximal shore face suggested.

Petrographic study reveals that the Stø Formation is quartz arenitic in composition dominantly clean consisting of fine to medium grained and well-sorted sandstone. Petrography and petrophysical analyses integrated with sedimentological processes demonstrated that the reservoir quality of the Stø sandstone is mainly affected by mechanical compaction and quartz cementation. Best reservoir quality observed in the Stø Formation of well 7119/12-2 where

porosity ranges from 15 to 30% (av. of 22%). Only small amount of quartz cement was observed implying porosity is primarily reduced by mechanical compaction. Reservoir quality of the Stø Formation is significantly degraded in well 7119/9-1 where the average porosity is 10% and even lower. Quartz arenites of the Stø Formation in this well are heavily cemented by quartz and the degree of quartz cementation is the main control on reservoir properties compared to the sediments in well 7119/12-2. This suggests that the reservoir property of the Stø Formation in this well is primarily controlled by chemical compaction. This study strongly shows that although the primary textural and mineralogical sediment composition and depositional environment are correlatable in the two mentioned wells, the reservoir quality of the Stø Formation varies actually in these two wells. These differences are principally attributed to variations resulting from mechanical compaction and the degree of quartz cementation.

Contents

1 INTRODUCTION

1.1 Background and Motivation

The Norwegian continental shelf (Fig. 1.1) is home to many petroleum fields starting from the first discovery of the Ekofisk oil field in 1969. Production from this field started since 1971 and remains among the most important producing fields in the Norwegian North Sea. The NCS embraces three petroleum provinces (Norwegian North Sea, Norwegian Sea and the Norwegian sector of Barents Sea) and contains 78 fields currently under active production in addition to 12 abandoned fields all from the Norwegian North Sea (NPD, 2014). The Barents Sea is also another area apart from North Sea and Norwegian Sea for hydrocarbon exploration interest. This petroleum province has been opened partly for exploration in the Norwegian sector in 1979. Since then important discoveries has been made in the area such as Snøhvit gas field (1981), Goliat (2000), and Johan Castberg (2011) oil fields. Moreover, based on the total undiscovered resource estimate made by Norwegian Petroleum Directorate in the Norwegian Continental Shelf (NCS) in 2016 about half of the expected petroleum resources are coming from the Barents Sea (NPD, 2016).

The Barents Sea basin contains potential source rocks from the Lower Carboniferous, upper Permian, upper Triassic and upper Jurassic sedimentary successions in which the most important source being Hekkingen Fm (Pedersen et al., 2006) . On the other hand, the middle Jurassic Stø Formation is the most important reservoir rock unit with an almost 85% of the Norwegian Barents sea resources contained in it (Larsen et al., 1993) . Other potential reservoir rocks include from Devonian, carboniferous, Permian carbonates and Silurian, carboniferous, Permian, Triassic, Jurassic and cretaceous sandstones where the lower-middle Jurassic sandstones are the most important proven reservoirs yet with widespread occurrences (Johansen et al., 1992). The Stø Formation has widespread occurrences in the western Barents Sea and usually contains favorable reservoir properties (porosity and permeability). Important sandstone reservoir properties, porosity and permeability, are primarily a function of types of sediment input, processes prevailing during deposition, and changes occurring during progressive burial (Ali et al., 2010; Bjørlykke and Jahren, 2015). Thorough examination of these parameters and their interrelationships is crucial for understating reservoir quality evolution through time. In addition, the Barents Sea is becoming a candidate for commercial site for carbon-dioxide sequestration including the Stø Formation. Complex geologic evolution from the formation of orogenic basement, extensional-rifted subsidence basins, strike-slip movements, glaciations, regional uplift and exhumation processes adds an interest to see deviations that could have brought to the characteristics of sedimentary deposits in the entire well section in general and effect on the sandstone reservoir properties. In this study an integrated approach was employed including conventional sediment logging, petro-physical and petrographic methods to analyze reservoir rock properties of the Stø Formation in the area of southwestern Barents Sea. The focus of this study is in two wells; (7119/9-1 and 7119/12-2) (Fig.1.2b).

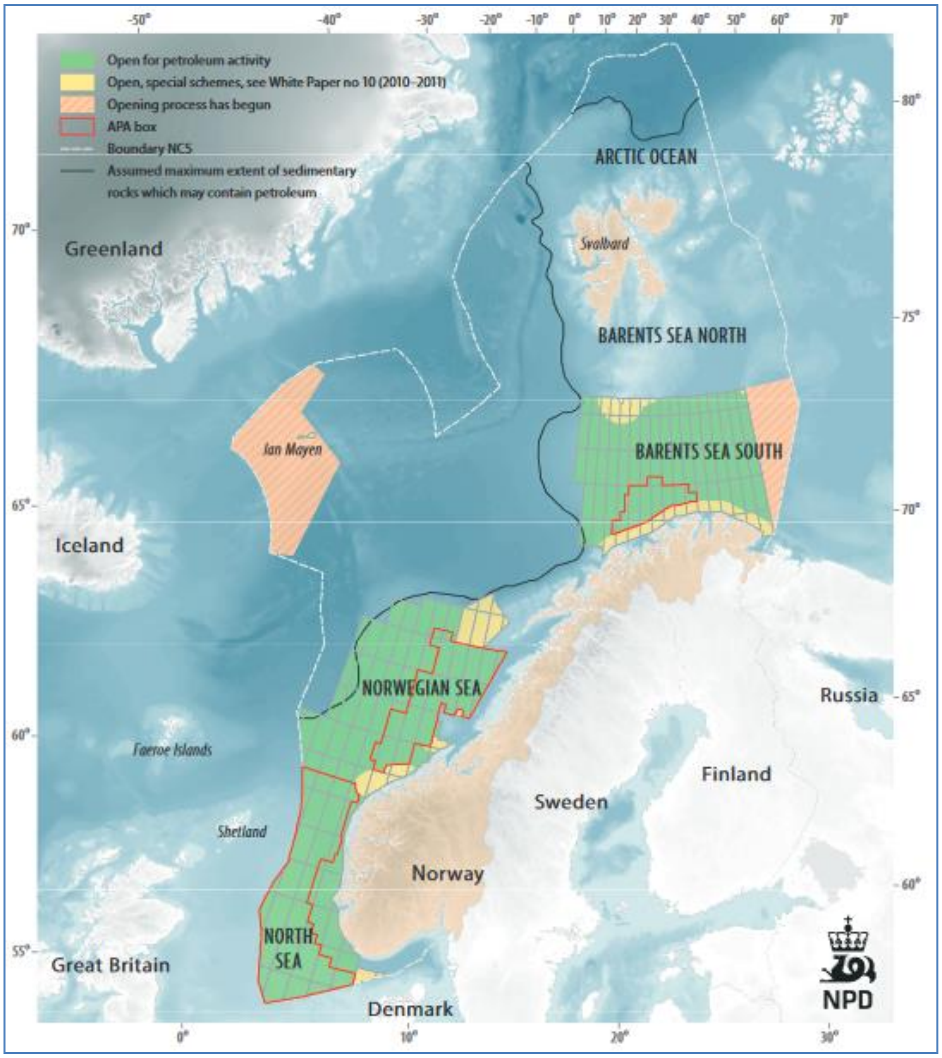

Figure 1.1: Map displaying the areal extent of the Norwegian continental shelf as of March 2012 along with main petroleum exploration activities (NPD, 2014).

1.2 Study Objectives

The primary objective of this study is to analyse reservoir quality of Stø fromation based on two exploration wells: well 7119/9-1 (situated on the Ringvassøy-loppa fault complex) and well 7119/12-2 (located on the Hammerfest basin) (Fig. 1.2b). Geological conventional sediment logging, petrophysical (well log) and petrographic (thin section, SEM, XRD and CL) approaches were employed in order to evaluate the reservoir quality of Stø Formation. Porosity and permeability are the most important reservoir properties that determine storage capacity and deliverability in addition to the obvious importance of presence of vertically thick and lateraly extended reservoir . They are primarily a function of the type of sediment input, depositional system, and modified by mechanical and chemical compaction during burial (Bjørlykke and Jahren, 2015). Provenance and climate are important factors determining mineralogical composition of sediment input and depositional systems that determine textural maturity (sorting, grain size and shape, amount of matrix etc.). These factors are among the most important factors controlling the ultimate reservoir quality during burial.

Specific objectives of this study were:

1/ to study lithology of the Stø Formation and make correlation panel based on the two wells

2/ to analyze mineralogical composition, texture, and facies association of Stø Formation

3/ to better understand sedimentary processes and depositional environments responsible for the reservoir quality development of the Stø Formation

4/ to delineate the possible onset of chemical compaction based on the velocity depth profile and uplift estimation and also by comparing with published experimental and natural mechanical compaction trends

5/ to investigate importance of porosity preservation mechanisms such as chlorite coating, microquartz precipitation, and others

1.3 Study Area

The greater Barents Sea is bounded by the Norwegian-Russian coasts to the south, Novaya Zemlya archipelago separating from Kara Sea to the east, Svalbard (an archipelago in between the Barents Sea and the Arctic Ocean) to the north and by the continental slope of the Norwegian-Greenland Sea from the west (Larssen et al., 2002) (Fig. 1.2A). The Southwestern Barents Sea contains series of NE to SW and NNE-SSW trending structural highs and rift basins divided into three main categories based on crustal structure, tectonic style and stratigraphic makeup (Faleide et al., 1993a). 1) N-S trending oceanic Lofoten Basin and the Vestebakken Volcanic Province, 2) the NNE-SSW trending deep Cretaceous basins (Harstad Basin, Tromsø Basin, Bjørnøya and the Sorvestsnaget basins) with the intervening highs (Senja Ridge, Veslemøy and the Stappen High), and 3) NE-SW trending Jurassic Hammerfest Basin, Finnmark Platform, Loppa High and the Fingerdjupet Subbasin. Continental boundary faults along the Senja Fracture Zone (purple line) separates the Lofoten Basin to the west, while Jurassic and Cretaceous basins and highs to the east. An almost N-S running series of fault complexes bounds the deep Cretaceous basins to the west and Jurassic basins and highs to the east. Troms-Finnmark Fault Complex in the south separates the Harstad and Tromso basins to the west and the Finnmark Platform to the east, Ringvassøy-Loppa Fault Complex bounds west of the Hammerfest Basin and southwest end of the Loppa High from Tromso Basin, and further north Bjørnoyrenna Fault Complex bounds Loppa High from west and east of Bjørnøya Basin (Fig. 1.2B).

This thesis is part of a project based on databases from two exploration wells found in the SWBS (Fig. 1.2b). Exploration well 7119/9-1 is situated on the Ringvassøy-Loppa Fault Complex at 71° 24' 53.19" N, 19° 49' 43.26" E and exploration well 7119/12-2 on the southwestern tail part of the Hammerfest Basin at 71° 0' 51.81" N, 19° 58' 20.81" E from NPD fact pages (NPD, 2016)

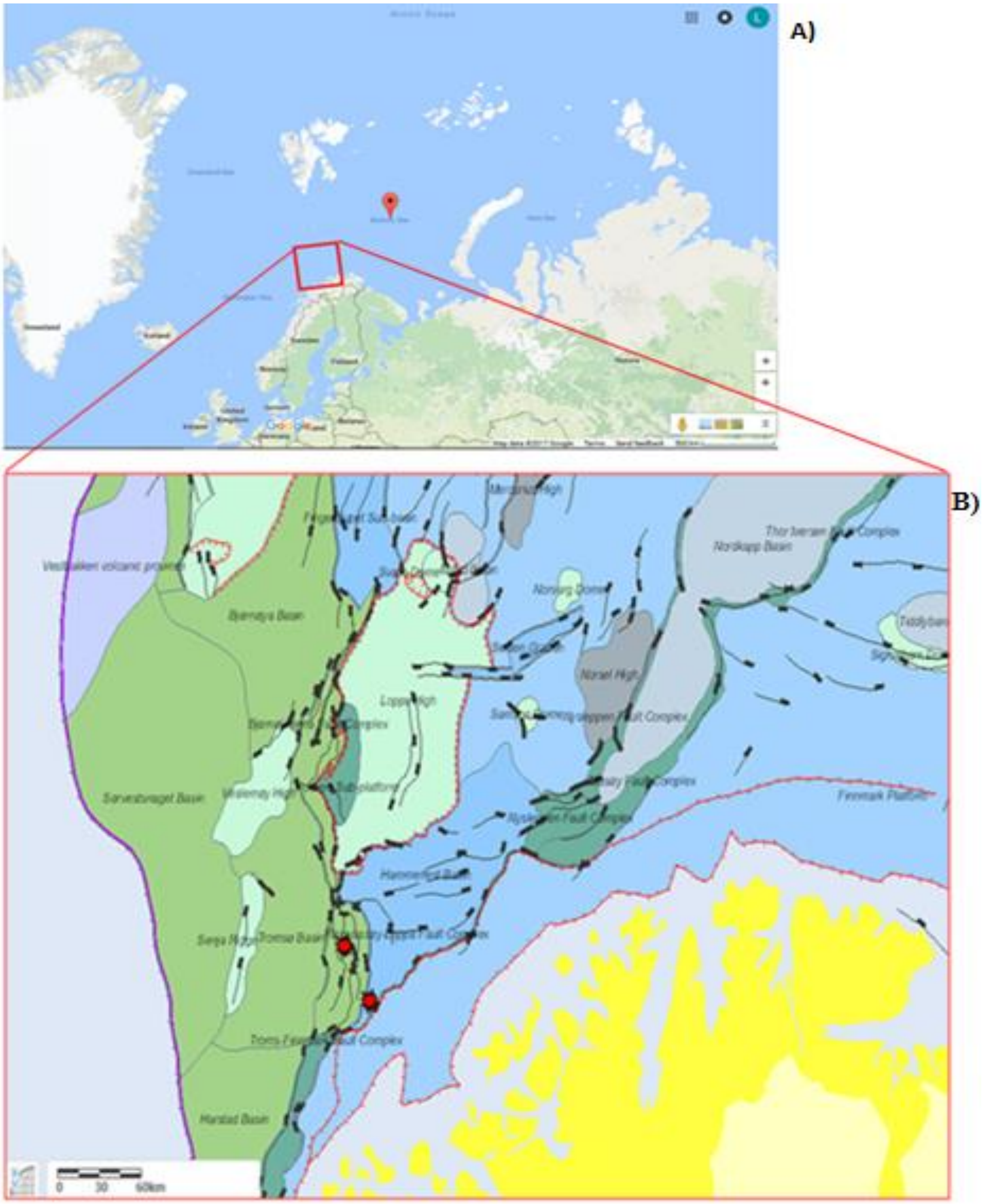

Figure 1.2: Figure displays location of the the SW Barents Sea (A), and main structural elements in the SW Barents Sea (B). Well 7119/9-1 on the Ringvassoy-Loppa fault complex and well 7119/12-2 on the southwestern tail part of the Hammerfest basin (red stars) (NPD, 2016). A-is modified form google maps, which can be accessed at: https://www.google.no/maps/@68.6978172,39.375959,3z

2 GEOLOGIC SETTING OF THE SWBS PETROLEUM PROVINCE

2.1 General Overview of Geology of SW Barents Sea

The Barents Sea is an extensive area of shallow epicontinental shelf with an average depth of 300m, found at the northwestern end of the Eurasian plate and delimited from the south by the Norwegian-Russian coast, Novaya-Zemlya archipelago to the east, Franz-Josef land and Svalbard archipelagoes to the north (Doré, 1995). It is bounded by the Norwegian-Greenland Sea continental margin to the west and covers a large area of approximately 1.3 million (km) ^{2}, which makes it one of the largest areas of continental margin around the globe. Geologically the Barents Sea is situated in an intra-cratonic setting and basement formed mainly from two major collision events: The Caledonian and Uralian orogens around a stable plate called Baltica Figure 2.1. Geologic evolution of the Barents Sea has been described in terms of the influence of The Caledonian and Uralian orogens occurred at different times and places with a different magnitude and trend starting from the basement structure by many authors (Doré, 1991; Faleide et al., 1984; Johansen et al., 1992; Ziegler, 1988). The Caledonian orogeny, which ended around 400Ma during late Silurian/early Devonian periods, resulted in the merging of Laurentian plate (North America and Greenland) and the Baltic plate (Scandinavia, western Russia). This has led to the closure of the Lapetus Ocean consolidated the above continental plates and formed the Laurasian continent (Gee et al., 2006; Roberts, 2003) (Fig. 2.1). N-S trending structural elements in the western Barents Sea and Svalbard, NE-SW trending structural elements in the southwestern Barents Sea and Finnmark platform, and E-W trending structures to the central Barents Sea are attributed to this tectonic event (Fig. 2.2). Further collision of the Laurasian continent with the Siberian plate (Uralian orogeny) has influenced geology of the eastern Barents Sea (Russian sector). It started during the carboniferous times in the south (present Kazhakstan terranes) and was culminated around 240Ma (late Permian/early Triassic times) in the north (today eastern Barents Sea area) (Gee et al., 2006; Puchkov, 1997). N-S trending structural elements paralleling to the Novaya-Zemlya island chains in the eastern Barents Sea zone (Fig. 2.2) are regarded as the result of influence of this tectonic event (Dore, 1995; Faleide et al., 1984).

These continental collisions (Caledonian and Uralian) must have led to the thickening of the corresponding newly formed continental crust and subsequent gravitational collapse (Zeigler, 1998; Faleide et al., 1984; Dore, 1991). Moreover, gravitational collapse of the Caledonian orogenic belt triggered rifting and spreading in the northeast Atlantic and arctic regions. Extensional rifting tectonics was then prevailed in the western Barents Sea starting from the late Devonian-Carboniferous times. Starting from the late Carboniferous times regional subsidence dominated and the entire Barents Sea region became part of a huge Permian-Triassic interior sag basin until a renewed Permian/Early Triassic rifting interrupted it and formation of north-south trending structures in the west (Gudlaugsson et al., 1998). Mainly three extensional tectonic rifting phases with subordinate transpressional to transtensional effects are well documented with the recognition of more small scale rifting episodes like during the Permian, and Triassic (Faleide et al., 1993; Dore, 1995). These three main rifting phases categorized into late Devonian-carboniferous, middle Jurassic–early cretaceous and the early tertiary.

Stratigraphic development in the area goes back to the Caledonian times with the earliest Sedimentary deposits covering the basement recorded on the onshore areas of the Barents Sea region starting from Devonian times. According to (Faleide et al., 1984), Molasses sediments of Devonian times have been recorded in the Svalbard and east Greenland areas covering the Caledonian basement. Following the Caledonian orogeny, the western Barents Sea had undergone a crustal extensional regime established an extensive continental rift zone during the late Devonian-early carboniferous times (Gudlaugsson et al., 1998). In addition, during the mid-carboniferous times further crustal extension and rifting occurred as a continuation of the north Atlantic rifting tectonics. Continental clastics with coals deposited in the first continental rifting regime and further rifting during the mid-carboniferous times led to subsidence of the craton and immersed under water created a carbonate platform and deposition of evaporates in local basins (Faleide et al. 1984; Larssen et al., 2002). Carbonate deposition continued up to the onset of the first significant rifting episode during the late Permian-early Triassic times in the western Barents Sea area. Uplift of the landmasses from the eastern and southeastern of the Barents Sea area during the Uralian orogeny favored the transition of carbonate deposition into clastic deposition in the western part (Johansen et al., 1992; Larssen et al., 2002). Relatively tectonically quiet period was prevailed during the early Triassic until the mid-Jurassic rifting episode in the whole Barents Sea area. Sedimentation was controlled by change in climate as the area moved about 40-50 degrees north from its original position during the Triassic (Jacobsen and van Veen, 1984; Steel and Worsley, 1984a). Tectonic control on sedimentation from the second major rifting episode (late Jurassic-early cretaceous) onwards was immense. Structural features in the southwestern Barents Sea from late Paleozoic crustal extension experienced further rifting which amplifies structural highs like the Loppa high during the mid-Jurassic. Further subsidence during the Cretaceous brought more pronounced effects to the westernmost structures created NNE trending deep basins such as Bjørnøya, Tromsø and the Harstad basins (Faleide et al., 1993a, b). Sedimentary successions from the Triassic deposits are uplifted and eroded in the structural highs (Loppa High, Stapen High) and organic rich shale depositions across the Barents sea was prevailed during the upper Jurassic marked a very important source rock strata for the area (Glørstad-Clark et al., 2011). Cretaceous subsidence effects are less in the Jurassic basins and highs (hammerfest basin, Loppa high, Finnmark platform) and much less effect in the Paleozoic basins further east (Nordkapp basin). Later during the third major rifting event (earliest Cenozoic) the western Barents Sea was developed into continental margin and later into sea floor spreading connecting the north Atlantic and arctic oceans (Dimakis et al., 1998; Faleide et al., 1991; Faleide et al., 1993b). Regional uplift and erosion dominated the Barents Sea during the Cenozoic and North-South tilting of the crustal block of the region (Faleide et al., 1993b; Faleide et al., 1993a; Wood et al., 1989). It was followed by tectonically quiet period during the Oligocene and basin wide Neogene uplift resulted in the deposition of a large sedimentary wedge consisting mainly Pliocene-Pleistocene glacial deposits to the west (Faleide et al., 1996) cited in (Gløsrtad et al., 2011).

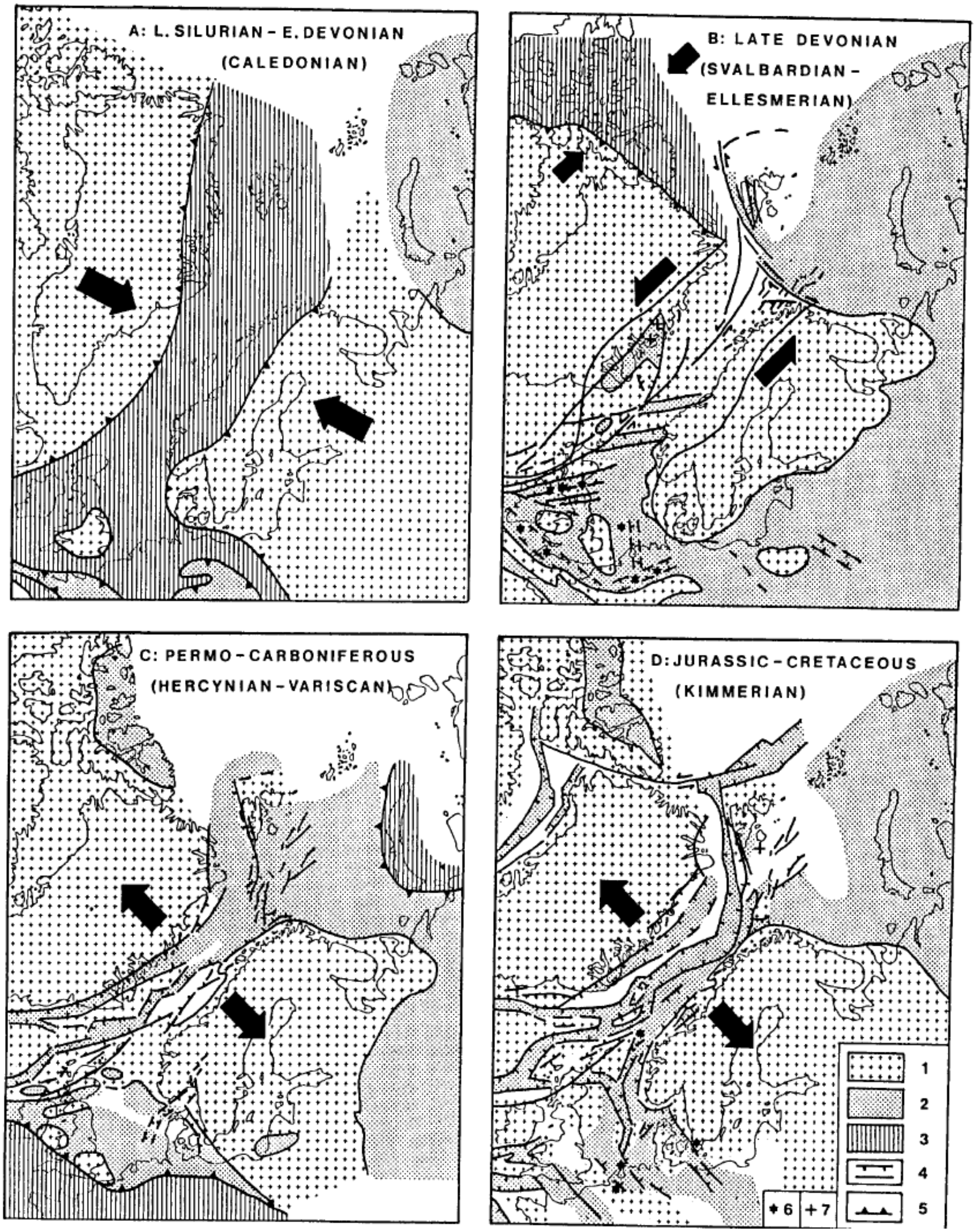

Figure 2.1: Map shows main evolution stages in the development of western Barents Sea and surrounding areas. 1) Stable elements-continental cratons and intrabasinal highs 2) sedimentary basins 3) active fold belts 4) normal and wrench faults 5) deformation front of active fold belts 6) intrusions and 7) volcanics. Image modified from (Faleide et al.1984).

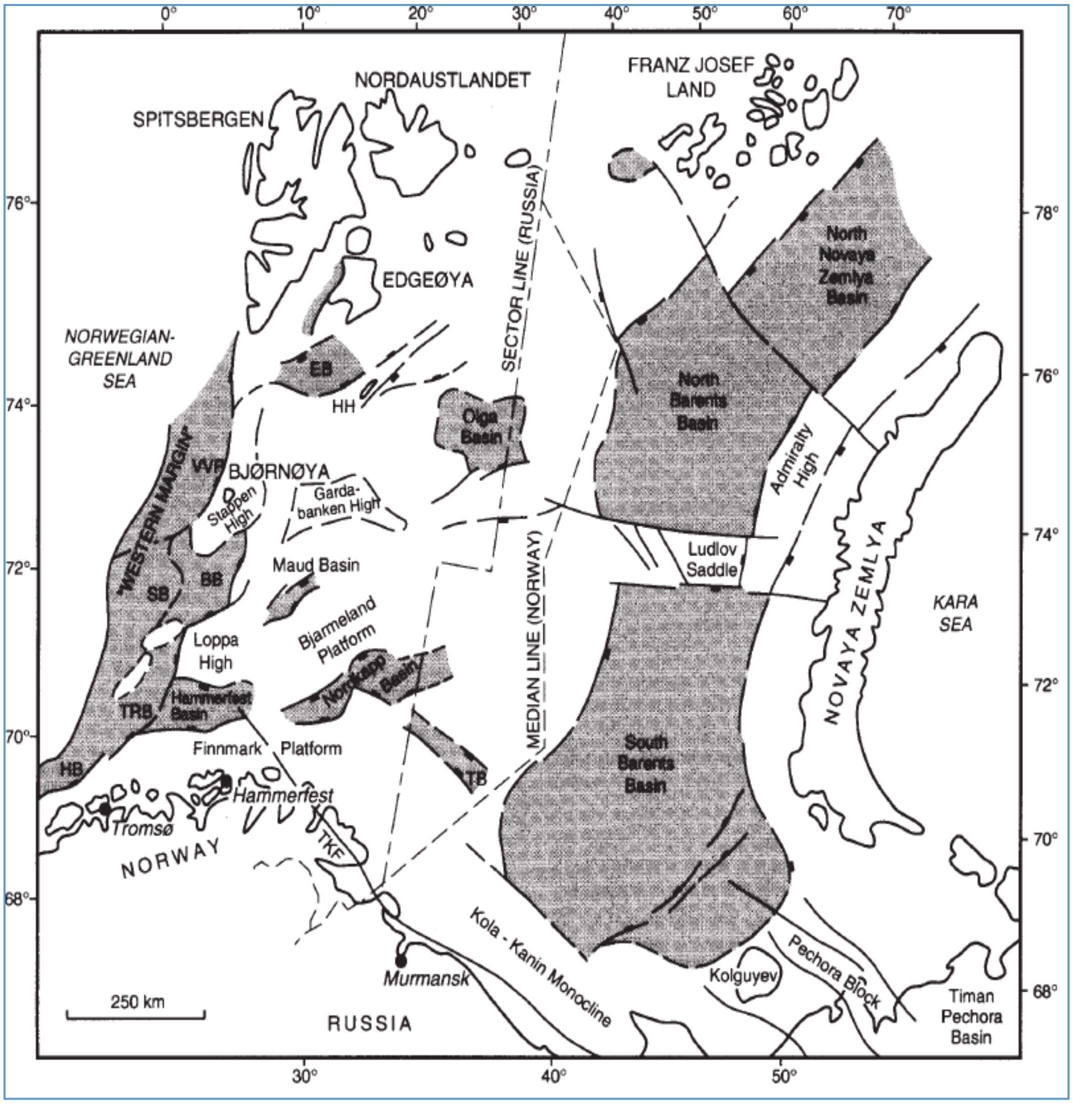

Figure 2.2: Map shows main structural elements of the greater Barents Sea, sedimentary basins are shaded, where BB-Bjørnøya Basin, EB-Edgoøya Basin, HB- Harstad basin, HH-Hopen High, SB Sørvestsnaget basin, TB-Tiddlybanken basin, TRB-Tromsø Basin, VVP-Vestbakken Volcanic Province. Image taken from (Dore et al., 1995)

2.2 Geologic Setting of the Southwestern Barents Sea

2.2.1 Structural Evolution

The southwestern Barents Sea is situated in the area where influences from the spreading of northeastern Atlantic Ocean from south and the Arctic region from north are seen: including a shift of center of propagation of rifting from the central Barents Sea to the western margin, transform (transtensional-transpressional) tectonic style (Faleide et al., 1993). It contains among the deepest sedimentary basins in the world.

Many workers have linked its Basement structure to the Caledonian orogenic belt, which has lasted roughly 400Ma. Examples; A dominantly North-Easterly trending regional Extensional regime dominated the SWBS area during the late Paleozoic (Silurian-Devonian) period along the Caledonian Orogeny (Doré, 1991; Faleide et al., 1993a; Gudlaugsson et al., 1998; Johansen et al., 1992; Ronnevik et al., 1982; Ziegler, 1988). In addition, Dorè (1991) stated that Urals influences are seen in the north-south trending structures in the eastern part of the Barents Sea whereas the Caledonian influences are seen in the N-S trending western Barents Sea margin and Svalbard and the NE-SW trending structural elements in the southwestern Barents Sea area. These phenomena of formation of extensional zones and new oceans along the line of old orogens is common in the geological record and is a fundamental constitute of the Wilson Cycle (Doré et al., 1999). Also, the tectonic style prevailed during the first establishment of rifted basins in this area is debatable, that most earlier authors suggested late Devonian-middle carboniferous tectonics with a coupled effect of large scale strike-slip and extensional movements were responsible (Ronnevik et al., 1982; Rønnevik and Jacobsen, 1984).

Contrary to this, recent studies agree that structures have dominantly extensional characters and at least two rifting phases (late Devonian-middle carboniferous and Permian-early Triassic periods) have been occurred in the formation of late Paleozoic basins (Dengo and Røssland, 2013; Gabrielsen, 1990; Jensen and Sørensen, 1992) as mentioned in (Gudlaugsson et al.1998). Accordingly, NE-SW and N-S striking Tromsø, Bjørnøya, Nordkapp, and the Fingerdjupet basins have been interpreted as rift basins established in the late Devonian-middle Carboniferous times. The Hammerfest basin is also believed to be initiated by this time (Dengo & Røssland, 2013; Jensen & Sørensen, 1992). Continued major rifting phases (middle-late Jurassic to early cretaceous), and the Cenozoic continental breakup has pronounced effects both from the northward seafloor spreading of the central Atlantic Ocean and Arctic region. This includes effect of change of extension center from the central to the western Barents Sea region and development of strike slip (transform) movements resulted in the formation of deep cretaceous pull-apart basins in the SWBS area (Faleide et al., 1993).

The Lofoten Basin is an oceanic basin developed by the Cenozoic seafloor spreading in the Norwegian-Greenland Sea. An oceanic crust approximately (4.5-6km) thickness is characterized by high velocity anomaly adjacent to the continent-ocean boundary (Jackson et al., 1990) from (Faleide et al., 1993). The high-density crust gives high velocity anomaly seaward of the Senja Fracture Zone (Eldholm et al., 1987). 5-7km of Middle and Upper Cenozoic strata covers the oceanic basement (Faleide et al., 1993). The Lofoten basin is bounded by a narrow continent-ocean transition along the Senja Fracture Zone to the east (Faleide et al., 1991).

The Sørvestsnaget basin is a marginal basin affected by the Tertiary breakup and was controlled by older structures (Senja ridge, Veslemøy high, and Stappen high). Tectonically quiet period during the Oligocene was followed by regional subsidence combined with widespread rifting in the western resulted in the development of huge post-Oligocene sedimentary wedge eroded from the eastern Barents Sea province (Fig. 2.4). Positive structural features within the basin west of Senja Ridge interpreted as salt structures are seen to interrupt pre-Cenozoic sediments, similar to in Tromsø basin (Faleide et al. 1993).

The deep cretaceous (Harstad, Tromsø, and Bjørnøya) basins are affected by the cretaceous subsidence and sedimentation (Faleide et al., 1993). A deep seismic reflection and refraction profiles indicate poorly known considerable section of pre-middle Jurassic strata in this basin, which it probably includes thick Triassic and Jurassic clastic sediments as well as Permo-Carboniferous mixed carbonates, evaporates and clastic sediments as suggested by (Ronnevik & Jacobsen, 1984; Faleide et al., 1984) cited at (Faleide et al., 1993). A mid-Jurassic rift unconformity below Cretaceous and Tertiary sequences (more than 5s TWT) can be followed in the Harstad basin (Faleide et al., 1993) and its southern part is affected by large-scale listric faults associated with hanging wall rollover anticlines. The Tromsø Basin is a North-Northeast trending deep structure mainly evolved during the late Jurassic-early cretaceous extension and affected by halokinesis and development of enhanced local subsidence. The Bjørnøya basin is divided into shallow eastern part (Fingerdjupet Sub-basin) and western of the Leirdjupet Fault Complex and appears to be a large half-graben down faulted along the Bjørnøyrena Fault Complex filled with early cretaceous strata (Faleide et al., 1993). Intrabasinal highs that were active during several tectonic phases became positive features mainly by late Cretaceous and early Tertiary faulting and differential subsidence (Faleide et al., 1993). The Senja ridge, which separates the Tromsø and Sørvestsnaget basins, interpreted to involve transpressional deformation during its formation. Mainly normal faulting forms it and salt diapers during the late Cretaceous-early Tertiary occurred in the Tromsø and Sørvestsnaget Basins. The Veslemøy High separates the Tromsø and Bjørnøya Basins is associated with major deep-seated west-facing faults forming a southerly continuation of the Bjørnøyrena Fault complex.

A series of fault complexes bordered younger deep Cretaceous basins to the west and the relatively older structures sitting in a general platform area to the east in the SWBS area. These include the Troms-Finmark Fault Complex (TFFC), Ringvassøy-Loppa Fault Complex (RLFC), Bjørnøyrenna Fault Complex (BFC) and the Leirdjupet Fault Complexes (LFC). They are extensional in origin and developed mainly in the early Cretaceous times (Faleide et al., 1993). Structural style in the TFFC and the BFC is dominantly listric faulting. The NNE trending RLFC separates the Hammerfest basin and Loppa high from the deep Tromsø basin is characterized by a terrace comprising rotated fault blocks and crosscuts the Hammerfest Basin (Gabrielsen et al., 1984). The LFC is defined by a single large fault in the south, associated with flexures and drag phenomena splitting into smaller rotated fault blocks to the north (Faleide et al., 1993).

The Loppa High, Eastern Bjørnøya Basin, Hammerfest Basin and the Finnmark platform lay on the Eastern platform region believed to affect by the Jurassic rifting without large-scale post-rift subsidence (Faleide et al., 1993). The Loppa High consists of an eastern platform and a western part underlain by shallow Caledonian metamorphic basement is a result of post-middle Jurassic tectonism (Gabrielsen et al., 1990a). The western crest of the high is bounded by rotated fault blocks with the faults appear listric and detachment below the Triassic. It was an island with deep canyons cutting into the Triassic strata supplying submarine fans in the basins to the south and west (Faleide et al., 1993). It was covered by Palaeogene mudstone deposition and been eroded by later uplift (Wood et al., 1989).

The Hammerfest Basin is a NE-SW trending, bounded by deep, high angle faults along basin flanks and listric normal faults detached above or within the Permian sequences in the basin center (Faleide et al., 1993). It is bounded to the south by the Troms–Finnmark Fault Complex, to the west by the Ringvassøy–Loppa Fault Complex, to the north by the Asterias Fault Complex and the Loppa High and to the east mainly by the Bjarmeland Platform. Dominantly extensional basin outline with minor strike-slip deformation in the late Jurassic to early Cretaceous times (Berglund et al., 1986; Gabrielsen et al., 1990b). Its internal structure characterized by a gentle dome parallel to the basin center, which was developed during the middle Jurassic-early Cretaceous rifting. Dome structure is cut by E-W to WNE-ESE running faults and hosts most of hydrocarbon discoveries made in the Norwegian sector of the Barents Sea.

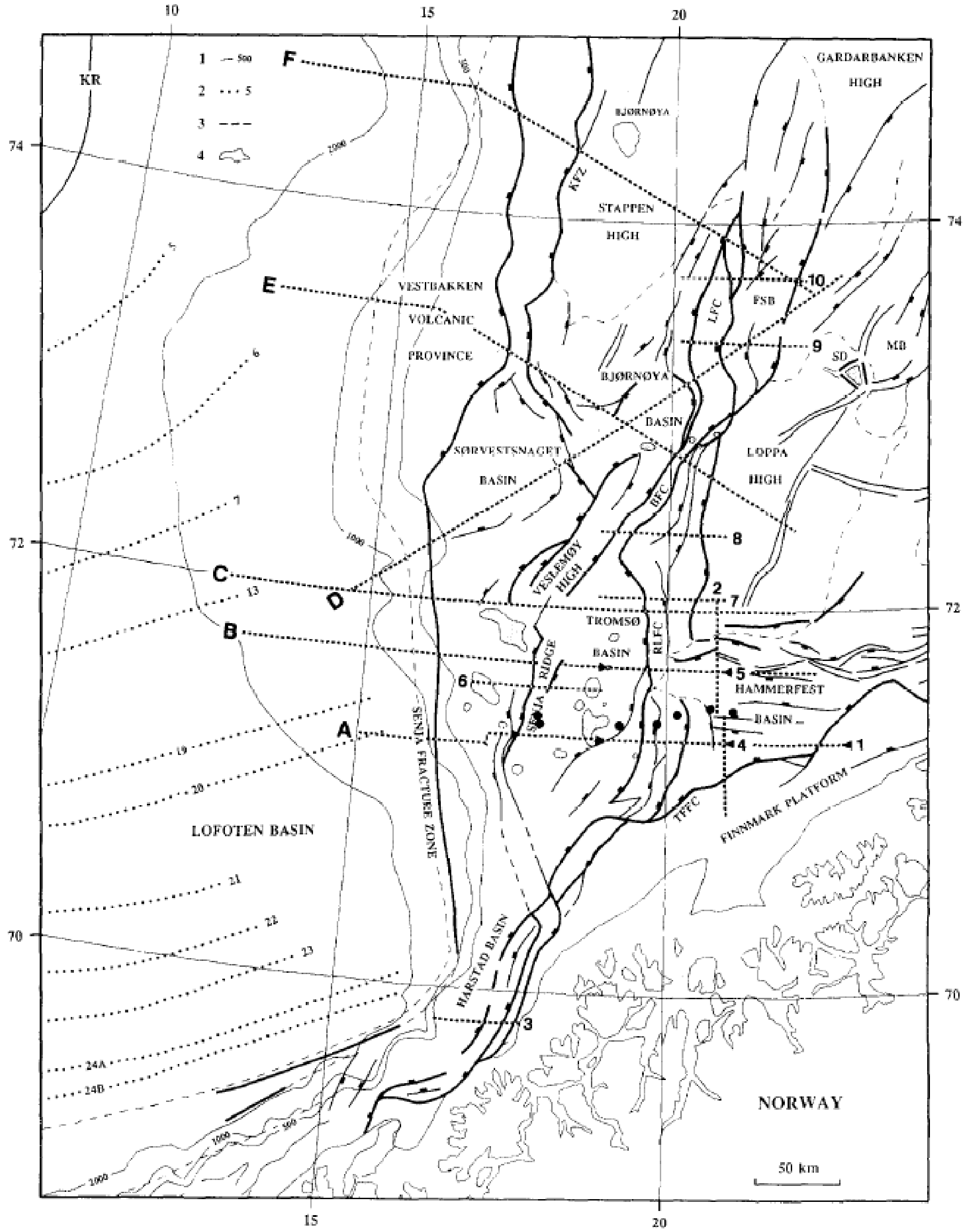

Figure 2.3: Map shows main structural features in the SWBS and location of seismic sections (dotted lines) in which section 'A' is shown in Figure 2.4 below. AFC= Asterias Falt Complex; BFC-Bjørnøyrenna Fault Complex; FSB-Fingerdjupet Subbasin, KFZ-Knølegga Fault Zone; KR-Knipovich Ridge; LFC-Leirdjupet Fault complex; MB-Maud basin; RLFC-Ringvassøy-Loppa Fault Complex; SD-Svalis Dome; TFFC-Troms-Finnmark Fault Complex (Faleide et al., 1993).

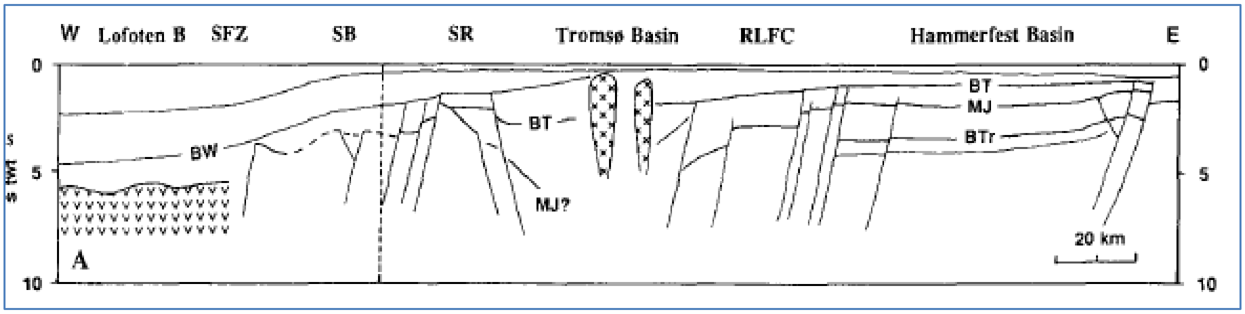

Figure 2.4: seismic section ‘A’ crosscutting main structural elements in the SWBS area. SFZ=Senja Fracture Zone; SB=Sørvestsnaget Basin; SR=Senja Ridge; RLFC=Ringvassøy-Loppa Fault Complex (Faleide et al., 1993).

2.2.2 Stratigraphy

During an extension regime prevailed in the late Paleozoic (Devonian-early Carboniferous) times, following the Caledonian Orogeny, continental clastics were deposited in a rift grabens (Glørstad et al., 2011). A relatively quiet period from late Carboniferous until the Permian was accompanied by a dominantly carbonate platform deposition as well as evaporates (Faleide et al., 1984; Larssen et al., 2002). During the buildup of the Uralian Mountains, an uplift of landmasses to the south-southeastern Barents Sea and significant extensional event in the western Barents Sea (late Permian) favored again the deposition of clastics in the SWBS area throughout the Triassic period (Johansen et al., 1993; Larssen et al., 2002; Gudlaugsson et al., 1998) as cited in (Glørstad et al., 2011). Triassic successions generally characterized by stacked clastic wedges that have prograded predominantly toward the west and northwest of the Barents Sea (Glørstad et al., 2010). A relatively quiet tectonic period (only minor tectonic events) during the lower to middle Triassic period dominated the SWBS in which types of sediment input was controlled by small-scale tectonic movements, climatic variations and northward drift (Jacobsen and van Veen, 1984; Mørk et al., 1989).

The main Svalbard Archipelago moved from about 40-60degree north and deposition occurred in an arid to humid climate conditions with periodic restricted circulation (Steel and Worsley, 1984b). Shallow marine to continental sandstones identified as reservoir rocks are recognized in all formations in the Triassic succession and up to the middle Jurassic (Jacobsen and van Veen, 1984; Mørk et al., 1989; Skjold et al., 1998) cited in (Glørstad-Clark et al., 2010). Middle Jurassic sandstones, which contain the Stø Formation, form the main reservoir rocks in the Hammerfest basin (Berglund et al., 1986; Olaussen et al., 1984) which is home to most of discoveries made until now. Deposition of organic rich shales in the late Jurassic period in the Barents Sea is an important source rock in the area (Glørstad-Clark et al., 2011). Tectonic rifting during the middle-late Jurassic to the early cretaceous contributed to the formation of the present day Loppa and Stappen highs in which Triassic to early Jurassic strata were uplifted and eroded (Doré, 1991; Faleide et al., 2008; Worsley, 2008).

Rifting and continental breakup during the early Cenozoic (Paleocene-Eocene) times in the western margin was accompanied by a regional uplift and erosion generally in the Barents Sea region during the Eocene-Oligocene times (Faleide et al., 1993a, b; Wood et al., 1989). Depositional break occurred during the Cretaceous-Tertiary transition throughout the South-Western Barents Sea (Dalland et al., 1988). Late Paleocene to early/middle Eocene sequences of dominantly claystones, interbedded thin siltstones, tuffs and carbonates deposited in an open and deep marine shelf environments preserved in the Hammerfest basin (Spencer et al., 1984). Faleide et al. (1993) also suggested that thin late Cretaceous-early Paleocene sequences present throughout the south western Barents Sea from seismic data and younger sequences (Eocene-Oligocene) are preserved only in the deep Cretaceous (Tromsø, Harstad, and Sørvestsnaget) basins. Tectonic quiescence of the Barents Sea margin during the Oligocene and regional subsidence combined with an uplifted eastern Barents Sea region resulted in the construction of huge post Oligocene sedimentary wedge mainly the Late Pliocene- Pleistocene glacial deposits (Faleide et al., 1993).

Lithostratigraphic correlation with seismic sequence boundary is possible up to the Middle Jurassic in the SWBS area with well controls from the Hammerfest Basin, which penetrated up to the Permian deposits (Fig. 2.4), (Faleide et al., 1993). Figure 2.5 below shows a chronostratigraphic correlation in the SWBS petroleum province, which includes the Ringvassøy-Loppa Fault Complex (RLFC) and the Hammerfest Basin (HB) where the two well are located (7119/9-1 and 7119/12-2). Well 7119/9-1 is located in the RLFC On an elongated NE-SW trending narrow horst structure while well 7119/12-2 is located in a narrow extension of the Hammerfest Basin to the southwest (Fig. 1.2).

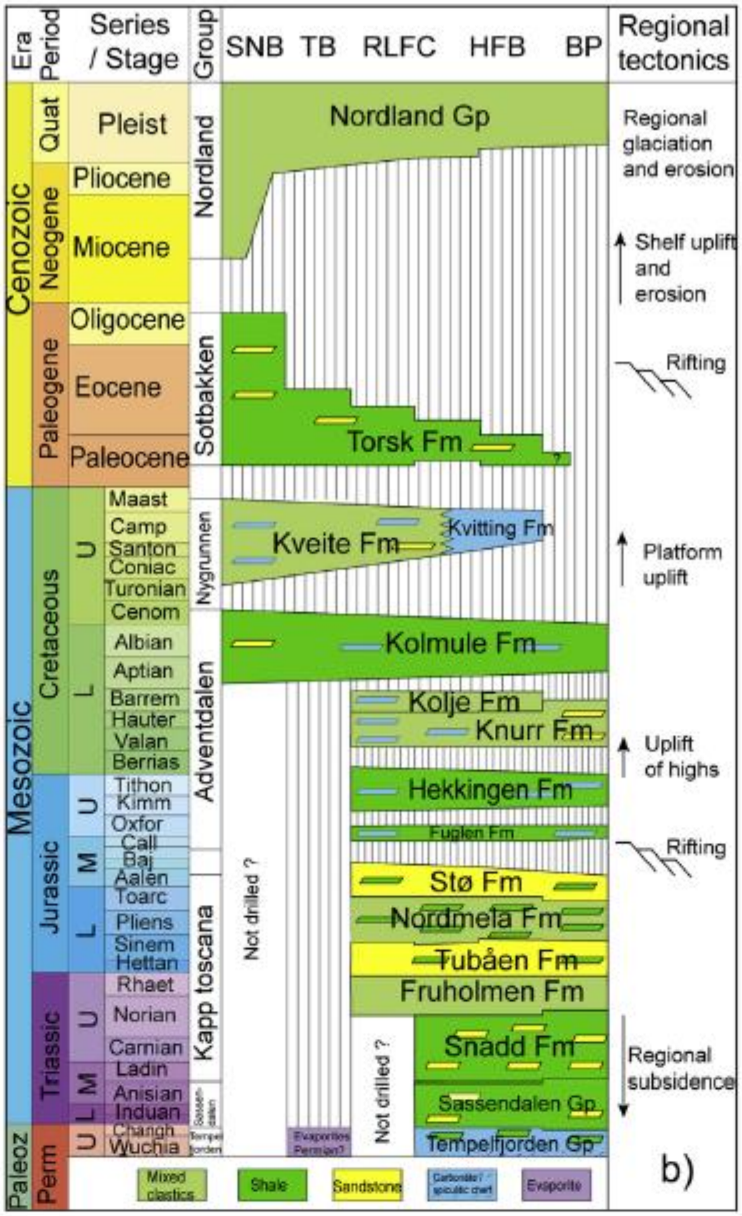

Figure 2.5: Chronostratigraphic correlation of lithostratigraphic units in the main structural elements of the SWBS area, chronostratigraphic data and major tectonic events are compiled from the production license completion reports and modified after (Dalland et al., 1988; Ryseth et al., 2003; Worsley, 2008). BP, Bjarmeland platform; HFB, Hammerfest Basin; RLFC Ringvassøy-Loppa Fault Complex; SNB, Sørvestsnaget Basin; TB, Tromsø Basin. Figure modified from (Baig et al., 2016)

The Realgrunnen Subgroup is predominantly pale grey sandstones with shale intervals most common in the lower parts where thin coals also occur is defined in the Hammerfest basin to comprise four formations; Fruholmen, Tubåen, Nordmela and the Stø Formations (NPD, 2016). It is mostly completely developed in the SWBS and consists of mature sandstones deposited in coastal plain, deltaic and shallow marine environments (Worsley et al., 1988)

Stø Formation (Late Pliensbachian-Bajocian) consists of moderately to well sorted, mineralogically mature sandstones. There are thin units of shales and siltstones, which are regarded as regional markers, and especially the upper part of this succession has occurrences of some phosphatic lag conglomerates (Worsley et al., 1988). Consistent with the underlying Nordmela formation, it thickens towards the west in the Hammerfest basin (Fig. 2.6). It is characterized by blocky to smooth cylindrical well log gamma ray patterns and density readings gradually decreasing upwards (NPD, 2016). Three discrete depositional units define the Stø Formation: the basal part defined by transgressive episodes where this unit is present only in the western parts of the Hammerfest basin, the middle part representing maximum transgression and (III) the highly variable uppermost unit owing to syn-depositional uplift and winnowing as well as later differential erosion (Worsley et al., 1988). The sand is deposited in a prograding coastal depositional environment and it marks the regional transgressive pulses depositing shales/siltstones in a deep shelf setting (Dalland et al., 1988).

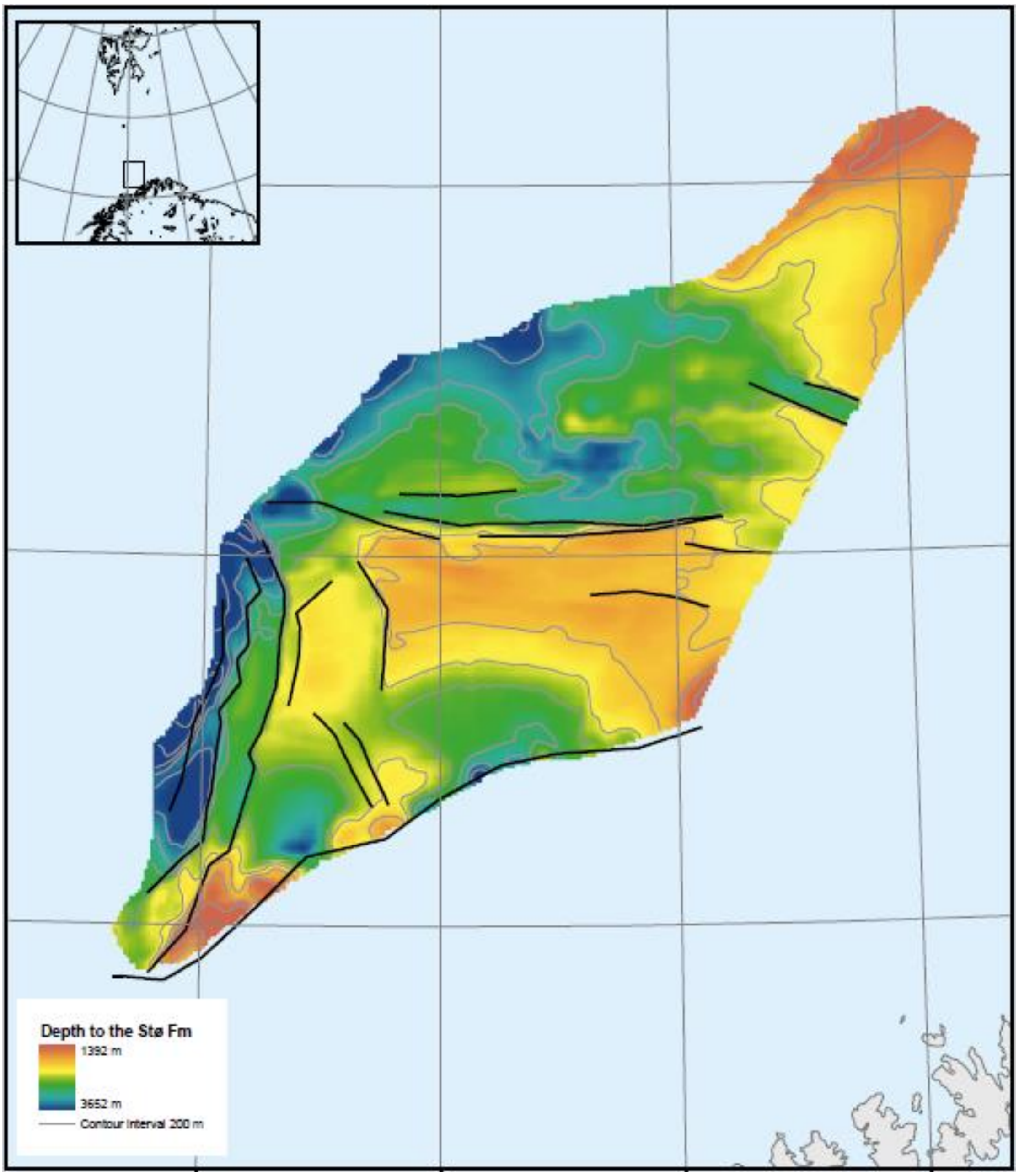

Figure 2.6: Depth property of the Stø Formation in the Hammerfest Basin. Depth map taken from (NPD fact pages)

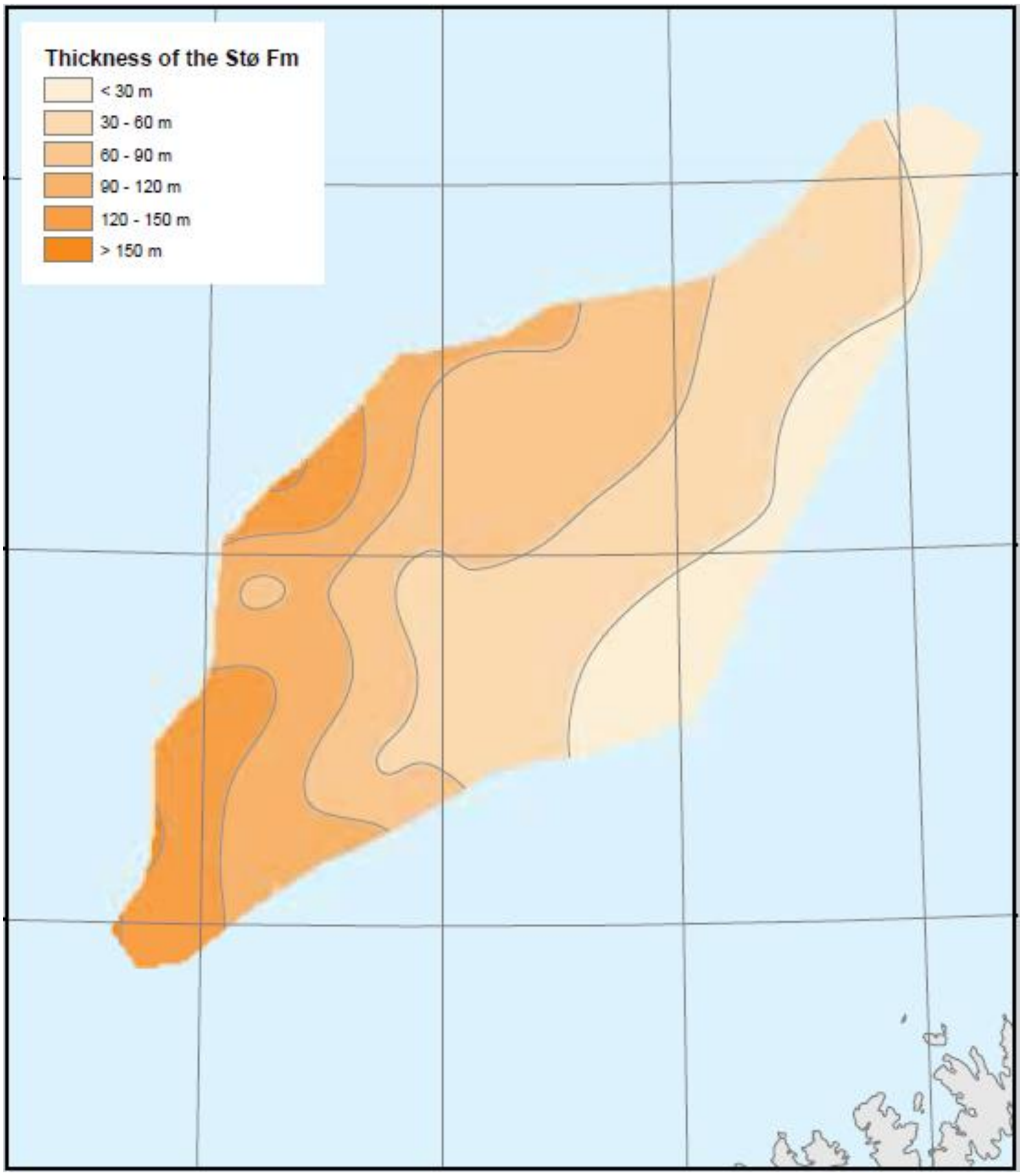

Figure 2.7: Thickness map of the Stø Formation in the Hammerfest Basin. Modified from (NPD fact pages)

2.2.3 Petroleum System and uplift implications

Potential reservoir rocks in the Barents Sea area include from Devonian, carboniferous, Permian carbonates and Silurian, carboniferous, Permian, Triassic, Jurassic and cretaceous sandstones however the lower-middle Jurassic sandstones are the most important proven reservoirs and have widespread occurrences (Johansen et al., 1992). The Stø Formation (middle Jurassic) is deposited in a coastal marine setting. Very commonly, this formation has favorable reservoir properties and is estimated to account about 85% of the Norwegian Barents Sea petroleum resources (Larsen et al., 1993). Variable trapping mechanisms are possible from stratigraphic variability, salt dome structures in the Barents Sea basin while fault bounded positive structures are the most important traps in the lower-middle Jurassic sandstone reservoir (Fig. 2.8). Excellent seal rocks of upper Jurassic to lower most Cretaceous shales are also the best quality and widely distributed source rocks in the Barents Sea area (Johansen et al., 1992). The most important source rock lithology (Hekkingen Fm) is believed to be mature for oil and gas generation in a narrow belt at the western margin of the Hammerfest basin and along the western fringe of the Loppa high whereas it is deeply buried to the west and too shallow to the east (Doré, 1995). Other potential source rocks include from late Paleozoic (upper Devonian, lower carboniferous, carboniferous-Permian) shales, carbonates deposits, middle Triassic shales, lower Jurassic coals and shales, lower Cretaceous shales and tertiary probable gas prone shales and coals along the western margin.

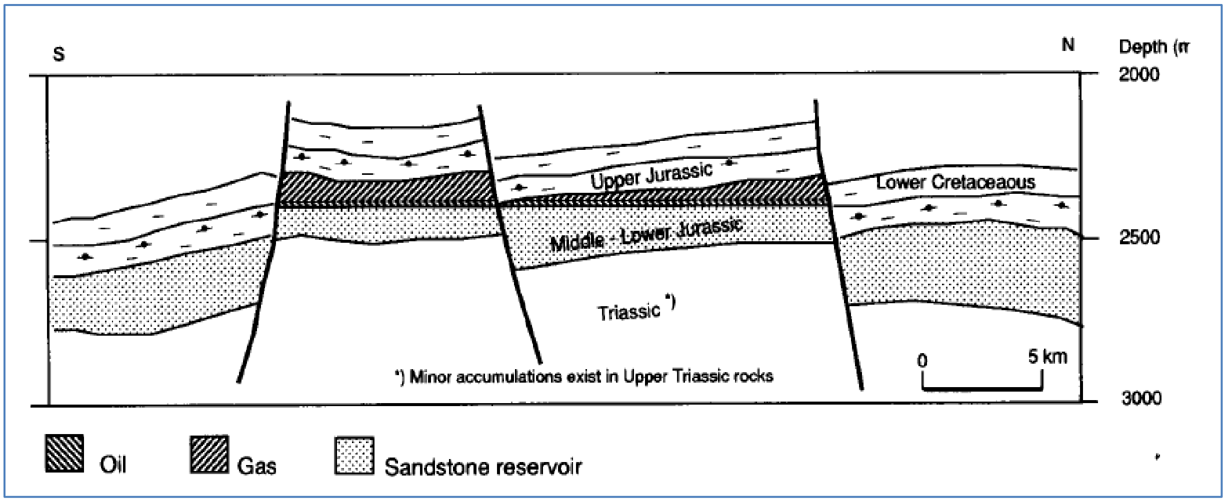

Figure 2.8: Trap mechanism in the Lower-middle Jurassic sandstone reservoirs of Snøhvit oil and gas fields of Hammerfest Basin. Figure was adapted from (Johanssen et al., 1992)

In general, it has been accepted that the Barents Sea shelf has experienced exhumation during the Cenozoic although difficulties exist to define the exact time and mechanisms that caused the initial tectonic uplift where mostly associated it with the opening of the Norwegian-Greenland Sea. Estimated uplift about 3000m in the northwest towards the Stappen High and in the south to the Norwegian mainland, and minimum values of 0-500m uplift around the axial parts of the Hammerfest and Tromsø basins (Nyland et al., 1992). The uplift estimation from diagenetic studies (Walderhaug, 1992) ranges from 1500-2000m indicating deep burial depths of the middle Jurassic sandstones prior to uplift where presently they are buried 1500m in the western Barents Sea area (Doré and Jensen, 1996). Based on shale compaction, thermal maturity and seismic shot gather data the variable degree of Cenozoic exhumation in the SWBS area was well constrained (Baig et al., 2016). Accordingly, it ranges from no or minor net exhumation in the western margin (Sørvestsnaget Basin and Vestbakken Volcanic Provinece), generally increasing towards east and northeast with an average estimates of 800-1400m within the Hammerfest Basin, 1150-1950m on the Loppa High, 1200-1400m on the Finnmark Platform, and 1250-2400m on the Bjarmeland Platform. Reservoir properties (porosity and permeability) of the middle Jurassic sandstones are affected by quartz cementation, authigenic clay mineral formation that confirms greater burial depths than the present occurrences in the western Barents Sea (Berglund et al., 1986; Olaussen et al., 1984; Walderhaug, 1992).

3 THEORETICAL BACKGROUND

3.1 An overview on clastic sedimentary petrology and Sandstone Reservoir Quality Controls

Sedimentary particles that make up clastic sedimentary rocks are mainly derived from the breakdown of pre-existing (igneous, metamorphic and sedimentary) rocks that have been exposed to weathering and erosion processes. The weathering and erosion products (clasts) form clastic sedimentary rocks passing through the course of sedimentary processes (sediment transport, deposition and lithification). In contrast, sedimentary rocks formed from particles of predominantly different origin, e.g. coal composed of mainly remains of plant debris, are non-clastic sedimentary rocks. Carbonates are also non-clastic sedimentary rocks composed of predominantly carbonate minerals (calcite) precipitated from solution in the province of deposition and/or fragments of remains of hard-shelled organisms. Such sedimentary rocks have different geophysico-chemical responses during deposition and subsequent burial diagenesis, and discussion about this topic is beyond the scope of this study.

Mineral composition of clastic sediments is predominantly controlled by the initial bedrock composition, strongly modified during weathering, transportation, depositional processes, and other factors such as humidity and source relief. Initial bedrock composition also has a greater control on the grain size of clastic sediments depending on its proximity to the depositional setting (Bjørlykke and Jahren, 2015). This determines the types of sedimentary rocks and the resulting clastic sediments. Granitic and intermediate composition igneous rocks, coarse grained metasedimentary and metamorphic rocks are most likely to produce weathering resistant larger size grains (e.g. quartz), and basic igneous rocks like gabbro under less weathering conditions produce feldspar grains of greater size. Most volcanic rocks, fine grained sedimentary and metamorphic rocks are less resistant to weathering processes and produce mostly fine grained (clay and silt sized) particles.

Clastic sediments are classified based on the size of sedimentary particles. Sand grains are clastic sediments in the size range of 0.0625-2mm diameter; gravel and conglomerate consist of clasts greater than 2mm, and mud (clay and silt) particles less than 0.0625mm diameter

(Nichols, 2009). Sandstones are clastic sedimentary rocks containing sand particles as a framework grains and form about 60% of all world petroleum reservoirs (Bjørlykke and Jahren, 2015). Silt and clay size particles fill intergranular pore spaces between sand grains existing as matrixes in sandstone units and destroy porosity (Bjørlykke and Jahren, 2015). Sandstone rocks having matrixes amount of less than 15% are called arenites, more than 15% greywacke and an increased content of silt and clay overtake the framework sand grains as load bearing particles and form mudstones (siltstones and shale). Sand grains matrixes filling pore spaces between gravels, pebbles that form framework grains of conglomerates.

Quartz is the most stable sediment grain both mechanically and chemically, and it is one of the most common mineral grains in sandstones and siltstones (Nicholas, 2009). Feldspar rich sandstones are likely formed from sand size grains released from most igneous and some metamorphic (Schists, Gneisses) rocks under low weathering conditions and short transport distances as feldspars are less resistant to weathering and abrasion (Nicholas, 2009). Sand sized grains can also be composed of more than one mineral (lithic fragment) unlike quartz and feldspar, which form the third major constituents in the sandstone framework grains. These are mainly derived from fine to medium-grained igneous, metamorphic and sedimentary rocks. Relatively abundant amount of mica, rarely occurrences of heavy minerals (apatite, rutile, tourmaline etc.) and oxides are other accessory mineral grains in sandstones and show some specific source rocks (provenance). Sandstones can also contain sedimentary particles of different origin including biogenic fragments of hard-shelled organisms, plant debris, and reworked authigenic mineral precipitates in the depositional environment e.g. reworked carbonate mineral precipitates in the shallow marine environments.

Sandstones considered as important reservoir rocks should have to have at least good reservoir rock properties (good porosity and good permeability). Porosity is the measure of potential accumulation of fluids while permeability is measure of capability to transmit fluids. The initial mineral composition and characteristic texture of clastic reservoir rocks (Sandstones) take a greater role on determining the ultimate porosity and permeability conditions. These includes: the grain size, sorting, grain shape, amount of matrix, mineralogical composition and subsequent diagenetic cement which are in-turn a function of provenance, transport processes, climate, and depositional environment (Bjørlykke and Jahren, 2015). Therefore, thorough understanding of these parameters is vital in the prediction of changes happening during burial and ultimately the processes controlling reservoir properties. Mineralogically mature sandstones enriched by physically and chemically stable minerals like quartz and lacking relatively feldspar grains including weak lithic fragments may be good indicators of long transport and stable, low relief provenance (Bjørlykke and Jahren, 2015). In addition, sandstones with such mineral composition compact less under the overburden stress maintaining high porosity and permeability to greater depths (detail below under mechanical compaction) unless quartz cementation prevails. Similarly, sandstones composed of chemically stable minerals will undergo less diagenetic changes with increasing temperature compared to mineralogically immature sandstones.

3.2 Diagenesis

Diagenesis includes all processes including physical and chemical alterations of sediments and sedimentary rocks after the onset of deposition and prior to metamorphism (Bjørlykke and Jahren, 2015; Milliken, 2003). Physical changes like compaction, deformation, reorientation of grains, expulsion of water in an open system are associated with an applying load as sediment layers laid on top of one another. Chemical changes may include dissolution of minerals and precipitation of authigenic minerals, replacement, recrystallization, hydration, cementation, etc... Physical changes are function of effective stress that transmitted through grain-to-grain contact due to overburden load to establish mechanical stability. Chemical alterations are functions of temperature where geochemical systems derived towards thermodynamic and kinetic stability. All such changes are controlled by the primary textural and mineral composition sediment inputs, which in-turn is function of range of processes from weathering, erosion, transport, climate, and deposition (Bjørlykke and Jahren, 2015). Biological activities also have contributions in physical/chemical alterations like bioturbation which mixes up grains destroy sorting, add fecal products, and calcareous materials most important at near surface.

Reservoir properties are the function of diagenetic processes, which usually affect in the direction of reducing porosity and permeability with increasing depth except in some cases of porosity preserving mechanisms exist (Bjørlykke and Jahren, 2015). Accordingly, three main diagenetic processes primarily based on depth of occurrences: (1) Near surface diagenesis in which there is communication with the environment (open system), (2) Mechanical compaction effective up to 2-3km burial depth is function of effective stress. (3) Chemical compaction drives mineral assemblages into thermodynamically stable and is primarily function of temperature. Descriptions given below are tuned with regard to sand depositional system.

3.2.1 Near Surface Diagenetic processes

A range of processes including diffusion of mineral ions, advection of ion carried fluids, evaporation and precipitation of minerals, bacterial activity, bioturbation, meteoric water flow and mineral dissolution act in a variety of depositional environments and climatic conditions bring physical and chemical changes of sedimentary deposits in a shallow burial depth (<1-10m). Mostly in the near surface, where sediments are in contact with the atmosphere/ seawater an oxidizing conditions prevailed. On land environments soil forming processes in exposure to air and fresh water is mostly to occur. In marine environments when there is flushing of fresh water in the presence of permeable layers (sandstones), leaching of unstable minerals like feldspar and mica and precipitation of kaolinite will occur (subsurface weathering). Calcareous fossils will also dissolve and precipitate carbonate cement. Meteoric water contains CO_2 and SO_2 from the atmosphere, which makes it slightly acidic. In addition, humic acid from decaying of plant materials and CO_2 produced in the sulphate reducing zone of sediment layer adds to the acidity of fresh water facilitate dissolution. When water supply is limited as in desert, environments, low permeability beds, pore water become concentrated and precipitation of carbonate cement and kaolinite will no longer stable. Under high silica concentration in pore fluids, smectite precipitation becomes stable instead of kaolinite. Therefore, Constant supply of meteoric water to remove silica and cations is needed for the kaolinite precipitation to proceed. Organic matter decay in the seabed sediments take away oxygen make reducing conditions, create a boundary of high gradient concentrations of oxygen in the water body, and sulfate beneath water sediment contact, redox boundary usually occur at 1-20 cm below sea floor. Oxidation of elements like Fe, Mn in sediment minerals can also consume oxygen most importantly in continental environments but rare in marine conditions, source (Bjørlykke and Jahren, 2015).

Leaching of K-feldspar and Muscovite represented by the chemical equations 3.1, and 3.2 below (Bjørlykke and Jahren, 2015):

$2K\ (Na)\ AlSi_3O_8 + 2H^+ + 9H_2O = Al_2Si_2O_5\,(OH)_4 + 4H_4SiO_4 + 2K^+\,(2Na^+)$ ------------------- (3.1)

Feldspar Kaolinite Dissolved Silica and cations

$2KAl_3Si_3O_{10}\,(OH)_2 + 2H^+ + 3H_2O = 3Al_2Si_2O_5\,(OH)_4 + 2K^+$ ----------------------------------- (3.2)

Muscovite Kaolinite

Biologic activities like bioturbation change textural composition, destroy lamination, overturn deposits and facilitate oxidation. Biogenic products also added into sediments after deposition like fecal products of burrowing worms, calcareous and siliceous biogenic products that may develop into grain coatings, and carbonate and silica cement at deeper depths. A calcite replacement of aragonite in the fragments of hard-shelled organisms is the main source of carbonate cement precipitated in shallow burial depths (Bjørlykke and Jahren, 2015).

3.2.2 Mechanical Compaction

A sediment layer under an overburden load will squeeze fluids out (if present), framework grains will re arrange by sliding, reorientation and crushing to attain stable positions (Bjørlykke and Jahren, 2015). Soft grains also deform plastically by bending, squeezing and bulge out into pore spaces. Sandstones lacking weak/ductile grains will compact by forcing sediment grains closer together and destroy porosity at shallow depths. Moreover, compressibility of rigid grains is much less than pore space compressibility, therefore in quartz rich sandstones that, is most common reservoir rock bulk volume will reduce most importantly by the diminishing of porosity as grain repacking. In sandstones composed of weaker mineral grains like feldspars, lithic fragments solid compressibility may account much for the reduction of bulk volume and is the primary control on the mechanical compaction behavior of sandstones (Pittman and Larese, 1991). Grain size composition also has an important effect on compaction behavior of sandstones and mudstones as well and many experimental studies support this: such as, well-sorted Coarser sand grains compact more than finer sand grains due to grain crushing (Fig. 3.1) (Bjørlykke and Jahren, 2015; Chuhan et al., 2002, 2003). Similarly, mudstones rich in kaolinite (larger size) compact more than smectite rich mudstones (Mondol et al., 2008; Mondol et al., 2007). This is due to the lower grain contact number in the coarse-grained rocks leading to higher concentrated effective stress. Rounded grains generally have smaller contact areas than grains that are more flat and will attain more porosity. Poorly sorted sand sediments have lower initial porosity due to the presence of pore filling materials (matrixes) and compact much faster at shallow depths. Moreover, this will reduce per grain effective stress, lesser rate of framework grains come closer and maintain higher intergranular volume (IGV). Therefore, burial compaction is determined from the mineralogical and textural compositions of primary sediment input. Holding all mineral and lithological factors constant mechanical compaction is function of effective vertical stress defined by the difference between total overburden load and pore fluid pressure (equations 3.3, 3.4). In a hydrostatic pressured sediment:

$$\boldsymbol{\sigma'_v} = \boldsymbol{\sigma_v} - P_p \text{ --- } (3.3)$$

- $\boldsymbol{\sigma'_v}$ is effective stress
- $\boldsymbol{\sigma}_v$ is total stress (total weight of sediment overburden and pore water) given by:

$$\boldsymbol{\sigma_v = \rho_b\, gh} \text{ -- } (3.4)$$

- $\boldsymbol{\rho_b}$ is the $_{\text{bulk}}$ density of overburden
- **g** is the acceleration due to gravity
- **h** is overburden thickness
- $\mathbf{P}_p$ is pore pressure

Higher pore fluid pressure attained where pore water is unable to escape during increased overburden. Increased pore fluid pressure will therefore reduce effective stress; maintain higher pore space and lesser compaction (Bjørlykke and Jahren, 2015).

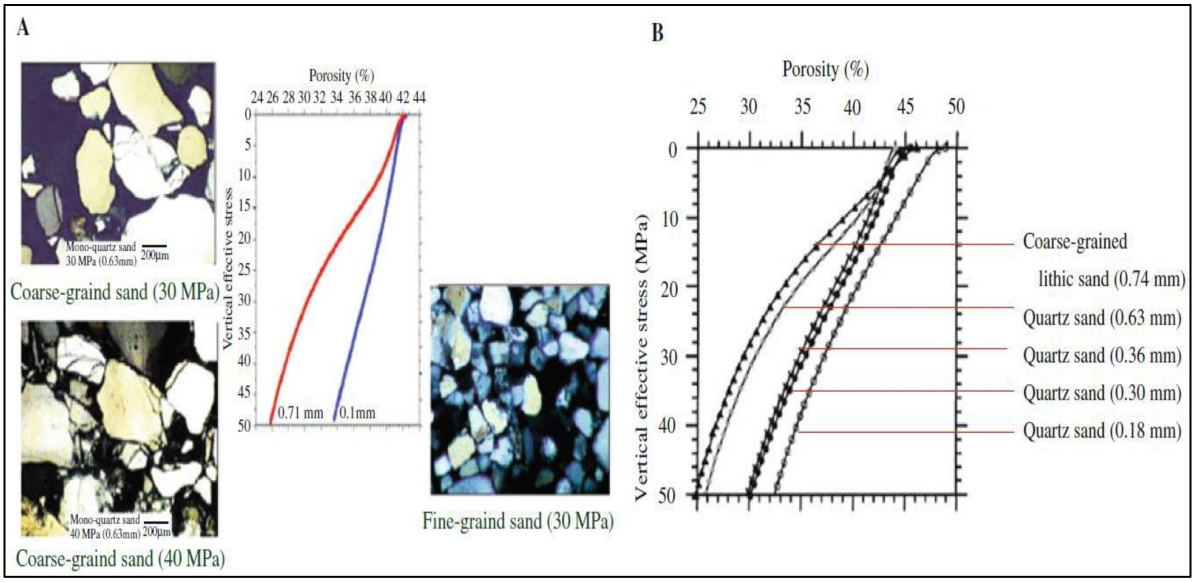

Figure 3.1: Experimental compaction of clastic sediment grains: A) showing well sorted fine-grained quartz grains compact less than coarser grains, B) Higher porosity loss as function of grain size due to grain crushing (Chuhan et al., 2003). Figure modified from (Bjørlykke and Jahren, 2015).

Mechanical compaction reduces in average sandstone porosity from 40-42% to 25-35% at stresses of 20-30 MPa (Chuhan et al., 2002). This is equivalent to an average 2-3km burial depth under normal geothermal gradients and hydrostatic pore pressure conditions. With an increasing depth, area between grain contacts will increase due to pressure solution at contact points, grain crushing, and crystal precipitation on grain surfaces etc. leads to greater mechanical stability. However, Apart from close packing of framework grains they remain loose unless a carbonate cement binds and consolidated them at shallow burial depths (Sharp and McBride, 1989) and is supported by data collected from the North sea basin and parts of Gulf Coast basin (Bjørlykke and Jahren, 2015). This depth range corresponds to temperatures 80-100^{o}C under normal geothermal gradients (25-35^{o}C/km), mechanical compaction ceases and chemical compaction (quartz cementation) takeover on porosity reduction. Only 2-4% of quartz cement will effectively shut down mechanical compaction in sandstones (Bjørlykke and Jahren, 2015). This is due to quartz cement precipitation around framework grains increases contact area and decreases effective stress.

3.2.3 Chemical Compaction

Like the mechanical compaction models, the primary controlling parameters on chemical compaction analyses of siliciclastic sediments is also the nature of primary sediment input. However, chemical compaction is strongly controlled by temperature at which minerals change their initial state towards higher thermodynamic and kinetic stability (Bjørlykke and Jahren, 2015). E.g., Sandstones deposited under restricted chemical weathering conditions like in arid climates, or high relief terrains contain detrital smectite and/or authigenic smectite due to restricted meteoric water flushing at shallow depths. Smectite becomes unstable at temperatures of 70-80^{o}C and start transform to illite (Bjørlykke, 1998; Bjørlykke and Jahren, 2015). Kaolinite transforms into illite at average temperature of 130ºC (Bjørlykke and Jahren, 2015), Amorphous silica (biogenic/volcanic origin), dissolve and re-precipitate to form microcrystalline quartz at temperatures of 60-65ºC (Jahren and Ramm, 2009). Arkosic sandstones have higher potential to produce authigenic kaolinite cement than quartz arenites, which is the main precursor for the formation of illite at greater burial depths (Worden and Morad, 2003). Silica released from clay transformations will also precipitate and form microcrystalline quartz filling pore spaces if the solution is strongly supersaturated. These changes will stiffen specially mudstone deposits at shallow or deeper depths depending on primary mineralogical composition and burial history. Thus, the transition of mechanical to chemical compaction of siliciclastic sedimentary successions may differ significantly due to composition of sediment input (Bjørlykke, 1998).

Quartz cementation: is the most important diagenetic product that destroys porosity of well sorted, quartz rich sandstone reservoirs buried to average depths of 2.5km and above (Bjorlykke and Egeberg, 1993). An effective temperature for the onset of quartz cement precipitation of around 70-80ºC is used in many analyses. It is based on observations made on basins subsided under well-constrained geothermal history and fluid inclusion studies (Lander et al., 2008; Lander and Walderhaug, 1999; Walderhaug, 2000) as described in (Harwood et al., 2013). It is a continuous process once started to precipitate unless the temperature drops below the threshold temperature (Fig. 3.3), if the progression of uplift reached below the quartz formation threshold temperature (Bjørlykke and Jahren, 2015; Harwood et al., 2013). Its rate of precipitation is function of time, temperature and available quartz surface area based on the kinetic models of

(Walderhaug, 1996). Sandstone reservoir exposed to higher temperatures will continue to reduce porosities until it completely diminishes though the rate decreases as available surface area decreases (Bjørlykke and Jahren, 2015).

The origin of silica for the quartz cementation in sandstones is still poorly constrained and debatable though majority of the scholars seem to accept the internal source model, at which silica sources in sediments can be of? 1) pressure dissolution between detrital quartz grains and along stylolites (Fig. 3.2), 2) clay mineral transformations, 3) feldspar alteration reactions, and 4) dissolution of amorphous silica (Bjorlykke and Egeberg, 1993; Harwood et al., 2013; Jahren and Ramm, 2009; McBride, 1989). Transport of silica within sandstone formation is by diffusion and is limited distance only centimeters to few meters (McBride, 1989). Other alternative, external sources of silica from local shale units is also suggested (Day-Stirrat et al., 2010; Hower et al., 1976; van de Kamp, 2008).

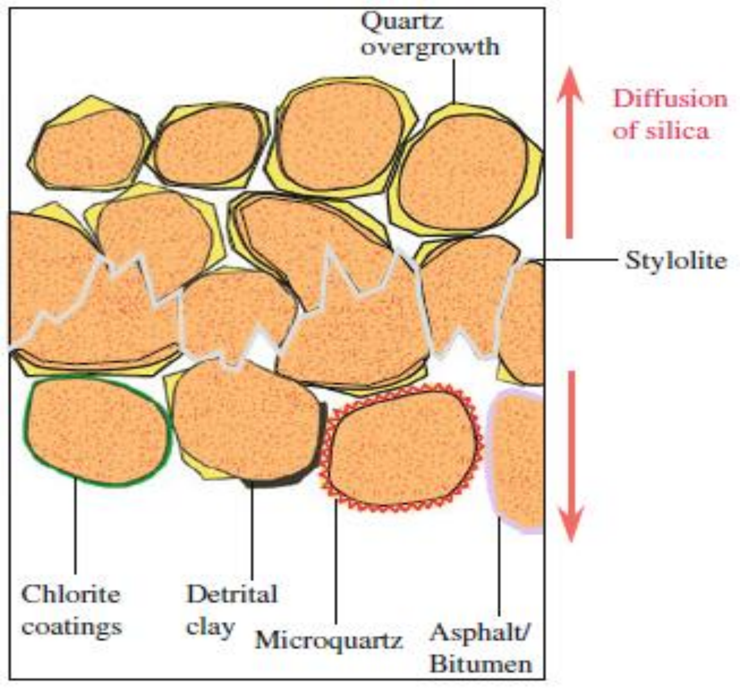

Figure 3.2: Schematic illustration of a stylolite; modified from (Bjørlykke and Jahren, 2015). Grains coatings of detrital clay, microquatz, chlorite, illite, iron oxide and bitumen showed how to retard quartz overgrowth.

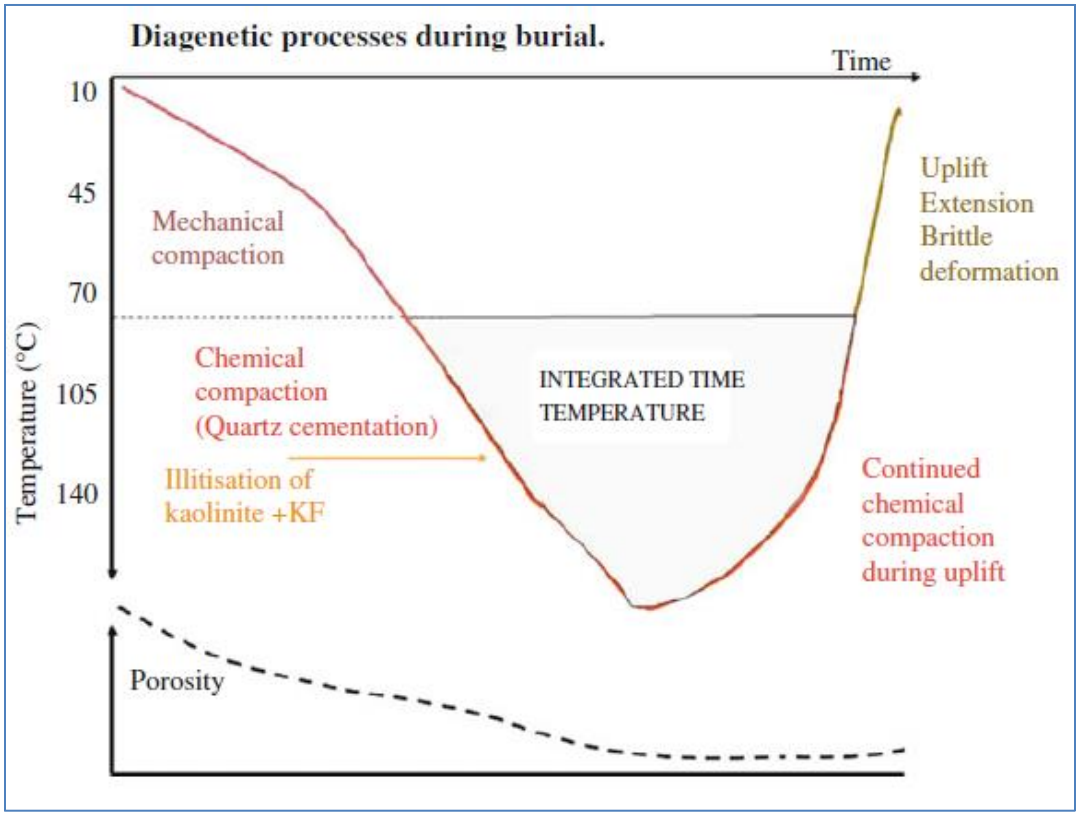

Figure 3.3: diagenetic processes, mainly, quartz cementation as a function of temperature and time. Quartz cementation will continue as long as the threshold temperature (70-80°C) during uplift. Modified from (Bjørlykke and Jahren, 2015)

Clay mineral transformations: Sandstones containing abundant clay matrixes have generally low reservoir quality as porosity is lost in relatively shallow burial depths (<1-2km) due to mechanical compaction (Bjørlykke and Jahren, 2015). Intermediate detrital clay content also increased the effect of mechanical compaction by enhancing sliding of sand grains and repacking though important in porosity preservation by hindering quartz cementation in deeper burial. While well sorted, quartz rich sandstones are best reservoirs; preserve much of its porosity from mechanical compaction to average burial depths of 2-3km. With increasing depth of burial and temperature, mineral alterations will occur due to the drive to more thermodynamically stable mineral assemblages. Illitization of kaolinite is an important diagenetic alteration, which occurs at deeper burial depths (Berger et al., 1997; Bjørlykke et al., 1986; Ehrenberg et al., 1992; Lanson et al., 1996) and has significant potential to change sandstone reservoir properties. It requires average temperature of 130°C and reaction needs potassium ion to proceed in most cases sourced from K-feldspar if present nearby (chemical equation 3.5) below (Bjørlykke and Jahren, 2015). In the absence of potassium, kaolinite remains stable even at higher temperatures. Authigenic illite has a fibrous, pore-filling appearance, which most importantly deteriorates reservoir permeability (Bjørlykke, 1998).

$KAlSi_3O_8 + Al_2Si_2O_5 = KAl_3Si_3O_{10} + 2SiO_{2\,(aq)} + H_2O$ -- (3.5)

K-feldspar Kaolinite Illite Quartz

Smectite is other important precursor for the precipitation of authigenic illite in sandstones and starts to transform at relatively lower temperatures than kaolinite and therefore shallow depths (Bjørlykke and Jahren, 2015). A mixed layer illite –smectite mineral form mostly described in the study of diagenetic change of smectite such as (Dypvik, 1983) based on observation in North Sea sediments suggest that I/S ratio depend primarily on temperature. Accordingly, illite content in the mixed layer mineral form increased from 30% of illite at temperatures of 65-75°C to >70% at temperatures of 80-100°C... In addition to temperature, presence of K^+ and time are important factors determining the rate of illite precipitation (Bjørlykke, 1998; Boles and Franks, 1979). Transformation of smectite to illite releases substantial amount of silica (chemical equation 3.6), (Bjørlykke, 1998), and precipitation of quartz cement facilitates the transformation (Peltonen et al., 2009).

Smectite + K-feldspar = Illite + Silica + Cations (Ca^{++}, Mg^{++}, Na^+) ---------------------------- (3.6)

Sandstones containing abundant smectite minerals are poor reservoirs from the beginning because of its high specific surface area and therefore high potential to absorb water. Illitization of smectites releases considerable amount of water, which can lead to the development of overpressure. In addition, illite has lower specific surface area, blocky and thick appearance in the mixed layer I/S form which contributes slight increase in reservoir porosity (Bjørlykke and Jahren, 2015). Albitization is other diagenetic phenomena (partial replacement of K-feldspar and/or plagioclase grains) though it has limited importance in the alteration of reservoir properties (Bjørlykke and Jahren, 2015).

3.2.4 Reservoir quality prediction

Primary Lithology (grain size, shape, sorting, detrital matrix content and composition) determines primary porosity during deposition and the modifications following burial depth (Ajdukiewicz and Lander, 2010; Bjørlykke and Jahren, 2015). Provenance, weathering/erosion processes, sediment transport, and depositional environment dictate the primary lithology and composition of sediment input. Poorly sorted sandstones lead to poor reservoir quality as it contains lower porosity from the start and losses much of its porosity during shallow burial depth due to overburden load. Well sorted, quartz rich, clean sandstones are rather most important reservoir rocks that have much capability of preserving porosity to great depths in effect of overburden compaction. It may have 30-35% porosities at 2-3km burial depths (Bjørlykke and Jahren, 2015).

Different processes right after deposition and during burial to few meters may generate both physical and chemical changes (near surface diagenesis). It may include biologic activity that disturbs initial layering and destroy primary sorting, introduce clay minerals that would have consequences during deeper burial. Meteoric water flushing of sand bodies generates authigenic clays depending on the primary K-feldspar or mica minerals content and degree of water percolation. Authigenic clays may appear lining pore spaces, pore/fracture filling, pseudomorphous replacements (Wilson and Pittman, 1977), (Fig. 3.4). Dissolution of calcareous products and precipitation of carbonate cement, addition of biogenic silica, and fecal products could change much of sandstone reservoir properties at shallow as well as deeper burial depths.

Mechanical compaction destroys much of sandstone porosities on burial to average depths of 2-3km. It is a function of vertical effective stress due to overburden load transmitted through the framework grains. A prediction of its effect is based on type of primary sediment input, as different lithology will respond differently. Experimental mechanics of different representative lithology are becoming popular on the analyses of mechanical compaction e.g. compaction of Etive sand (Marcussen et al., 2010), though time is critical. Well log, Petrographic and core porosity/IGV measurements from sedimentary basins of well constrained geothermal and subsidence histories are useful natural databases for predicting the effect of mechanical compaction with depth. Intergranular volume (IGV) measurements from well sorted, quartz rich, clean sand deposits buried to about 2km show an average of 26% (Paxton et al., 2002; Szabo and Paxton, 1991). Sandstones rich in ductile grains such as lithic fragments compact more and their abundances control IGV significantly through depth. Sandstone pore-fluid overpressures may reduce effect of compaction by reducing effective stress. However, if it only introduced before extensive mechanical compaction has occurred (Bloch et al., 2002; Paxton et al., 2002).

Porosity reduction of sandstones buried to greater depths to corresponding temperatures of 70-80°C is due to chemical compaction; predominantly quartz cementation grows onto detrital quartz grains and destroy porosity. Semi-quantitative prediction suggested based on the theory that quartz cementation is function of time-temperature, and quartz surface area available where newly formed quartz crystal is to nucleate (Walderhaug, 1994, 1996, 2000). Therefore, fine-grained sandstones will have higher value than coarse grained once and most importantly, presence of clay minerals lining detrital quartz grains (grain coating) determines the effect of quartz cementation. Most importantly authigenic clays (chlorite), microquartz crystals precipitated on grain surfaces and infiltrated detrital matrixes inhibit quartz cementation and have the potential to preserve higher porosities at much deeper burial depths (Bjørlykke and Jahren, 2015). Other chemical compaction product is illite precipitation. It has fibrous appearance and has significant effect on permeability. In addition, primary porosity can be estimated as a function of calculated IGV minus calculated cement abundance (Lander and Walderhaug, 1999).

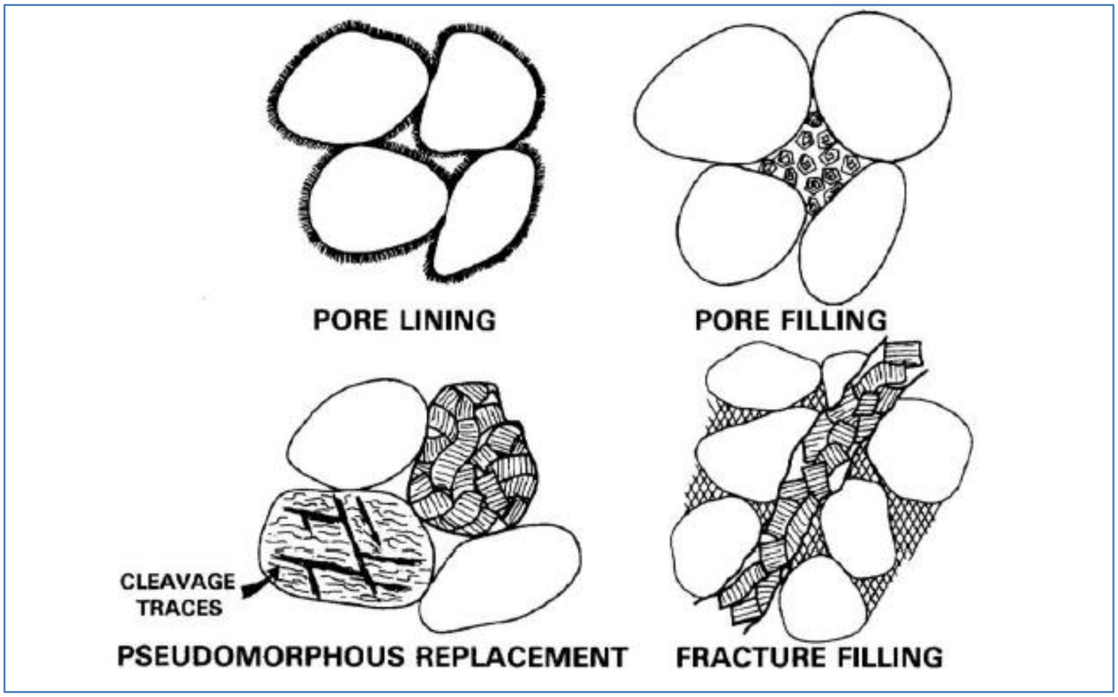

Figure 3.4: Common appearances of authigenic clays between sandstone grains (Wilson & Pittman, 1977). Image taken from (Hansen, 2016)

3.2.5 Rock Physics Diagnostics

Effective medium models of mixtures of sediment grains and porosity of sandstones have been developed to establish the relationship between elastic moduli and porosity fractions of sandstones. Two theoretical models (Dvorkin and Nur, 1996) the ‘contact-cement model’ and ‘Friable sand model’ for high porosity sands (Avseth et al., 2000). The former assumes porosity reduction from the initial porosity of a sand pack is due to uniform deposition of cement layers on grain surfaces. This will result in dramatic increase in the stiffness of sand by reinforcing the grain contacts nevertheless of significant porosity reduction (Fig. 3.5). The later model assumes that porosity reduction due to deposition of solid matter away from grain contacts, which weakly affects the stiffness of the rock. A combination of the two- ‘constant cement model’ assumes sands of having the same amount of contact cement but variable porosity due to varying amount of pore filling cement (Avseth et al., 2000).

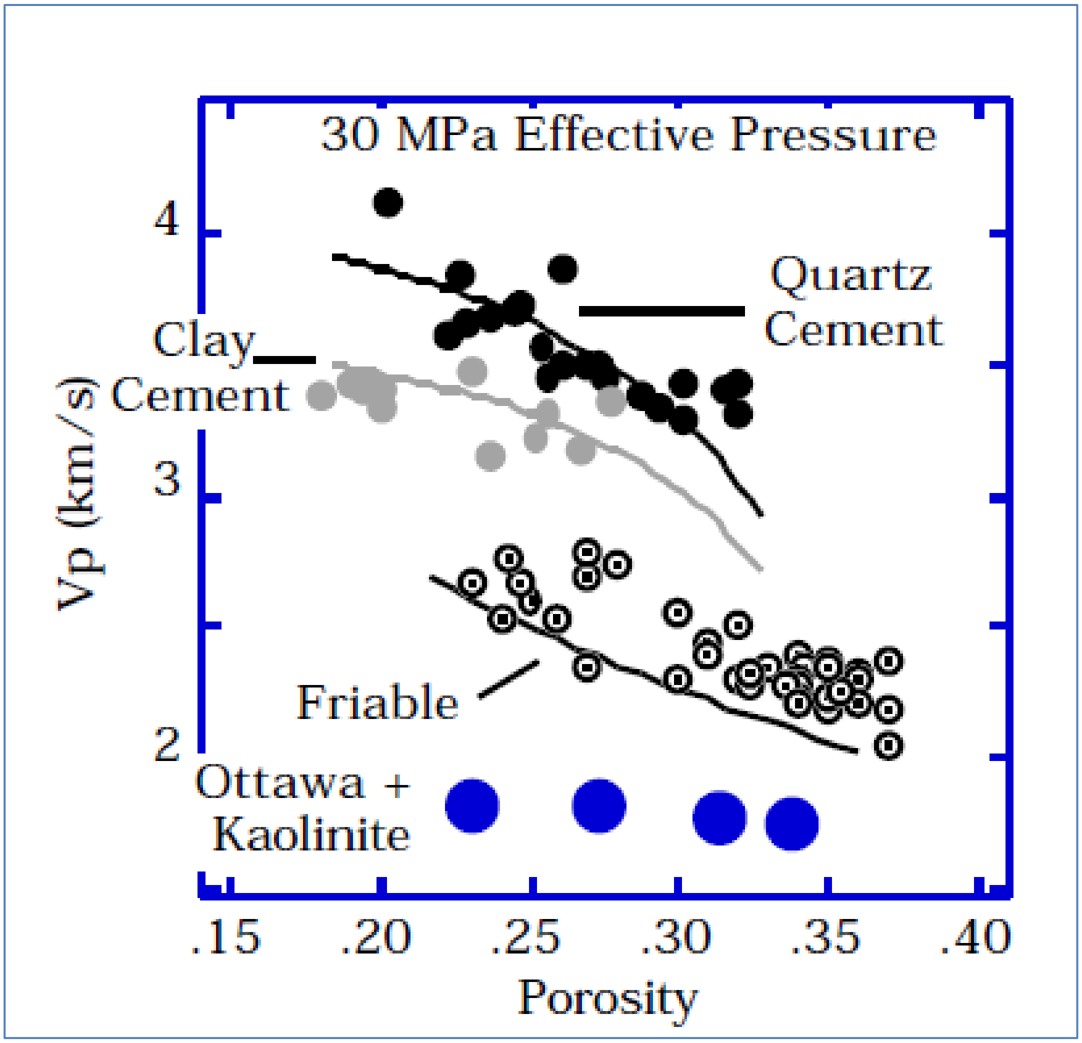

Figure 3.5: Elastic wave velocities versus porosity cross-plot of quartz, clay cemented and friable North Sea sands (Avseth et al., 2000), with superimposing model curves discussed in (Dvorkin and Nur, 1996); and handmade Ottawa sand and kaolinite mixture from (Yin et al., 1993). All data are for room dry samples at 30 MPa differential pressures. Figure modified from (Avseth et al., 2000)

4 MATERIALS and METHODS

4.1 Introduction

Drilled core samples and geophysical well logs were used for a geologic, petrographic and petrophysical study of the reservoir sandstone Stø Formation. The data regarding the two wells (7119/9-1 and 7119/12-2) were obtained from Norwegian Petroleum Directorate (NPD) core store and the University of Oslo. Wells general information is taken from NPD fact sheet pages (Table 4.1).

In total 27 thin sections from both wells marked in (Fig. 4.1) with a background gamma ray log image were studied under transmitted light microscope to recognize mineralogical composition and textural properties. In addition, petrographic (SEM) was used to analyze the texture and morphological appearances and types of authigenic phases in the sandstones. An x-ray diffraction analysis was performed for a bulk mineral composition determination of 16 powder samples. DIFFRAC-EVA software program was used for phase identification while quantitative analyses of the constituent minerals were done using Profex-BGMN bundle (Doebelin and Kleeberg, 2015). Petrophysical interpretation and analyses of given geophysical well logs (Table 4.2) was performed using PETREL and HRS software. Geological interpretation was recorded based on conventional sediment logging of core samples.

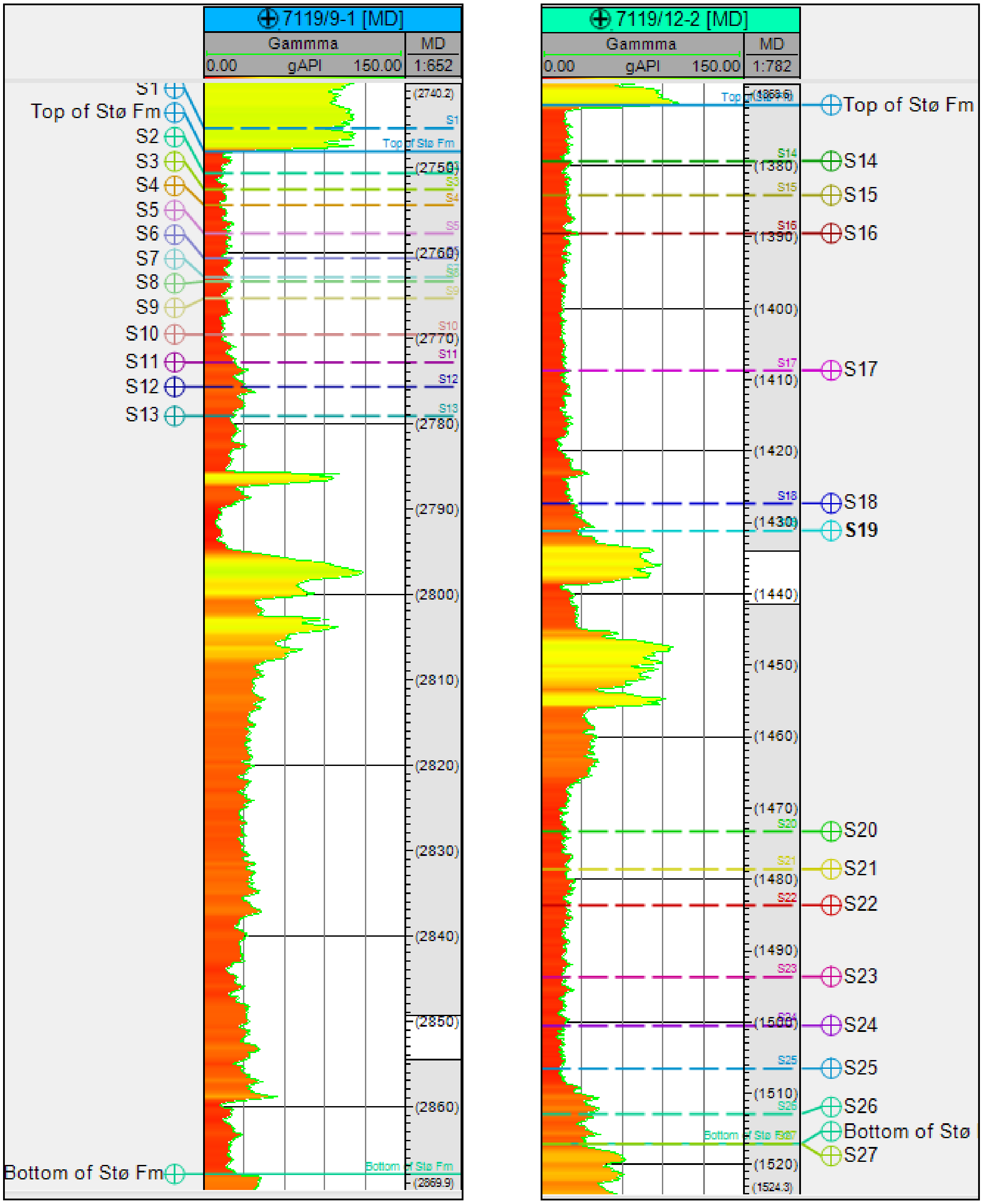

Figure 4.1: Thin section samples from well 7119/9-1 (left) and 7119/12-2 (right) overlapped to their corresponding Gamma Ray logs.

Table 4.1: General well information taken from NPD fact pages (NPD, 2017)

Well information	Well 7119/9-1	Well 7119/12-2
Location (degrees)	71° 24' 53.19" N 19° 49' 43.26" E	71° 0' 51.81" N 19° 58' 20.81" E
Type/purpose	Exploration/wildcat	Exploration/wildcat
completed date	25,09,1984	26,06,1981
content	dry	Oil shows
water depth(m)	201.0	180.0
Kelly Bushing elevation (m)	25.0	25.0
Total depth (MD), [m-RKB]	3248.0	1902.0
Maximum inclination [o]	0^o	0^o
Stø depth interval (MD), (m)	(2748-2868)	(1372-1517)
Bottom hole temperature [°C]	112	62

Table 4.2: Geophysical well logs from wells 7119/9-1 and 7119/12-2 and recorded depth intervals (NPD, 2017)

Well Logs	Well 7119/9-1 Depth interval (m)	7119/12-2 Depth interval (m)
Gamma Ray .gAPI	218-3247	179-1902
Density Correction .g/cm3	240-5247	236-1900
Density g/cm3	240-3247	236-1900
Neutron .m3/m3	2719-3248	236-1900
Sonic .us/m3	295-3248	179-1902
Resistivity (deep) ohm.m	295-3248	179-1902
Resistivity (medium) ohm.m	295-3248	179-1902
Resistivity (shallow) ohm.m	2719-3248	378-1902
Caliper .in	240-3247	236-1900

4.2 Petrographic analyses

4.2.1 Point count - (Transmitted light microscope)

In total of 27 thin section samples were studied under petrographic analyses. 13 of them are from well 7119/9-1 representing only the upper part of Stø Formation, 14 from well 7119/12-2, well represented the whole Stø Formation (Fig. 4.1). A point count of 300 points per thin section was performed in a transmitted light, polarizing microscope (Nikon) and a swift counting machine for the mineralogical content analyses and porosity. Mineral compositions of framework grains, porosities (primary, secondary), matrix content, and amount of diagenetic cement were investigated. In addition, intergranular volume computed which can be used to measure degree of compaction.

4.2.1.1 Framework grain composition and sandstone type

Point counting was performed mainly to determine porosity, framework grain mineral composition, matrix content (detrital, authigenic clay, and cement), and analyze other minor constituents. Framework grains composition and their relative distributions used to describe the type of sandstone. The Pettijohn sandstone classification scheme was used for this analysis. Proportions of framework mineral grains (quartz, feldspar and lithic fragment) computed will be compared with the ternary diagram (Fig. 4.2). The third dimension of the Pettijohn classification scheme used to classify sandstones based on the increasing percentage of matrix content. Accordingly, Sandstones containing less than 15% matrix are called Arenites, between 15-75% Wacke while clastic sedimentary rocks more than 75% matrix content are mud rocks. In this classification method, less important components (mica, biogenic and other minor minerals) are disregarded in the ternary diagram (Nichols, 2009).

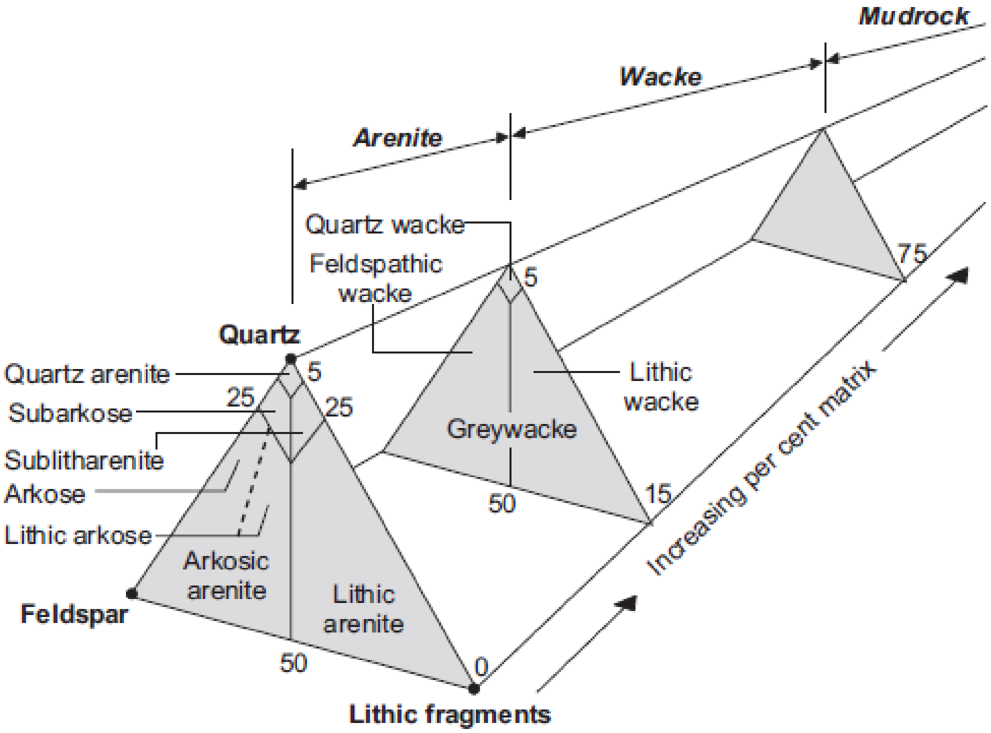

Figure 4.2: Pettijohn classification scheme of sandstones (Pettijohn, 1957), image is taken from (Nichols, 2009)

X-ray powder diffraction: In total of 16 bulk samples were analyzed for the identification of bulk mineral compositions. This was done in order to identify sediment mineralogical composition and to complement SEM and Optical microscope analyses.

Small representative rock samples were considered for the analyses of the bulk mineral composition. Small rock samples were crushed and ground in a grinding machine, which reduce grain sizes to less than 500microns. An alcohol was used to clean and avoid contamination in every run of sample powdering. A 3.0-3.5g of these powdered samples was mixed with 8 ml of ethanol into the sample jar filled with 48 grains of agate and micronized for 12minutes. This further reduced size of powder to approximate 10microns and better homogenization. Micronized powder put into an oven with a temperature of 60^{o}C and left for drying. Milled and dried powder carefully filled into small, plastic holders and pressed to have smooth, flat surface in level of sample holder. Prepared samples were put into X-ray diffractometer machine -Bruker D8 Advance equipped with Lynx eye detector –and Cu Kα tube.

4.2.1.2 Texture-Grain size

For the grain size analyses, measurement of 100 grains per thin section was performed on a transmitted light microscope and using Lumenera INFINITY ANALYZE software. It uses camera-captured images, calibrated to microscope object lenses (4x, and 10x calibration). Measured grain diameters in each thin section sample were transformed into a phi-scale (Krumbein Phi scale) for further grain size distribution analyses using Formula 4.1 below, negative logarithm of particle diameter D to base 2. It changed fractional measurements into integer numbers. This is for convenience of making visually interpretable graphical plot and for statistical calculations (Boggs, 2009).

$$\emptyset = -logD \text{ -- } (4.1)$$

Where, $\emptyset$ = grain size (Phi scale), D = particle diameter (mm)

Folk’s cumulative frequency curves were used for visual analyses of grain sizes distributions (e.g. Fig. 4.3) and for the calculations of statistical distribution parameters such as sorting, and skewness using graphic methods (Fig. 4.4). Sorting describes the range of grain sizes present and measures the degree of spread or scatter of these grain sizes around the mean grain size (Boggs, 2009). Similarly, skewness is another measure of spread of grain sizes that measures sorting around the tails of distribution curves. Qualitative analyses of cumulative curve are based on the proportion of grain size distributions relative to a particular grain size, which describes sorting. The steeper the graph is better the sorting (Bjørlykke, 2015). Statistically, sorting and skewness were computed employing the method called Folks cumulative curve formulas 4.2 and 4.3 (Folk and Ward, 1957). An arithmetic average used to calculate mean grain sizes and excel was used for computations. Moreover, Verbal descriptions were used for the description of range of calculated parameters (Table 3.).

Sorting

$$\sigma i = \frac{\emptyset 84-\emptyset 16}{4} + \frac{\emptyset 95-\emptyset 5}{6.6} \text{ --- } \tag{4.2}$$

Skewness

$$SKi = \frac{\emptyset 84+\emptyset 16-2\emptyset 50}{2(\emptyset 84-\emptyset 16)} + \frac{(\emptyset 95+\emptyset 5-2\emptyset 50)}{2(\emptyset 95+\emptyset 5)} \text{ ------------------------------------ } \tag{4.3}$$

$\emptyset_5$, $\emptyset_{16}$, $\emptyset_{50,}$ $\emptyset_{84}$, and $\emptyset_{95}$ are grain sizes (phi-scale), corresponding to the index cumulative percentage values, as graphically indicated in Figure 4.4.

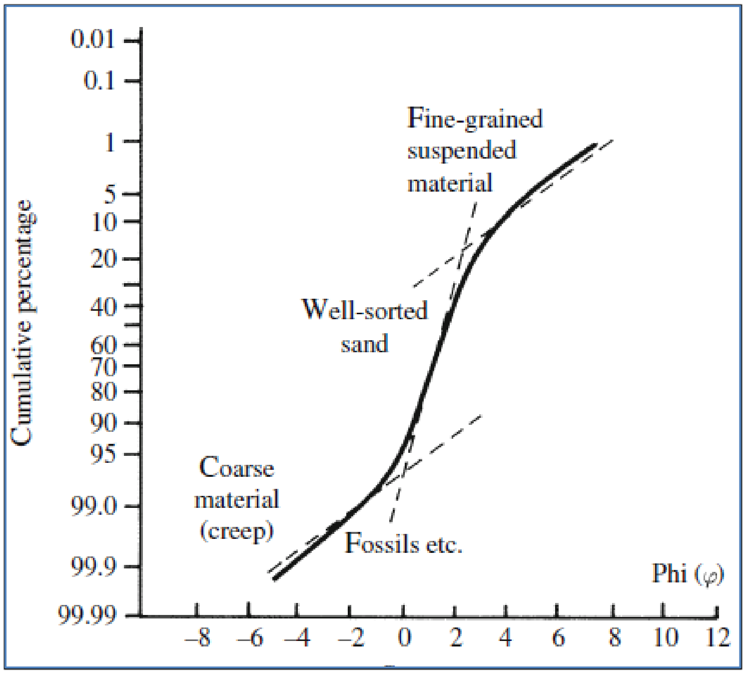

Figure 4.3: Grain size distribution curve, cumulative percentage versus grain size (Phi-scale), and qualitative description of curve shape. Image modified from (Bjørlykke, 2015)

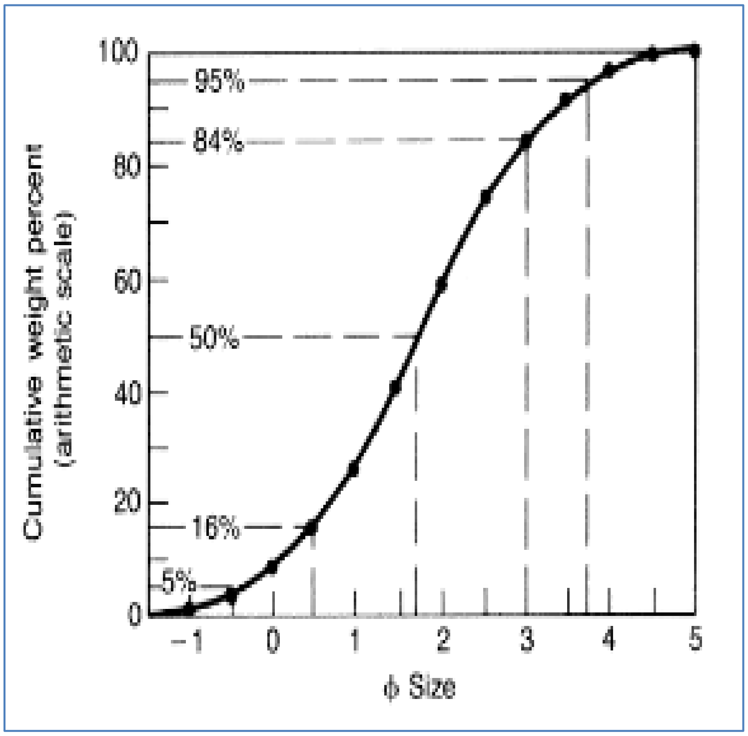

Figure 4.4: Figure shows graphic method for calculating grain size percentile values from a cumulative curve. Image modified from (Boggs, 2009)

Table 4.3: verbal terms used to describe interval values of calculated sorting (left) and skewness (right) after (Folk, 1980).

Sorting- inclusive graphic standard deviation	
Phi standard deviation	Verbal sorting
<0.35σ	Very well sorted
0.35-0.50σ	Well sorted
0.50-0.71σ	Moderately well sorted
0.71-1.00σ	Moderately sorted
1.00-2.00σ	Poorly sorted
2.00-4.00σ	Very poorly sorted
>4.00σ	Extremely poorly sorted

Skewness-inclusive graphic skewness	
Calculated skewness	Verbal skewness
> +0.30	Strongly fine skewed
+0.30 to +0.10	Fine skewed
+0.10 to -0.10	Near symmetrical
-0.10 to -0.30	Coarse skewed
<-0.30	Strongly coarse skewed

4.2.1.3 Texture-Grain shape

Sediment surface textures describe sedimentary processes that sediment grains underwent. It includes such as roundness, and smoothness which can express degree of sediment grain exposure to abrasion, like the more rounded grains may indicate long period of sediment transport history before settling. Whereas grain sphericity is, measure of closeness to spherical shape and shows type of original weathering product (Nichols, 2009). Grain fabric describes grain-to-grain relationships such as spatial distribution, geometric, and orientation with the effect of type of depositional environment. Grain contact is one that describes spatial grain-to-grain relations and has the effect from mechanical compaction through burial beyond the effect of sedimentation processes.

In this study, standard images were employed for the qualitative description of grain surface textures such as grain roundness, sphericity, and grain contacts (Fig. 4.5, 4.6). For statistical distribution analyses, 100 sediment grains per thin section sample were analyzed in a transmitted light microscope fitted with an infinity video camera. The descriptive terms such as roundness were plotted in a frequency curve graphs (Histograms) for statistical distribution analyses.

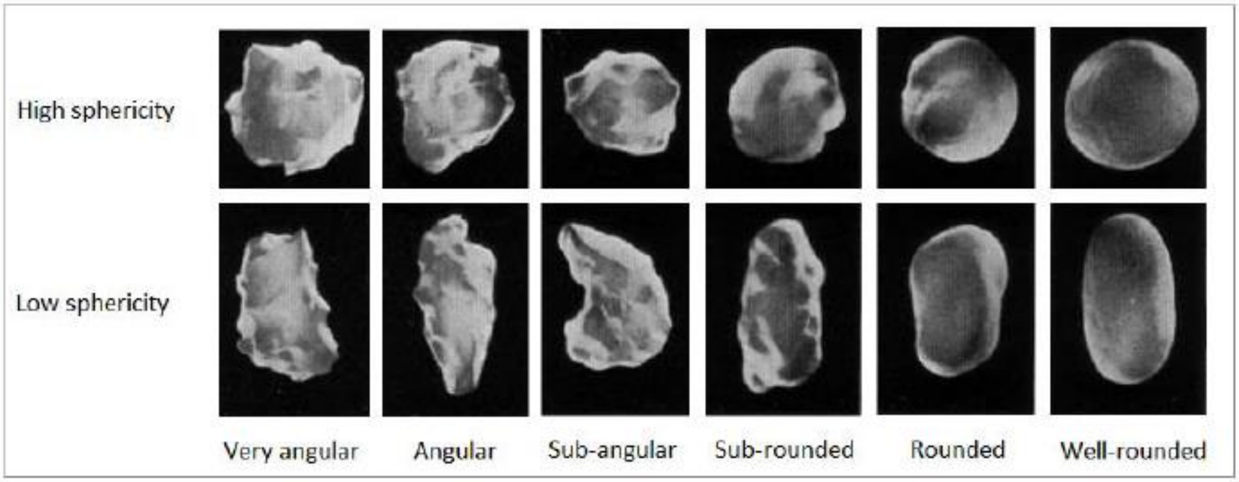

Figure 4.5: Figure displays standard images used to determine grain shape under optical microscope after (Powers, 1953). Figure taken from (Hansen, 2016)

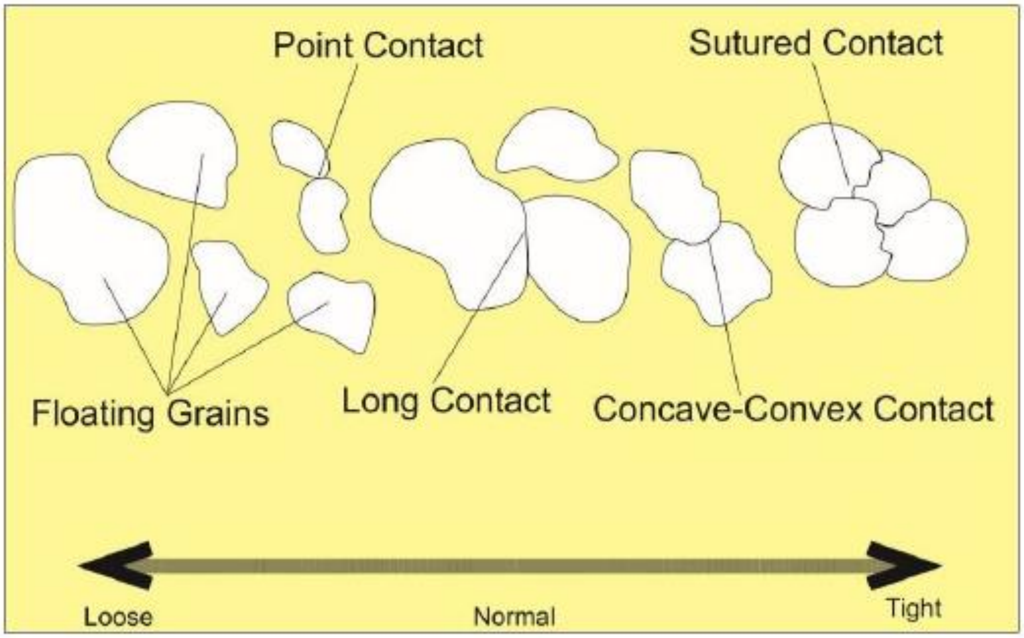

Figure 4.6: Schematic cartoon used for performing grain contact analyses (Santin et al., 2009). Image taken from (Hansen, 2016)

4.2.2 Scanning Electron Microscope and Cathodoluminescene (CL)

For detailed analyses of clay minerals and other mineral grains difficult to characterize under optical microscope carbon coated thin section samples were examined under scanning electron microscope (SU5000, 15 kV accelerating voltage). X-ray elemental mapping done to recognize grain coating clay minerals that could limit quartz cementation. A CL analysis was performed in some thin sections from both wells to investigate authigenic quartz cement. High performance CL microscopy-delmic spark advanced CL system was used for this analysis.

4.3 Geological interpretation using sediment core logging

An observation of sedimentary structures, texture, and bioturbation as well as biogenic content of core samples from both wells was made at the Norwegian Petroleum Directorate core store in Stavanger. Geological interpretation were recorded on a standard logging sheet and digitized using Adobe Illustrator Software as displayed in appendix-1. Different types of sedimentary facies were recorded and depositional environments were interpreted based on sedimentary facies associations.

4.4 Petrophysical Interpretation

PETREL and Hampson Russel Software (HRS) were employed for the petrophysical interpretation and analyses in the two study wells (7119/9-1 and 7119/12-2). The main goal of the analyses is to describe as well as correlate lithology of Stø Formation, estimate shale volume, which have detrimental effects in reservoir quality and estimate porosity. Mainly the gamma ray log was used for lithological analyses, correlation, and shale volume estimation. Neutron porosity and density crossover additionally used to identify if hydrocarbon containing sand is present. Porosity calculated from density log and total porosity derived using an averaging formula with neutron porosity. Sonic logs transformed into velocity logs and metric units for the use of compaction trend analyses. Transition zone from between mechanical and chemical compaction zone was delineated as well. Published natural and experimental compaction trends were used for uplift and exhumation estimation by overlapping with velocity logs. Finally, rock diagnostics chart was used to analyze cementation, porosity reduction; by the use of velocity, versus total porosity cross plot.

4.4.1 Lithological Interpretation and correlation

Gamma ray logging is a continuous recording of natural gamma radiation emitted from formation rocks. Most importantly Potassium (K^{40}), isotopes of Uranium-Radium and Thorium spontaneously emit such radiation. Lithological discrimination is based on shales are presumed to contain more radioactive elements (K^{40}). Generally shale, black shale and volcanic ash give higher gamma ray readings while halite, anhydrite, coal, clean sandstones, limestone/dolomite have the lowest values (Mondol, 2015). However, overgeneralizations would lead to wrong interpretations, like sandstones rich in feldspars, mica, heavy minerals, and greywacke or glauconitic, could show higher values. Therefore, gamma ray was used with other well logs to accurately distinguish between shale and non-shale formations. Density log versus neutron porosity crossover was used to identify hydrocarbon saturated sand formations. High negative separations between crossovers occur when oil/gas saturated sandstones existed. Gamma ray log has high vertical resolution that makes it capable to identify thin beds, which makes it suitable in correlating lithologies and depth matching between different logging runs. Moreover, Gamma logs used to infer litho-facies and deposition environments as shalliness naturally changes gradually and develop characteristic shapes in different depositional systems (Fig. 4.7), (Mondol, 2015).

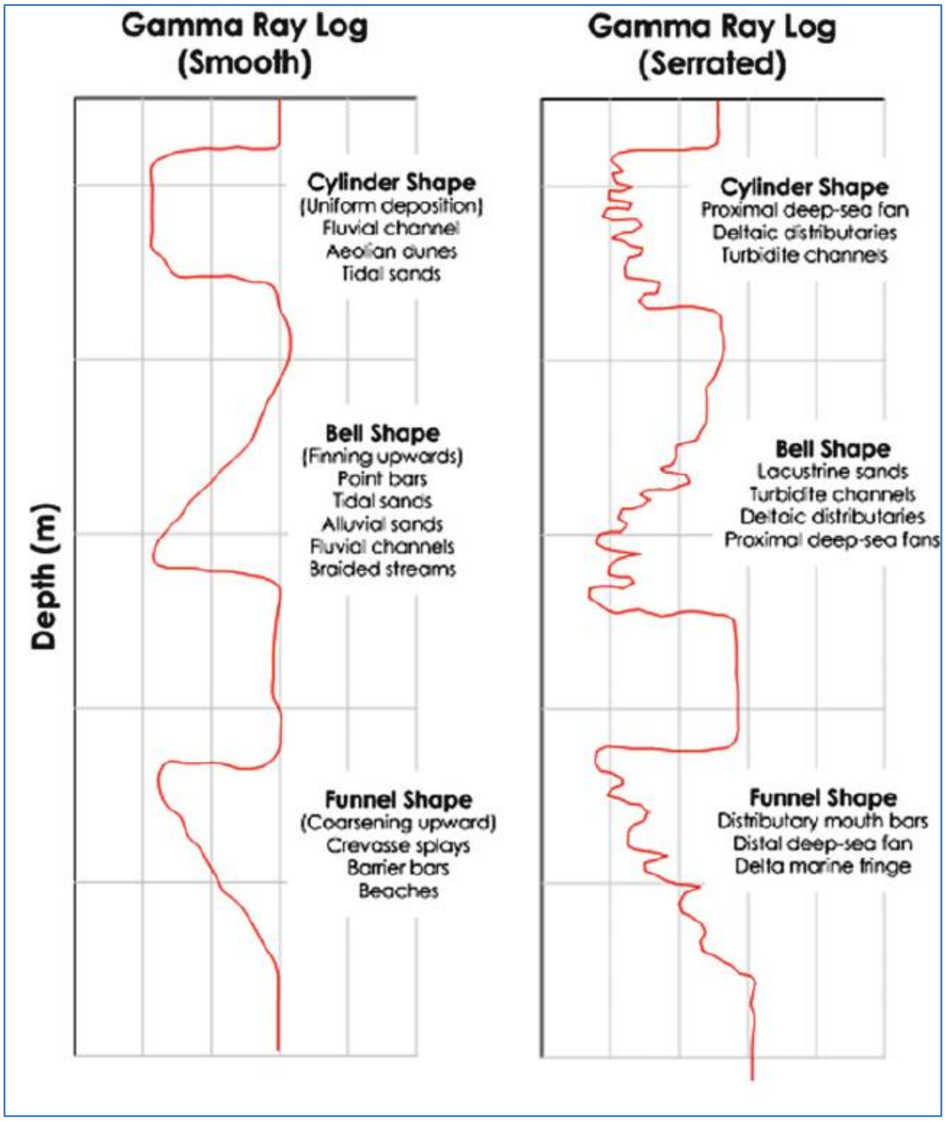

Figure 4.7: Summary of gamma ray log responses used in depositional environment and facies interpretation, image taken from (Mondol, 2015).

4.4.2 Shale volume estimation

To discriminate between reservoir and non-reservoir rocks the threshold value of shale volume is used most often (Mondol, 2015). It is computed in two steps: first by calculating the gamma ray index (Formula 4.4):

$$\mathbf{GR_I = \frac{GRlog - GRmin}{GRmax - GRmin}} \quad \text{---} \ (4.4)$$

Where GRI is gamma ray index, GRlog is gamma ray reading, GRmax is maximum gamma ray reading (usually mean maximum through shale/clay formation), and GRmin is minimum gamma ray reading (usually mean minimum reading through clean sand, carbonate formation).

In the second step GR_I, values are entered into the chart (Fig. 4.8), to read corresponding shale volume. Chart contains linear and nonlinear relationships of GR_I and shale volume, in which the nonlinear once will give reduced volume estimation. The Stieber relationship was used for analyses in this study (Formula 4.5):

$$\boldsymbol{Vsh_{Stieber} = \frac{GRi}{3 - 2GRi}} \quad \text{---} \ (4.5)$$

Where $Vsh_{Stieber}$ is calculated shale volume, GRi is gamma ray index.

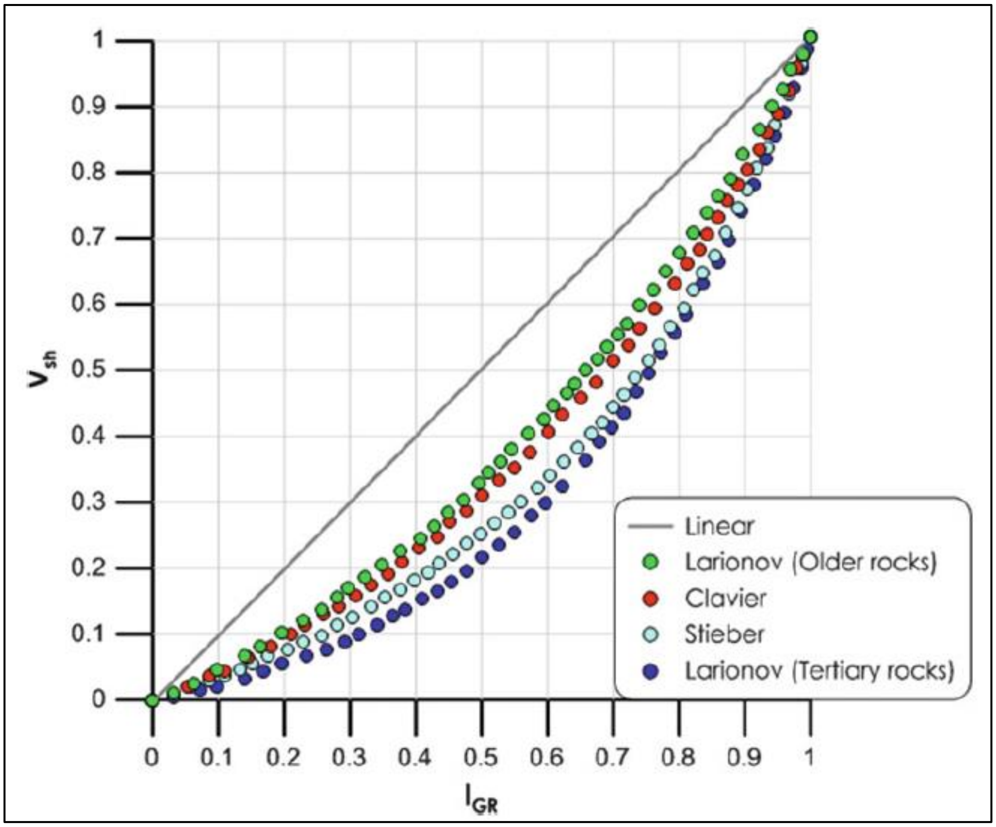

Figure 4.8: Figure displays chart used for corrected shale volume estimation after gamma ray index computed, image modified from (Mondol, 2015).

4.4.3 Porosity Estimation

Porosity calculated from density and neutron porosity logs. First porosity from density is calculated (Formula 4.6):

$$\emptyset\text{den.} = \frac{\rho_{\text{solid}} - \rho_{bulk}}{\rho_{\text{solid}} - \rho_{\text{fluid}}} \text{ --- } (4.6)$$

Where $\emptyset_{\text{den.}}$, is calculated porosity from density log, ρ_{solid} is density of total solid constituent (framework and matrix), ρ_{bulk} is the measured formation density, and ρ_{fluid} is density of formation fluid.

Density of quartz (2.65 g/cm^3) is commonly used for the solid density in sandstone reservoirs assuming clean sand. Fluid density is usually formation water (1.025 g/cm^3). If pore filling fluid is found to be oil or gas, using water as density of fluid will lead to an overestimated porosity. Using combinations of porosity logs such as neutron log is usually used technique for better porosity estimation (Mondol, 2015). It is a technique that measures concentration of hydrogen ions present, which is indirectly used to measure porosity because most importantly ions of hydrogen associated with pore fluids. However, hydrogen ion can exist in solid part of formation rocks such as clay bound water; therefore, shaly sandstones will give higher readings of neutron porosity, called shale effect. If gas is pore-filling fluid, porosity estimation from neutron log will be underestimated due to less concentration of hydrogen ions (Mondol, 2015). An averaging formula (Formula 4.7) is often used to compute total (true) porosity from combinations of density and neutron porosity logs. By doing this, the effect of predicted lithologies will be reduced (Mondol, 2015).

$$\emptyset total = \sqrt{\frac{(\emptyset d)^2 + (\emptyset n)^2}{2}} \text{ --- } (4.7)$$

- $\emptyset_{total}$ = calculated porosity
- $\emptyset_d$ = porosity from density
- $\emptyset_n$ = neutron porosity

4.4.4 Compaction Trend analyses

Two main goals of compaction trend analyses are identifying probable transition zone between mechanical and chemical compaction effects and Uplift and exhumation estimation using acoustic property measurements (sonic-log). Temperature gradient was calculated to validate identified transition zones and uplift estimates in correlation to literatures and experimental results. Table 4.4 summarizes measured bottom-hole temperature (BHT), and calculated geothermal gradients. Average 4^{o}c of mean Sea temperature was used, and depths in kilometers for the computation of gradients in both wells (Formula 4.8).

Table 4.4: summaries measured bottom-hole temperatures and computed geothermal gradients in study wells

Type	Well 7119/9_1	Well 7119/12_2
Mean Sea Temperature (^{o}C**)**	4	4
Bottom Hole Temperature (^{o}C), TVD(km)	112**,** 3.25	62**,** 1.90
Geothermal Gradient (^{o}C/km)	33.23	30.53

$$\mathbf{Ggradient} = \frac{\boldsymbol{BHT-MST}}{\boldsymbol{TVD-MSL}} \text{--} (4.8)$$

- Ggradient= calculated geothermal gradient, BHT = bottom hole temperature, TVD = true vertical depth (km), MST= mean sea temperature, and MSL = mean sea level

Trend analyses is based on the generalization that sediment compaction upon burial consolidates sediment particles, and physical properties change with depth systematically for a specified lithology and under certain conditions. Compaction due to overburden stress drives into reduced porosity, increased bulk density, and elastic properties (velocity) with increasing depth (Bjørlykke and Jahren, 2010). Factors such as high sedimentation rate during deposition creates over pressured zones, which have potential to resist stress due to overburden load and may cause measurement of properties out of trend at deeper depths. Early carbonate cementation consolidates sediments and stiffening which can give high acoustic property measurements at shallower depths. Otherwise, compaction due to overburden stress brings predictable property changes upon depth such as porosity, and velocity. It is function of effective stress and consolidates sediments by forcing sediment particles coming together, deform and crush to establish mechanical stability. Moreover, this process can continue to average depths of 9km such as in cold sedimentary basins depending on the type of sediment composition where cementation due to elevated temperature is absent (Bjørlykke and Jahren, 2015).

Chemical compaction affects the nature of sediment grains upon burial (Bjørlykke and Jahren, 2010). It is function of temperature, where solid materials dissolve and precipitate to fill pore spaces between sediment grains. Instead of close packing of grains, it stabilizes by filling the space between and increases dramatically elastic properties. Quartz cementation is the most important chemical compaction, which occurs to average burial depths of 2500m in a normally subsided sedimentary basin. It overtakes consolidation of sediment layers, e.g. in sand formations, 2-4 % of quartz cement is believed to effectively stop mechanical compaction (Bjørlykke and Jahren, 2015).

Experimental compaction trends of specific materials e.g. kaolinite-silt 50:50 combinations after (Mondol, 2009) was used to correlate with measured velocity logs of shaly intervals in both wells (7119/9-1 and 7119/12-2). A rough estimation of uplift and exhumation performed likewise to figure shown below (Fig. 4.9). Other established natural compaction trends such as based on Etive sand (Marcussen et al., 2010), and experimental compaction trends of specific clay compositions and combinations (Mondol et al., 2007) are commonly used as well.

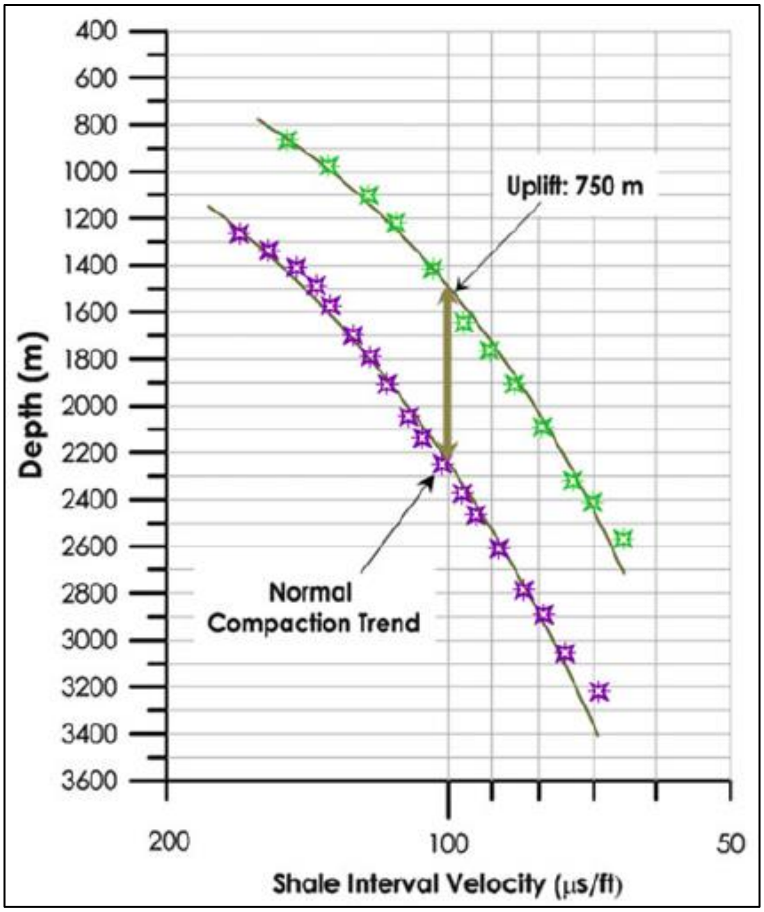

Figure 4.9: Figure displays estimation technique of uplift and exhumation in shale sequences, image modified from (Mondol, 2015)

4.4.5 Rock Physics diagnostics

Total calculated porosity versus velocity log cross-plots were used for rock physics diagnostic analyses of the Stø Formation in both wells. Cross plots were superimposed with effective medium models, which establish the relationship between elastic wave velocity and porosity of sandstones. Qualitative analyses of the status of quartz cementation and estimation of amount of quartz cement volume was performed.

Procedure

- Velocity log from well 7119/9-1 was transformed into water-saturated case using the Gaussian fluid substitution method, employing HRS. This is because presence of gas was indicated by the high negative separation between density and neutron porosity logs crossover and from well completion reports (NPD) a kick accompanied by up to 14% background gas (C1 to C4), at the depth of 2744m, just above the upper reservoir zone, when circulating out. Initial 20/80% of gas and water saturation respectively was assumed, where as other parameters kept default values. Velocity log from well 7119/12-2 used without transformation assuming 100% water saturated case.

- Velocity log and total calculated porosity data inserted into Excel, cross-plotted by superimposing rock diagnostic sand models.

- Qualitative analyses of the degree of cementation and quantitative estimation were performed.

Graphic method of cement volume estimation (Hossain and MacGregor, 2014) was used for the quantitative analyses (Fig. 4.10). It is physical based approach to quantify amount of contact and pore-filling cement by combining three rock physics models: the soft sand model, stiff sand model (Mavko et al., 2009) and intermediate stiff sand model (Hossain et al., 2011; Mavko et al., 2009). Cement estimation is based on drawing a line from data point (blue dot) along the intermediate stiff sand model to the end at the stiff sand model curve. Horizontal intercept of line directly measures amount of pore filling cement, whereas intercept up to the maximum porosity measures amount of contact cement.

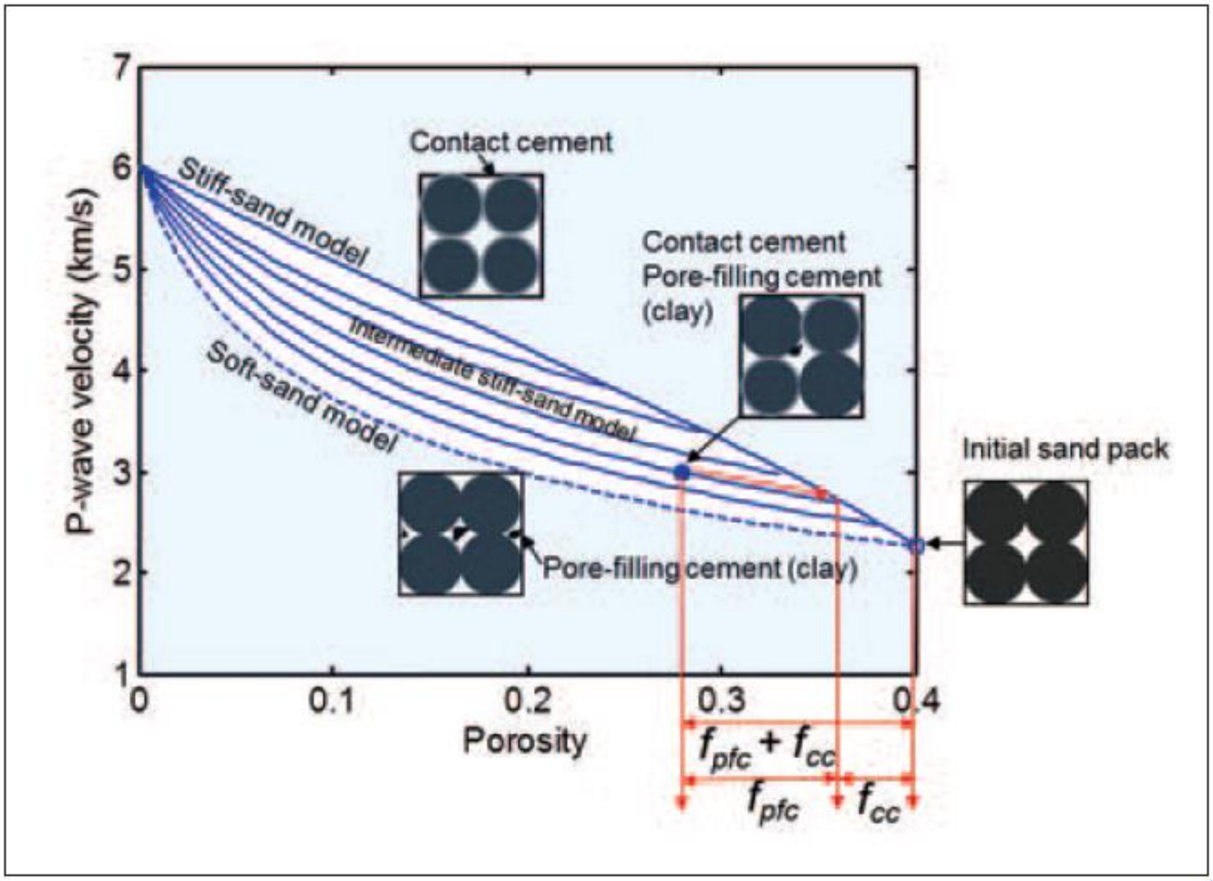

Figure 4.10: Figure displays methods of quantitative cement analyses, f_{cc} – fraction of contact cement, f_{pfc} –fraction of pore-filling cement. The stiff sand model explains theoretically stiffest way to add with initial sand pack, the soft sand model explains the theoretically softest way to add pore filling minerals, and the intermediate stiff sand model describes both initial contact cementation and noncontact cement, after (Hossain and MacGregor, 2014).

5 RESULTS

5.1 Sediment Core Observation

The Stø Formation can be subdivided into two sand units occurring in stratigraphic order: 1) lower sand unit and 2) the upper sand unit. These two sand units are characterized by distinct intervening shaly horizons (Fig. 5.1). Only the upper sand unit of the Stø Formation is cored in well 7119/9-1 (two conventional cores in the depth range of 2745m to 2779.3m), while in well 7119/12-2 both sandstone units are recognized. This well consists of four conventional cores where samples were collected between 1517.39-1473m, and six cores between 1433.5-1378.5m intervals. Conventional core logging was performed on both wells (Appendix 1A and 1B, respectively). Table 5.1 shows the summary of the facies associations and interpreted depositional environments. This is based on the recorded details in the sediment core logs including sedimentary structures, trace fossils, bioturbation, grain size, and biogenic content.

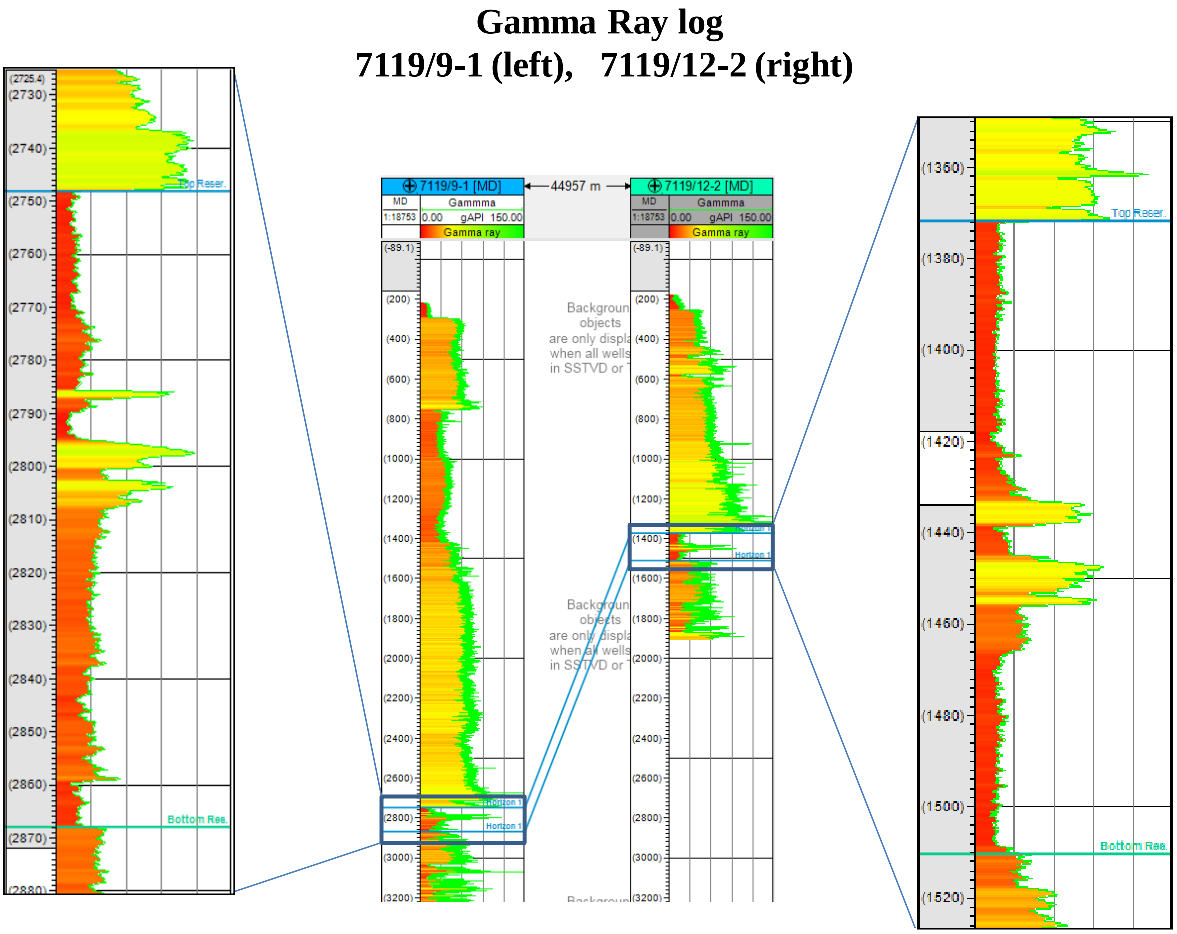

Figure 5.1: Plot of gamma ray log of well 7119/9-1 and 7119/12-2 with an inset showing the Stø Formation i.e. the focus of this study. As it is illustrated in the logs, two sand units with intervening shaly horizons characterize the Stø Formation.

Table 5.1: Summary of facies associations and interpreted depositional environment for the Stø Formation

Facies associations	Grain size	bioturbation	descriptions	Depositional environment
FA-1	medium to coarse grained sand	Intermediate	- Plane parallel and cross laminated structures, mud drapes and fossil fragments in the coarse grained intervals - Uni-directional and bi-directional ripple marks, millimeter scale deformation structures in the finer and coarser sand interlaminations, trace fossils	- Fluvial, tidal distributary channel fill influences in an interchanging proximal lower to upper shore face environment
FA-2	Medium grained sand	Little/null bioturbation	- Mostly structureless, lighter sand with few low angle planar cross laminations and uni-directional ripples - limited trace fossils, some hard shell fragment body fossils	- Near shoreline swash and low energy environments
FA-3	Very fine sand	Intermediate to strong bioturbation	- Massive, condensed intervals intercalated with strongly bioturbated, dark muddy sand	-Proximal lower shore face

FA-1

Facies association-1 is composed of fine to medium grained sandstones with characteristic burrows, which destroys sedimentary structures and also thin mud laminations, and some wavy bedding with double mud drapes in the finer intervals, and organic draped plane parallel and cross-laminated sand interval in the coarser intervals. Some preserved plane parallel laminations in the fine-grained sand, which could suggest relatively low energy depositional regime. Some dark painted conglomeratic lag, containing some wood fragments seen to form a sharp contact with the bioturbated finer sand. The bioturbated intervals are clear indications where sediment input is restricted allowing organisms to burrow. These could suggest sandstone deposition in a shifting sedimentary environment of high and low energy regime typically in the tidal dominated shore face realm. This facies association is dominantly occurred in the lower sand unit and 2-3m at the bottom part of the upper sandstone unit in well 7119/12-2.

FA-2

Facies associations-2 is composed of medium grained, lighter color, friable sand of dominantly structureless and limited plane parallel and low angle cross lamination structures. Very rarely observed planar and trough ripple marks, hummocky cross stratifications. Centimeter scale conglomeratic, scoured bases also observed. It has little organic fragments content, some hard shell fragments such as bivalves and rarely seen root like features. The degree of bioturbation (borings) in this facies was so little compared to FA-1 suggesting less habitable environment for organisms likely due to strong current actions bringing sediment to the coast. This facies association dominantly occurred in the upper sand unit of well 7119/12-2 and few meters in the lower unit and top part of cored section of well 7119/9-1. Deposition at a near shoreline environment of less shifting energy regime could be suggested.

Figure 5.2: Figure shows core image between 1479-1476 m depth from well 7119/12-2, scale bar 1m (NPD). FA-1 coarser, friable sand, with plane parallel and cross laminated sedimentary structures (F-1.1). Bioturbated, wavy laminations double mud drapes with centimeter scale massive, light colored units (F-1.2).

Figure 5.3: Core image between 1511.39-1514m depth, well 7119/12-2, scale bar is 1m (NPD). FA-1, Facies-1.2 bioturbation-soft sediment burrows (red parenthesis to the right), medium grained sand, some preserved plane parallel lamination (red arrow bottom right) and uni-directional ripple marks (red arrows middle) showing flow direction to the right, small scale sediment load structures (black arrow left). Mostly occurs in the lower sand unit and at the base of upper unit in well 7119/12-2.

Figure 5.4: core image between 1396-1393m, well 7119/12-2, scale bar 1m (NPD). FA-2 dominantly massive with some plane parallel and low angle cross laminations (black arrow), lighter, friable sand, it dominantly occurs in the upper unit of well 7119/12-2 and top part of same unit in well 7119/9-1.

FA-3

Facies association 3 is composed of intercalation of very fine, dark muddy sand and cemented, massive, and lighter color fine sand units (Fig. 5.5). Bioturbation is very strong in this facies association suggesting limited sediment input and hence the environment is suitable for dwelling organisms. Original sedimentary structures have been destroyed by burrowing organisms. The sedimentary sequence of this unit is also characterized by the existence of abundant macrostylolites commonly filled with dark organic matter. This facies association occurs at the base of the upper sand unit of the Stø Formation in well 7119/9-1. Only less than a half meter where bioturbation is rare, lenticular sand at the base of same unit in well 7119/12-2 was observed.

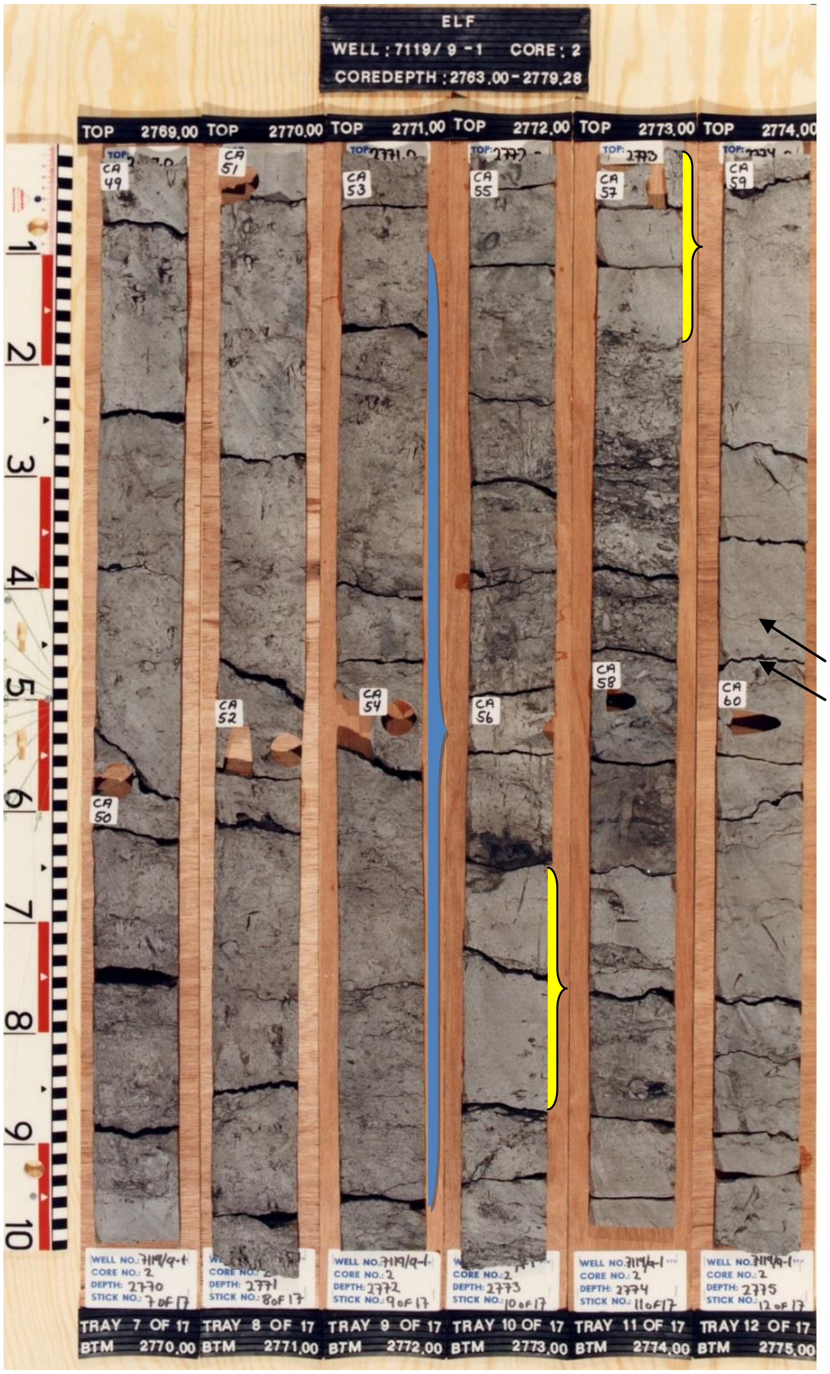

Figure 5.5: Core image between 2774-2769m depth of well 7119/9-1, scale bar is 1m (NPD). FA-3 very fine, muddy sand, strongly bioturbated (blue mark) and intervening massive, clean, and cemented sand units (yellow marks). The sedimentary strata in this depth interval have several macrostylolites (black arrows).

5.2 Petrographic characterization

5.2.1 Point counting during transmitted light microscope:

5.2.1.1 Mineralogical composition: Figure 5.6 shows the conventional thin section point counting results. Most samples contain more than 80% quartz. Accessory mineral grains such as muscovite and other heavy minerals (apatite, rutile, and oxides of iron) constitute only minor amount of the bulk composition (not more than 2% in total). Matrix content varies from sample to sample mostly ranging from 1-4% of the bulk volume with few exceptions reaching up to 12%. Pore-filling booklet type kaolinite mostly associated with muscovite and feldspar was observed. The detrital matrix sediments occur filling pore spaces. Few matrix laminations were also observed. Quartz cement usually constitutes 6-10% of total bulk rock volume in well 7119/9-1and increases as function of depth. It varies between 2-5% in well 7119/12-2 and has variations as a function of depth. Other cements mostly carbonate cement, and pyrite fills up to 4.5% of the bulk rock volume in few samples. These other cement content decreases with depth in opposite to the increase with depth of quartz cement in well 7119/9-1. Secondary porosity due to dissolution of small amount of both feldspar minerals and rock fragments were noted, usually <1%.

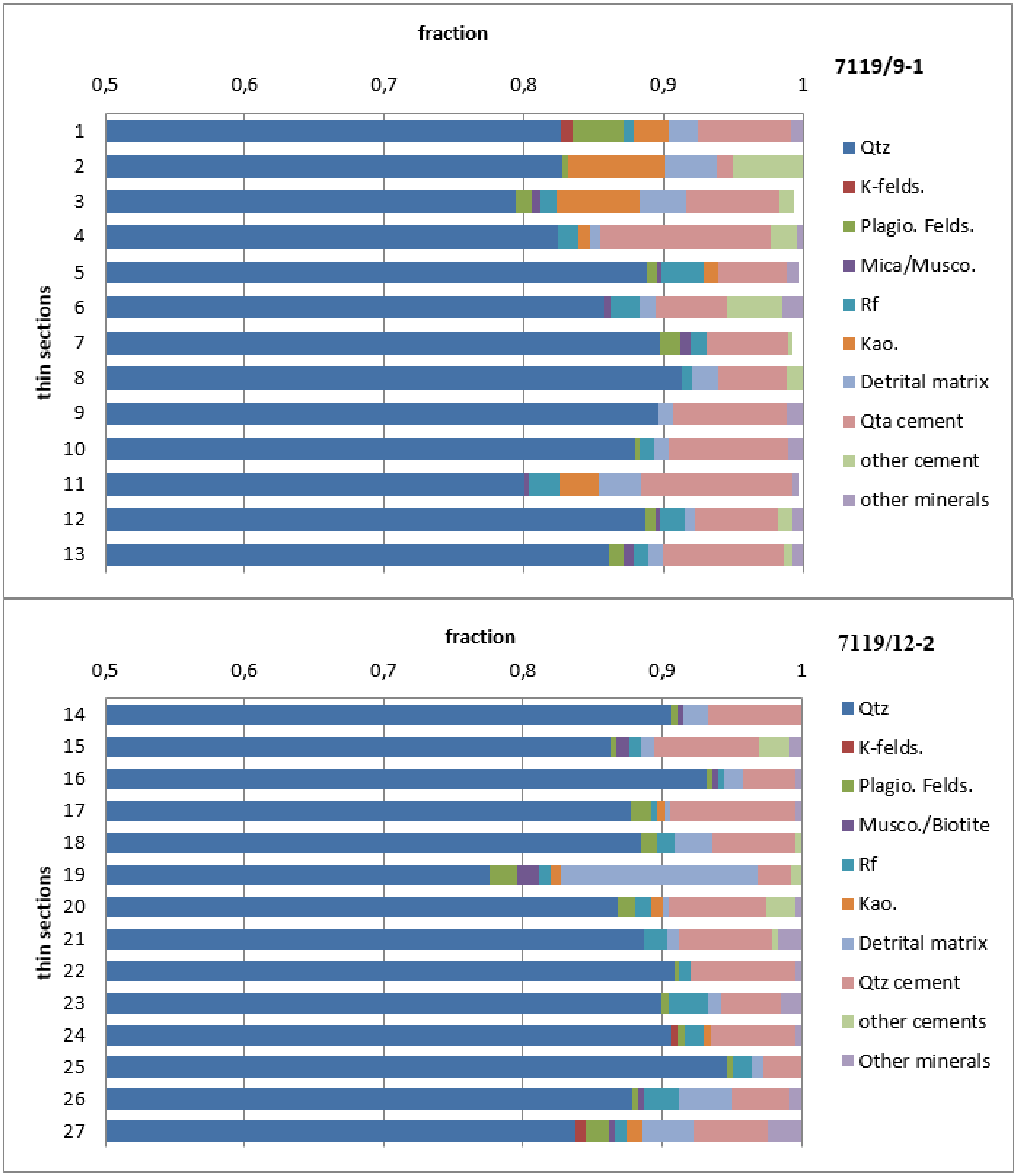

Figure 5.6: Figure displays histogram of petrographic thin section point counted results of sediment mineral composition. Note, for display composition of detrital quartz was cut at 50%

Detrital Framework composition: With regard to detrital frame work composition, detrital quartz grains constitute more than 95% except thin section-1 (Fig. 5.7). Detrital plagioclase dominates over potassium feldspar. The main type of rock fragments are fine sedimentary rocks and chert. The feldspars and rock fragments constitute the remaining percentage of the framework grains. Since the Stø Formation sandstones comprised of detrital quartz grains ≥ 95%, they are quartz arenites (Pettijohn, 1957). The Stø Formation is categorized as mineralogically mature sandstone since it is predominantly composed of high detrital quartz grains.

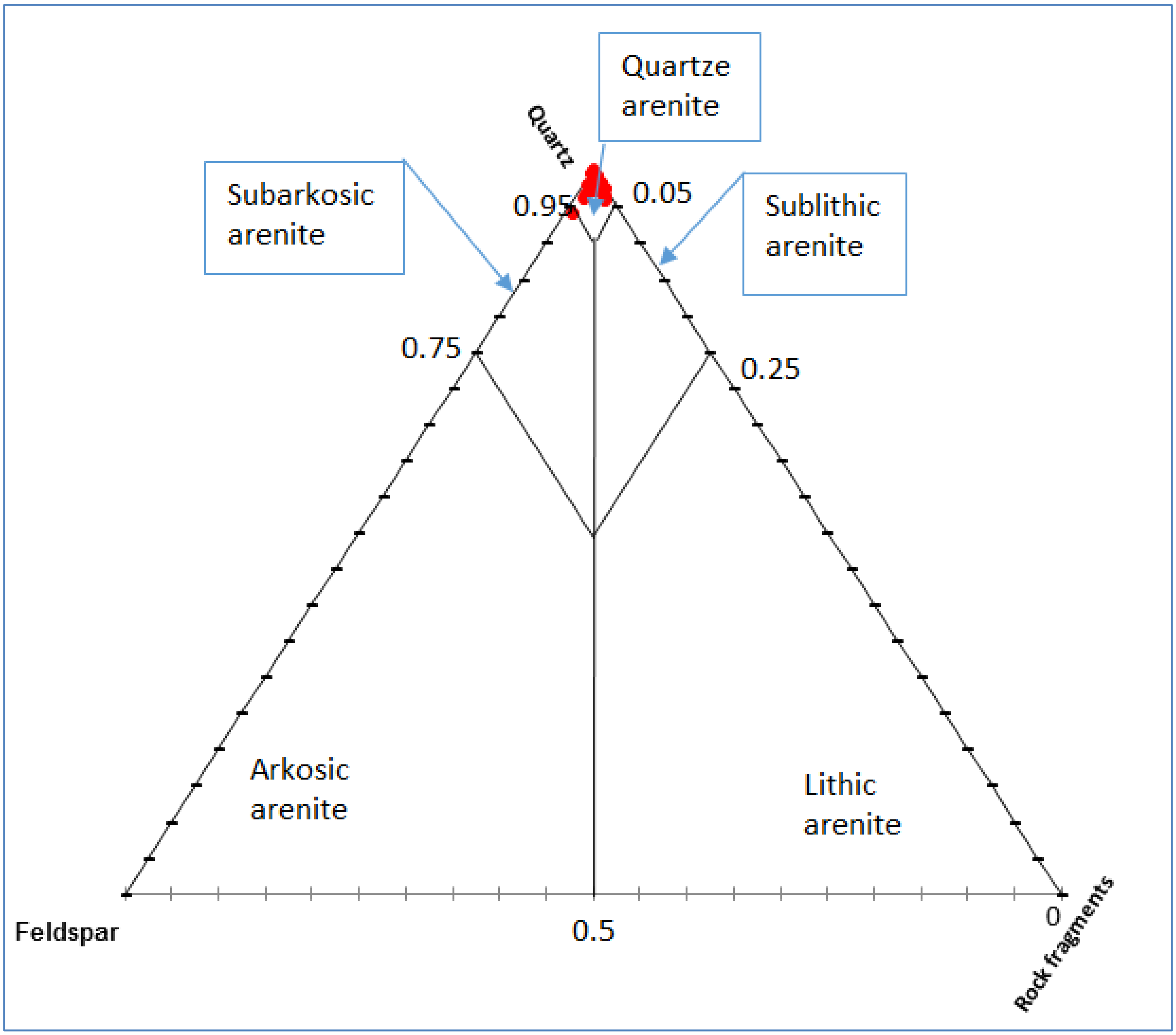

Figure 5.7: Ternary diagram showing framework grains composition of the Stø Formation as obtained from the thin sections petrographic point counts.

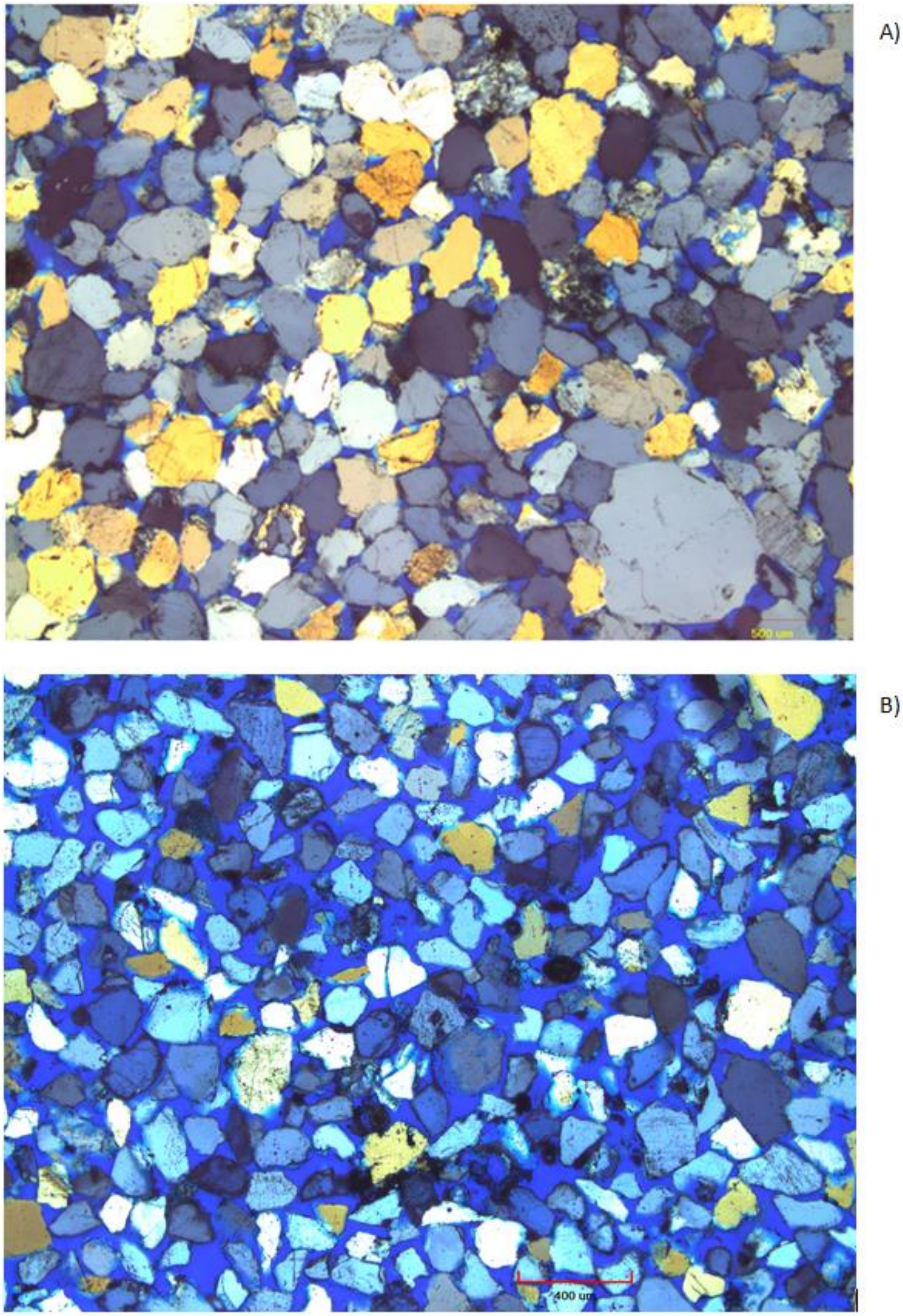

Figure 5.8: Optical micrograph images of representative samples of the Stø Formation: A) from the upper sand unit of well 7119/9-1, thin section-4, where abundant quartz cementation was observed, and B) Image obtained from the lower sand unit of well 7119/12-2, thin section-23, where less quartz cementation was observed.

Bulk XRD analyses: - Bulk mineral composition of powder samples was analyzed using X-ray powder diffraction method. Phase identification was done using DIFFRAC-EVA software and quantified using PROFEX-BGMN bundle based on Rietveld refinement method (Doebelin and Kleeberg, 2015). Similar to the point count analyses results the mineralogy of the Stø Formation is dominated by quartz (Fig. 5.9). More than 90% of the bulk mineral composition is quartz in well 7119/9-1, Even higher percentage (>95%) of quartz in samples from well 7119/12-2. Kaolinite and carbonate content fill the remaining percentage especially in the upper unit of 7119/9-1 and it is in good correlation with point count result. Only few of the samples contain mica/illite clay minerals. In the other heavy minerals category, it includes most importantly pyrite, and minor fraction of apatite, rutile, and zircon. Very little microcline and orthoclase feldspar were included in the other minerals category as well.

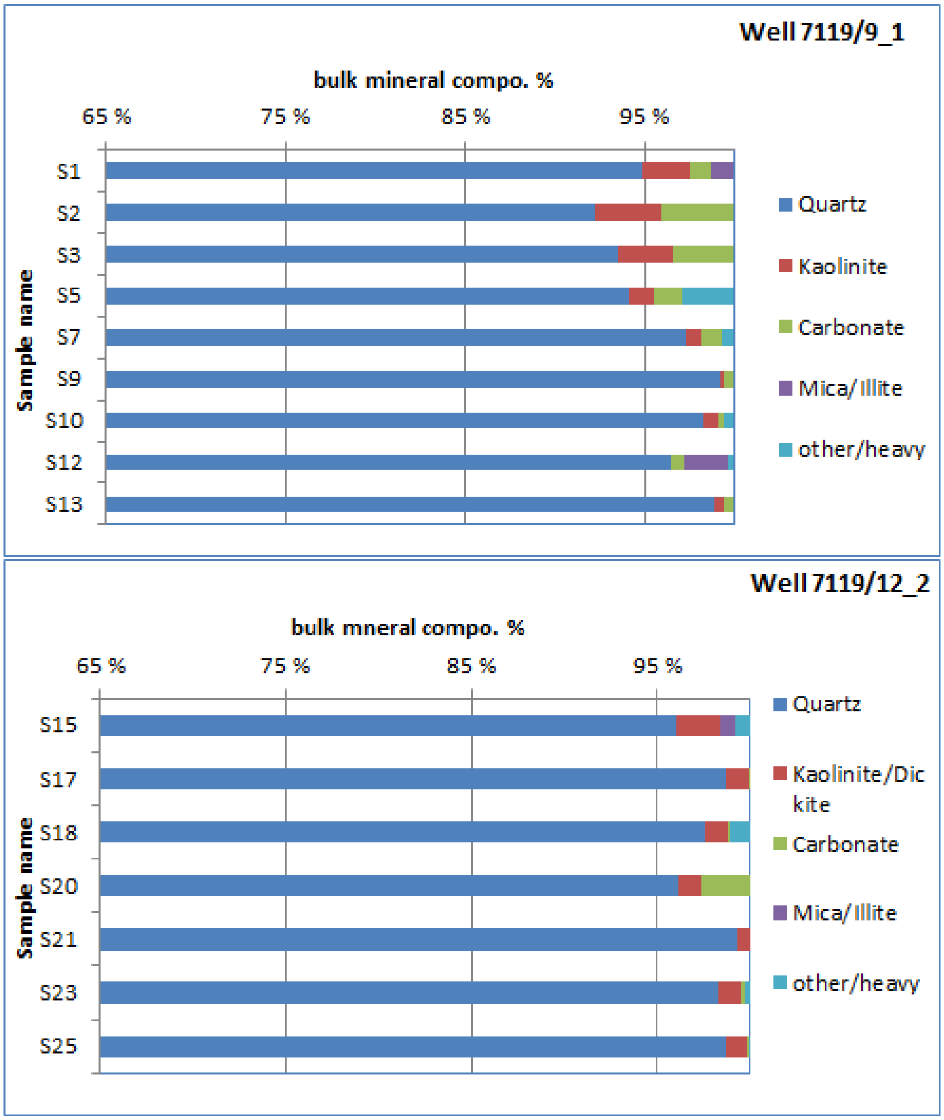

Figure 5.9: X-ray diffraction bulk mineral composition analyses results of powder samples, quantified using PROFEX-BGMN bundle (Rietveld refinement method). It supports the super mature mineralogy of the Stø sandstone units as observed in the point count data.

Porosity evolution as function of quartz cement

Point counted porosity in the upper sand unit of well 7119/9-1predominantly ranges from 5 to 12% but exceptionally high porosity (19%) was noted only in one sample. The porosity values vary as a function of quartz cement; it increases relatively as a function of depth (Fig. 5.10). In this well macrostylolites were noted (Fig. 5.11) and thin sections of high and low quartz cement content were inspected in terms of the distance from stylolites. High amount of quartz overgrowth t was associated with thin sections obtained from near to abundantly stylolitized (wiggly structures) section. Several stylolites were observed in facies association-3 which occurs at the base of upper sand unit, well 7119/9-1. Macrostylolites filled with dark, organic material was especially concentrated at the interfaces between small units of massive, clean, relatively coarser sand units with bioturbated, dirty, very fine intervals. Figure 5.12 shows cross polarized microscope image from thin section-14 where in the presence of mica grains dissolution of detrital quartz grains were noted. This may suggest development of macrostylolites at interfaces of muddy and clean sand units in FA-3 facilitated by clay induced grain dissolution. Grain coating of detrital quartz grains by illite clay minerals were observed in thin sections of high porosity content in this well as depicted in the SEM analyses (Fig. 5.26). Porosity variation was observed in well 7119/12-2 however it does not have observable relationship with quartz cementation (Fig. 5.10).

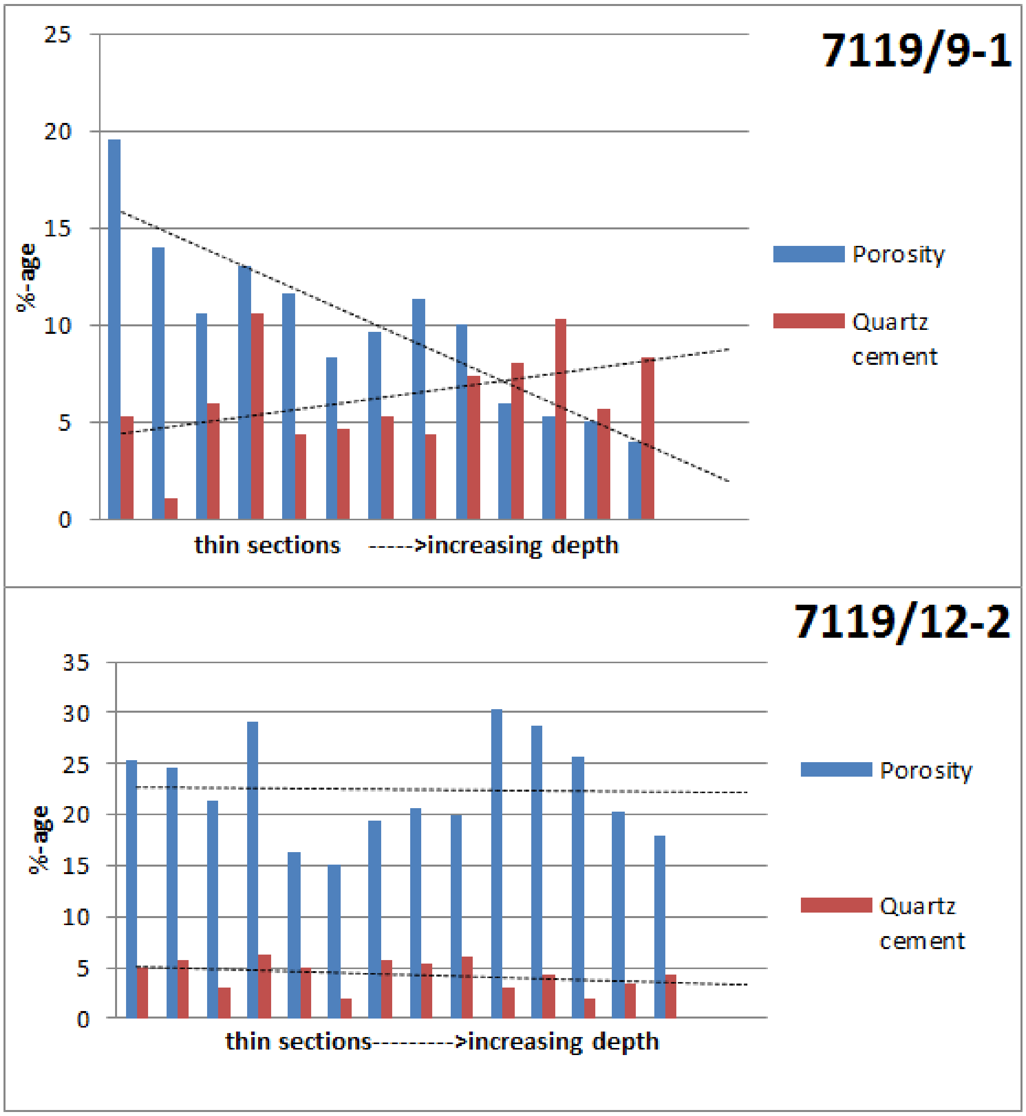

Figure 5.10: Histogram of point count porosity and quartz cement for individual thin sections, porosity varies as a function of degree of quartz cement in well 7119/9-1, whereas it has no observable trend with quartz cement in well 7119/12-2**.**

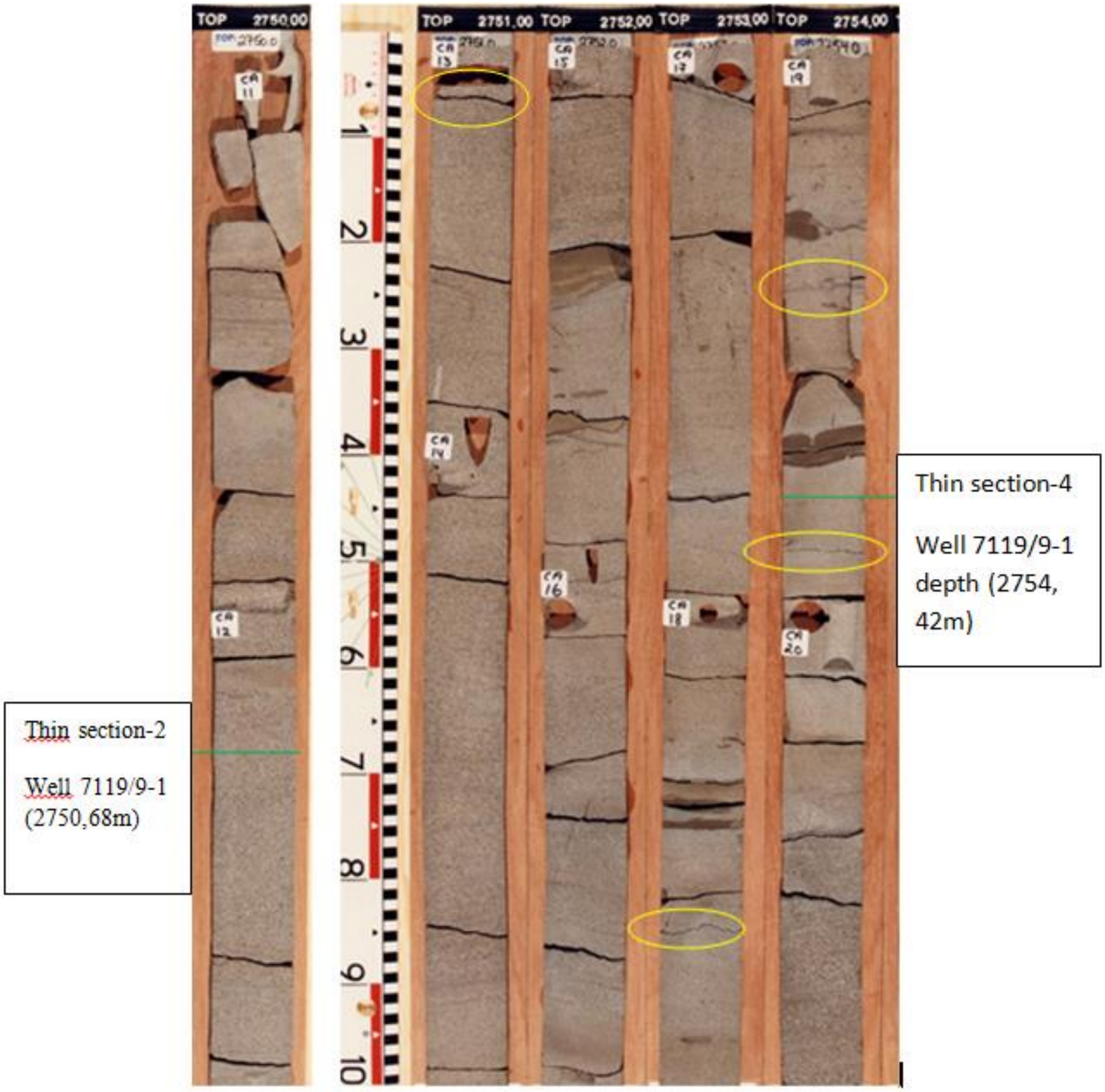

Figure 5.11: Thin sections locations relative to well-developed stylolites (yellow marks) in the core section obtained from the upper sand unit of Stø Formation in well 7119/9-1. Thin section-4 lies few centimeters far from the closest stylolite and have high counted quartz cement, thin section-2 lies meter scale far from stylolite and contains low quartz cement. Core image taken from (NPD, 2017)

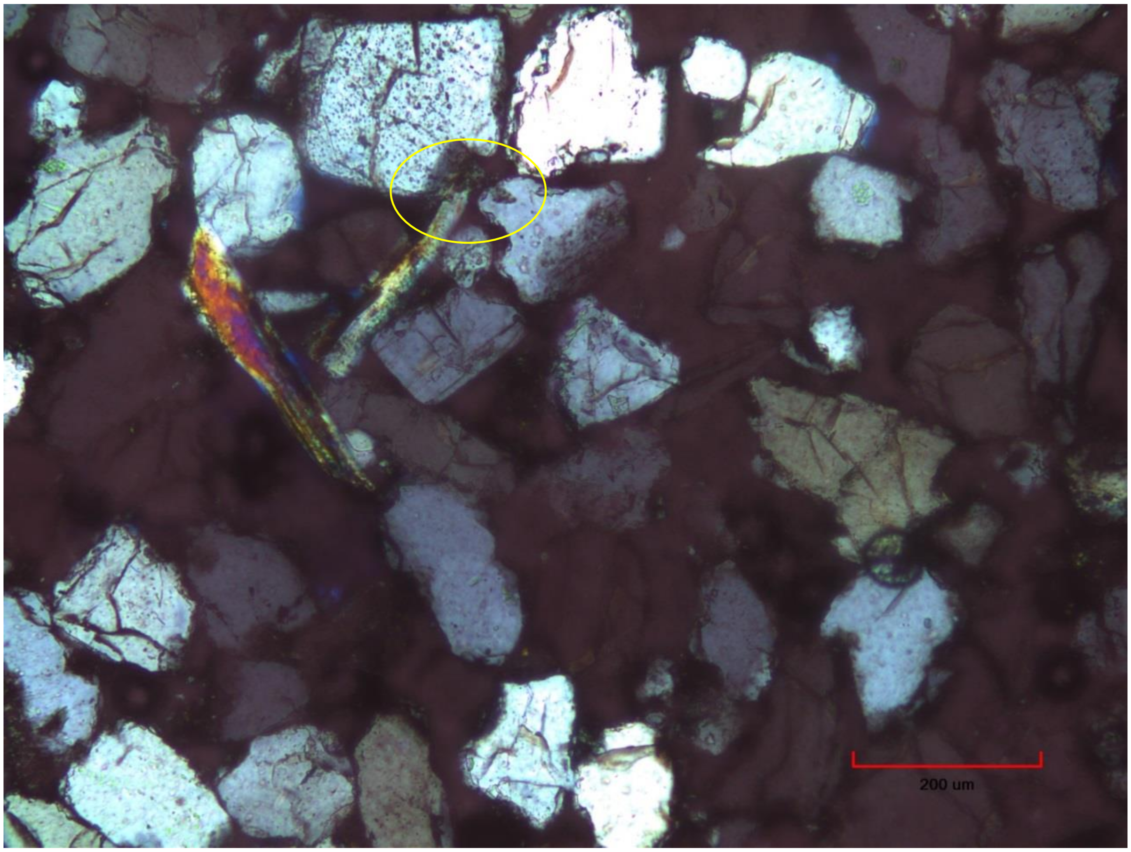

Figure 5.12: cross-polarized optical micrograph from thin section-14, well 7119/12-2. It shows an interaction between muscovite and quartz grains at the interfaces.

Porosity is little affected by both detrital and authigenic matrix minerals and other carbonate cement in general in the Stø Formation of both wells. However, slight decreasing trend observed with increasing detrital matrix content in the upper sand unit of well 7119/12-2 (Fig. 5.13). Exceptionally high matrix content from thin section-19, which is obtained from bottom part of the upper unit, near to the intervening shaly unit, is associated with laminated matrix occurrence. It creates clear boundary between the two sand units. Figures 5.14 A and B shows laminated and infiltrated pore filling form of detrital matrix from thin sections-27 and 15 of well 7119/12-2 respectively. Other authigenic minerals of most importantly kaolinite, carbonate cements, pyrite, and some opaque (iron oxide) minerals were observed to fill pore spaces in some thin sections during the optical microscopy but generally limited contribution. Figure 5.15 displays pore-filling authigenic carbonate cement, and pyrite.

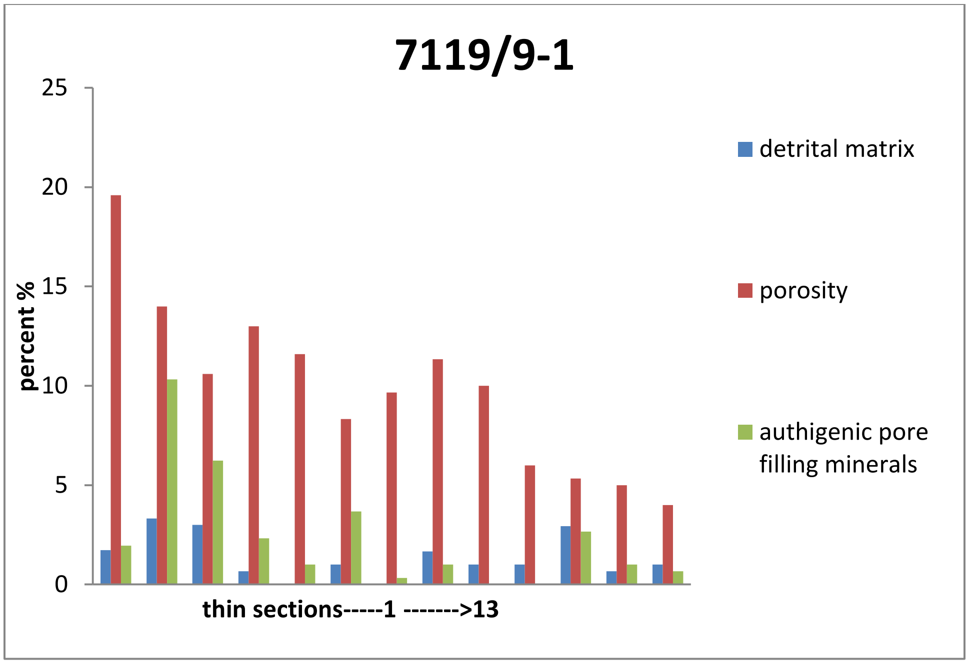

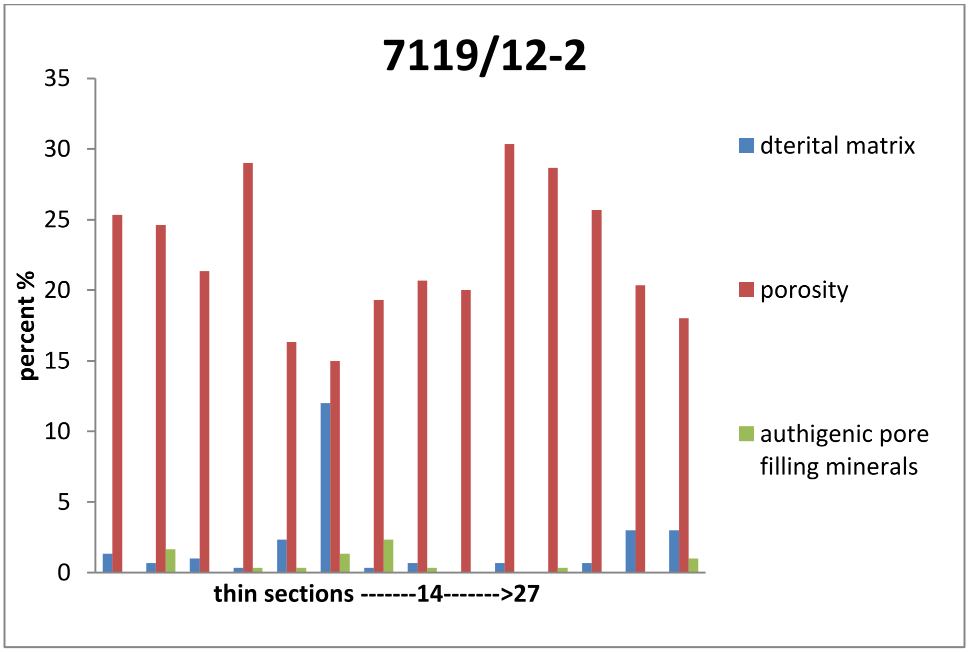

Figure 5.13: Histogram displays point counted fractions of detrital matrix and total amount of authigenic clay and carbonate cement of each thin section from both wells.

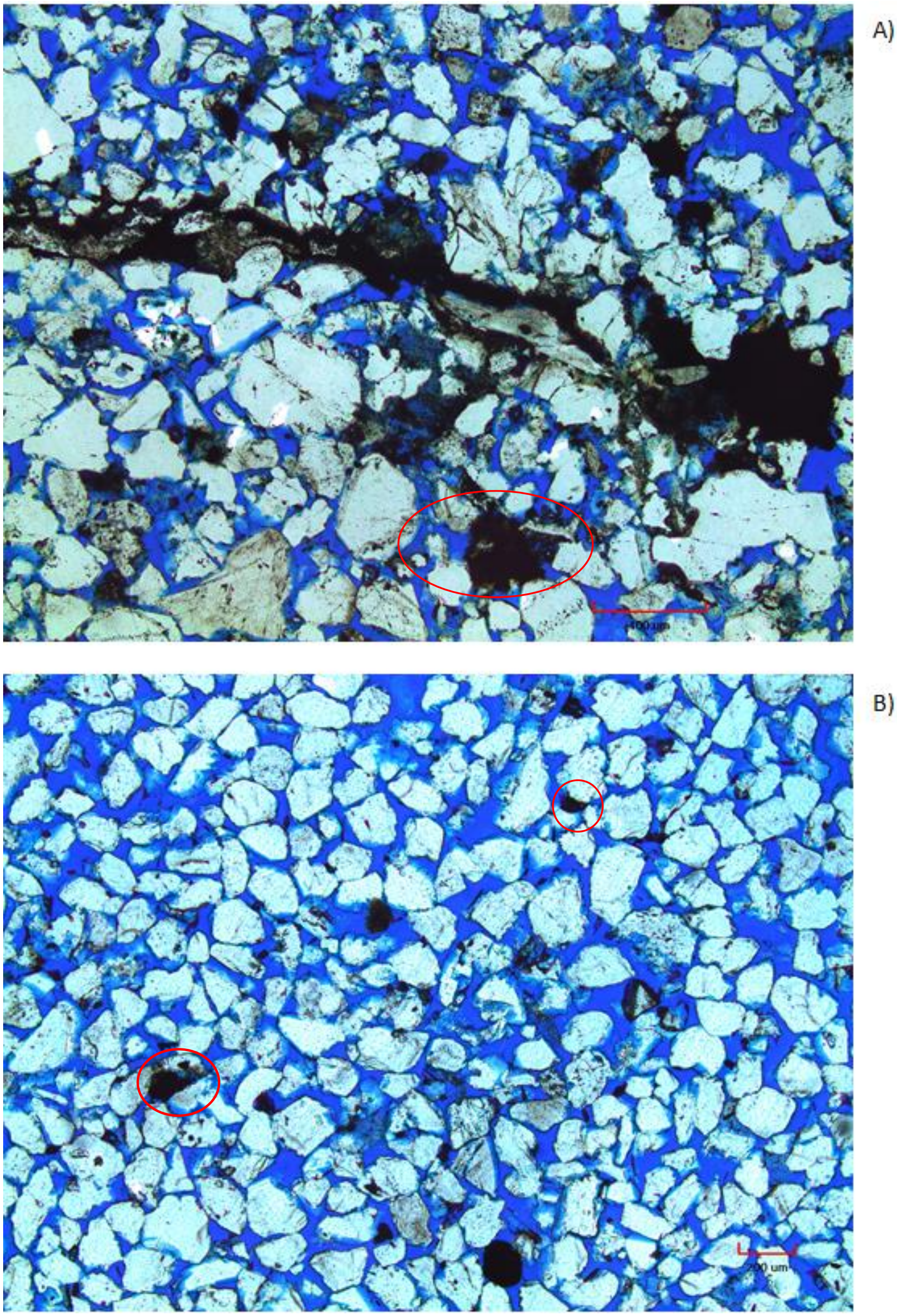

Figure 5.14: thin section micrographs of plane polarized microscope displays high porosity Stø Formation from well 7119/12-2. A) Thin section-27 is from the lower sand unit of well 7119/12-2, B) thin section-15 is from the upper sand unit of the same well. It shows detrital matrix of laminated and pore filling (red marks) form.

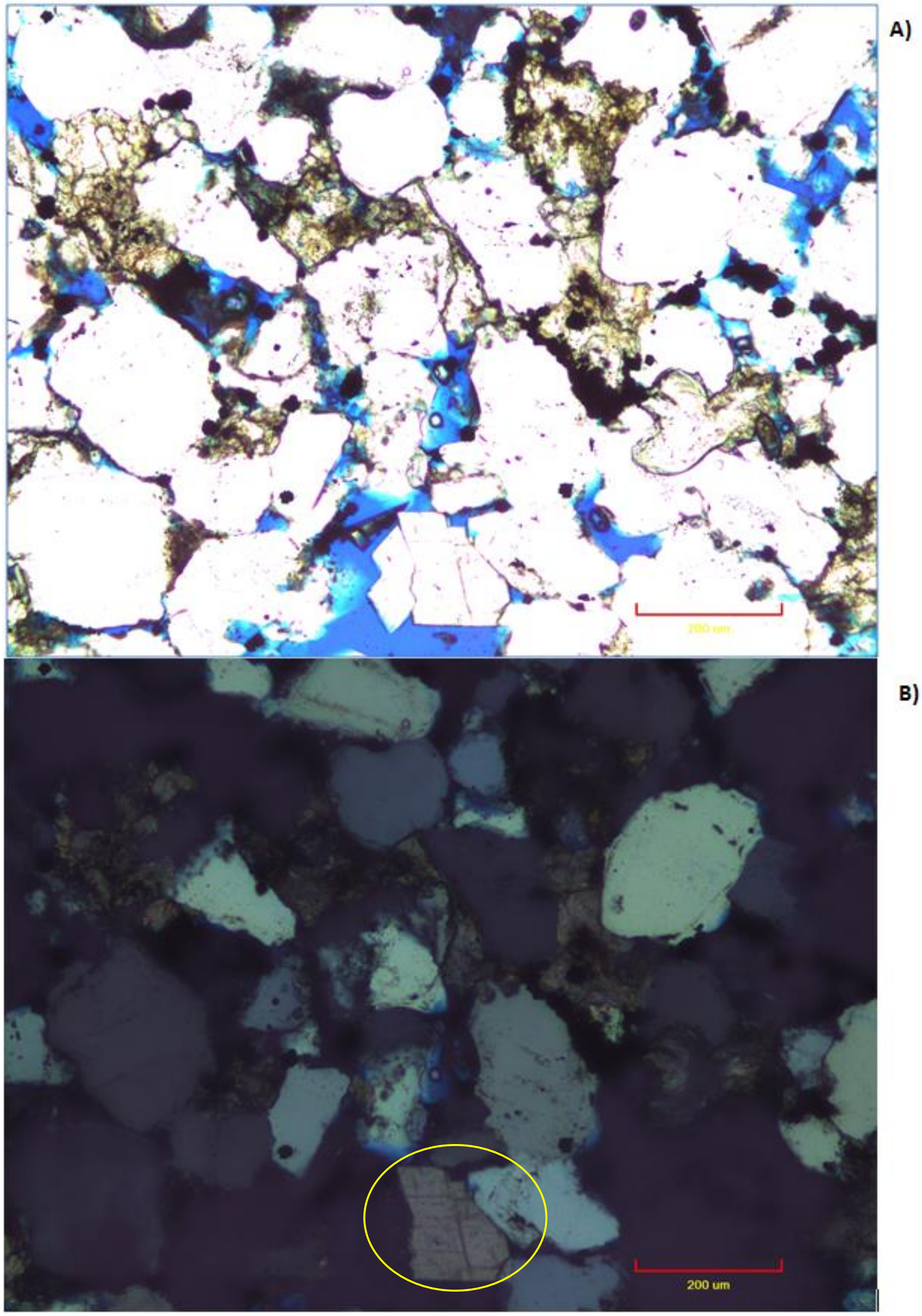

Figure 5.15: Figure displays optical micrograph images, A) is plane polarized image from thin section-6 of the upper sand unit, well 7119/9-1m, showing deformed carbonate cement (yellowish color), and pyrite (dark spots), B) is cross polarized image of A, where undeformed carbonate cement grows into pore spaces (yellow mark).

5.2.1.2 Intergranular volume (IGV)

Total sum of intergranular porosity (Primary porosity), detrital matrix, authigenic clay and carbonate cement, and other pore filling materials was calculated for individual thin sections and plotted against depth (Fig. 5.16A). An average IGV of 29% at average depth of 1400m, and 19% at average depth of 2700m in wells 7119/12-2 and 7119/9-1 measured respectively. After depth, correction using an average of 600m for both wells the measured IGV's would lay at an average depth of 2000m and 3300m. Low IGV measurements below 20% observed in well 7119/9-1 though the Stø sand observed to have little soft sediment grains that reduce IGV values at relatively lower effective stress. In addition, brittle deformation of rigid sand grains (quartz) was not much observed as depicted in the SEM analyses section. Figure 5.17 shows cross-plot between point-counted quartz cement and measured IGV for individual thin sections. Accurate counting of quartz cement was difficult using optical microscope especially in the abundantly quartz cemented thin sections due to lack of well-defined dust rims. This could associate with the low IGV measurements observed.

Figures 5.18 A, and B show cross plot between measured IGV and average grain sizes and calculated sorting respectively. IGV values observed to decrease with decreasing grain sizes while it has no observable trend with sorting in well 7119/9-1. In contrary to this, systematic variation of IGV with grain size and sorting exist in well 7119/12-2. An increasing trend of IGV values with decreasing grain size can be noticed, and decreases with deteriorating sorting in both sand units of later well.

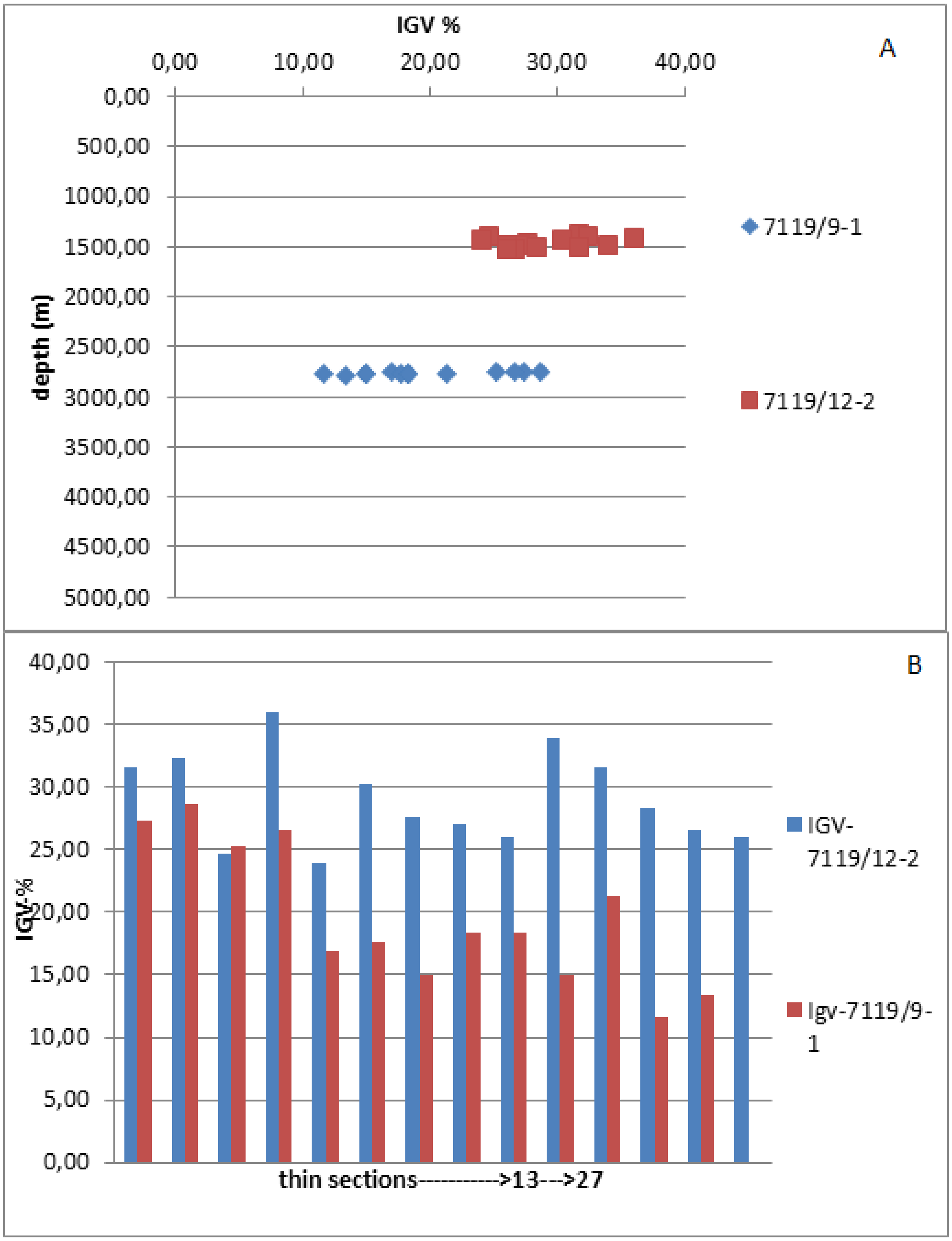

Figure 5.16: Figure displays measured IGV versus depth plot of individual thin sections from both wells (A), and histogram of measured IGV for individual thin sections (B). More scattered with an average value of 19% IGV was measured from thin sections of well 7119/9-1 while less scattered with an average of 29% in well 7112/12-2.

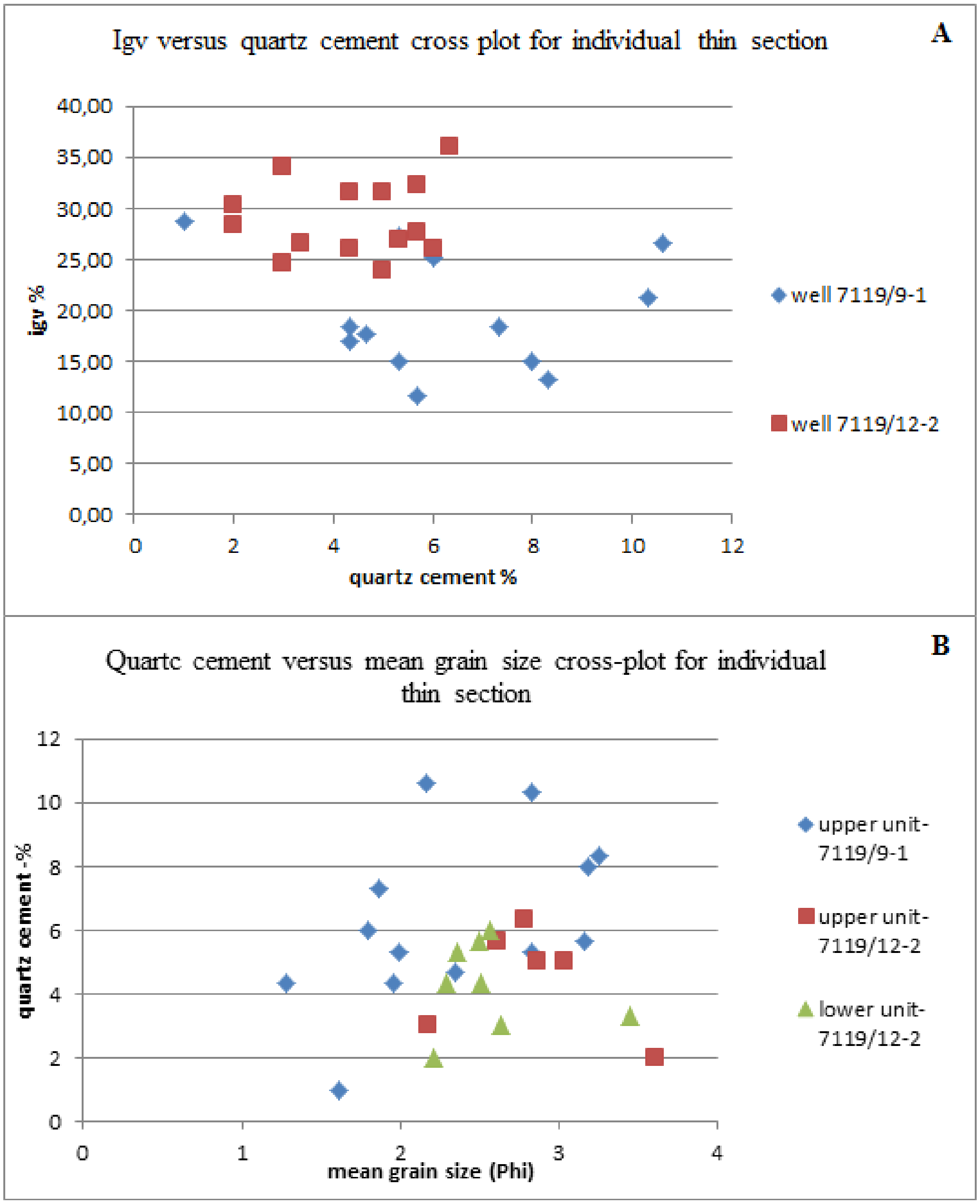

Figure 5.17: Figure displays cross-plot between point-counted quartz cement and measured IGV's for individual thin section of both wells (A), and cross-plot between quartz cement and mean grain size (B).

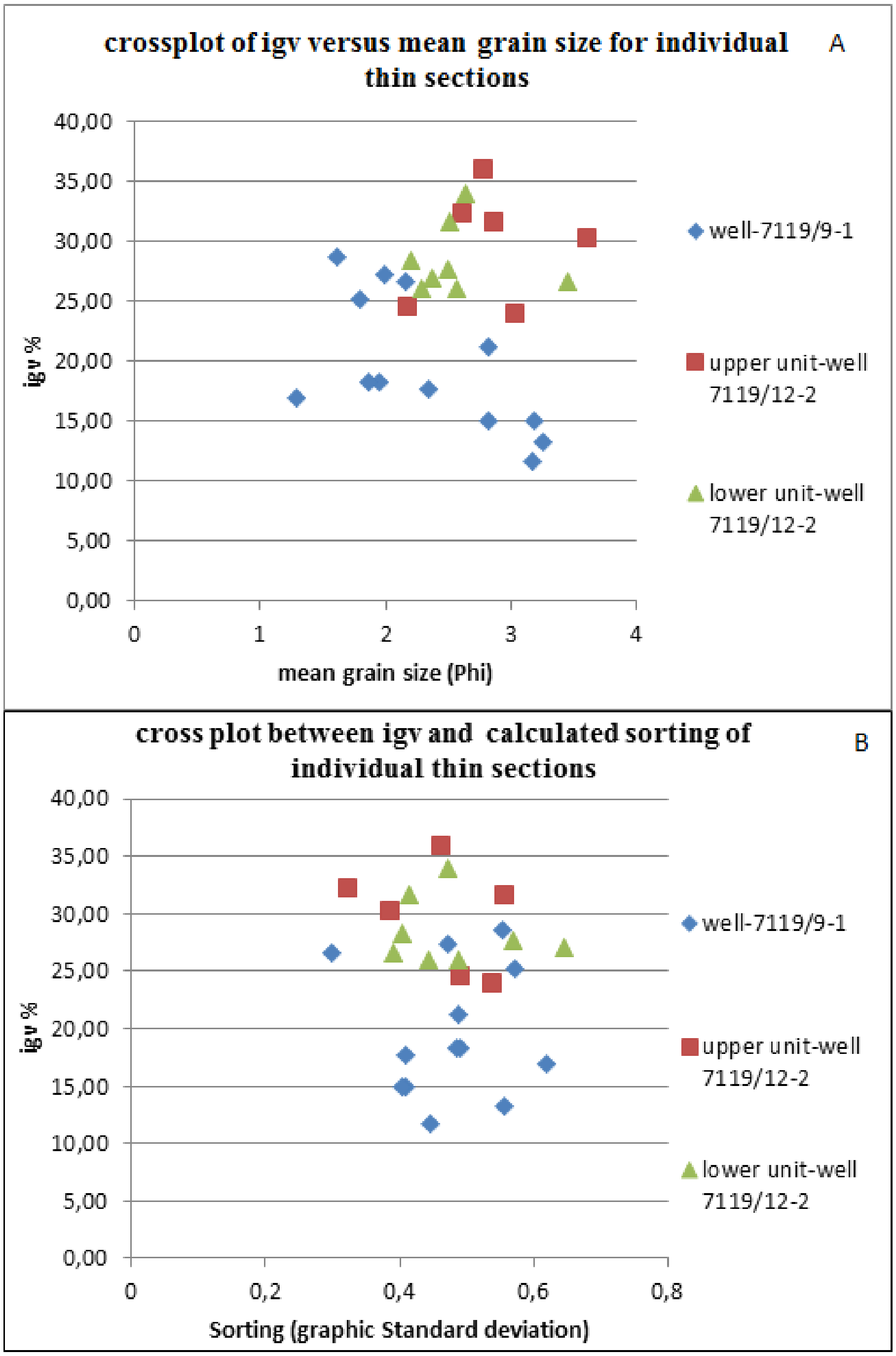

Figure 5.18: Figures display cross-plot between measured IGV with average grain size and calculated sorting for individual thin section of both wells. A) Shows IGV decreases with decreasing average grain size in well 7119/9-1 whereas it increases in well 7119/12-2. B) IGV has no observable trend with calculated sorting in well 7119/9-1 while it decreases with deteriorating sorting in well 7119/12-2.

5.2.1.3 Texture

(Grain size): - grain size measurements performed along the long axis of grains of 100-randomly selected points using an optical microscope and transformed into phi scale. Mean grain size was calculated using an arithmetic average for individual thin sections of both wells and plotted against depth (Fig. 5.19 A, B). Generally, grain size increases, from very fine sand at the base to medium sand to the top in the upper sand unit of well 7119/9-1. Similarly, slight increase in grain size up depth in the same unit of well 7119/12-2 observed, while the lower sand unit contains average of fine-grained sand and shows no observable change with depth.

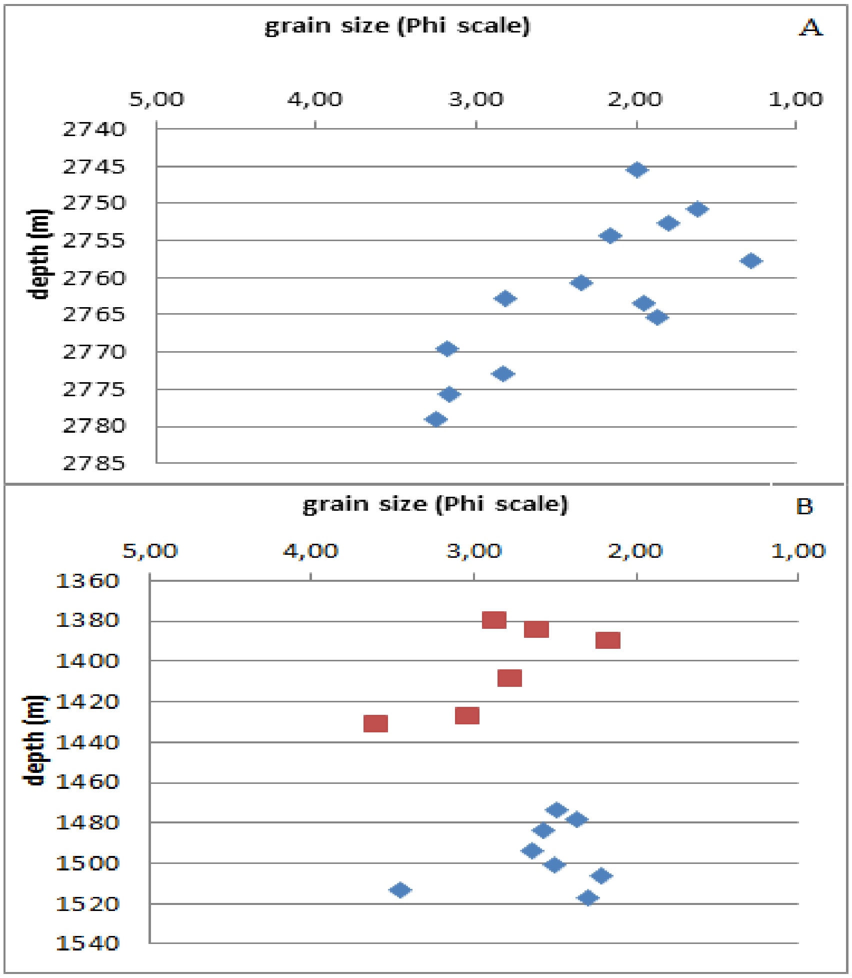

Figure 5.19: Figures display plot of mean grain size (arithmetic average) against depth for individual thin sections of both wells. A) Well 7119/9-1 grain size decreases with increasing depth, B) well 7119/12-2 generally decreasing trend of grain size in the upper sand unit, while almost constant in the lower unit

Texture (Sorting): The distribution of measured grain size values were analyzed using cumulative frequency curves that can describe degree of scatter from specific value. Grain size measurements were plotted in cumulative frequency distribution curves (Fig. 5.20, 5.21) below for individual thin section samples. Mostly steeper curves observed in thin sections of the lower sand unit of well 7119/12-2 (Fig. 5.21B). Such curve shape is characteristic of well-sorted sand (Bjørlykke, 2015). Figures 5.20 and 5.21A show relatively less steep curves an indication of relatively less sorted sand of the upper sand unit.

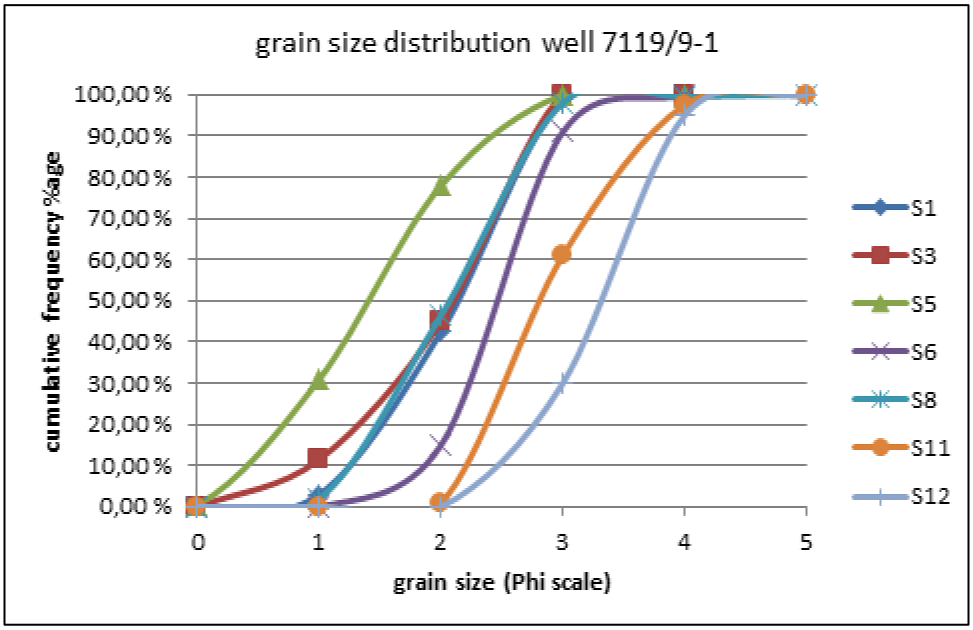

Figure 5.20: Figure displays grain size cumulative distribution curves of some representative samples from well 7119/9-1 based on thin sections inspection.

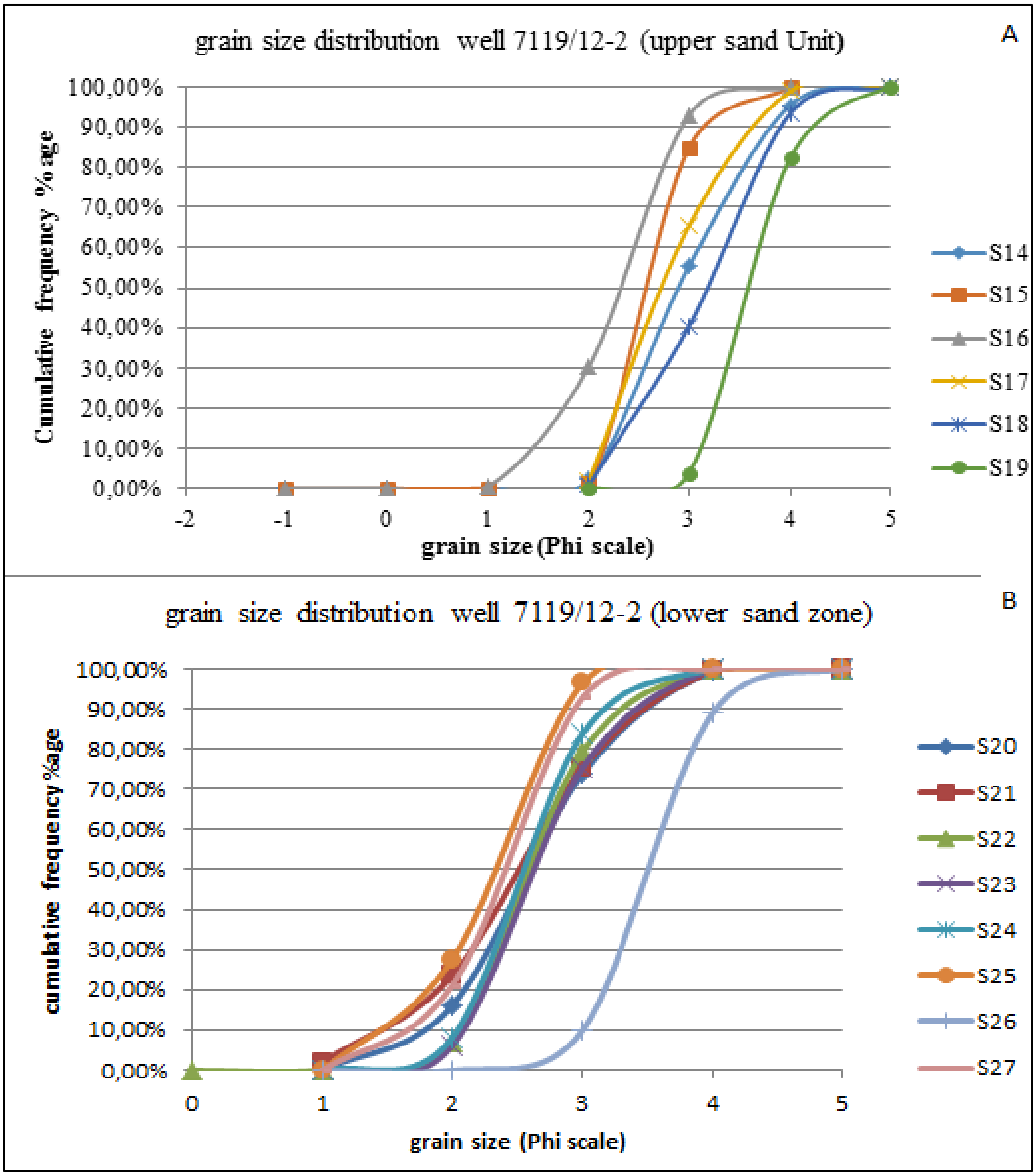

Figure 5.21: Grain size cumulative distribution curve of representative samples from well 7119/12-2 based on thin sections measurement relatively steeper curves in figure B) than in A).

From the statistical calculations, inclusive graphic standard deviation (sorting) shows most of the samples from both wells lie in the well-sorted interval (Table 5.2). However, few samples fall in the moderately sorted and very well sorted sand category. Calculated skewness from same table, almost all thin sections from the lower sand unit of well 7119/12-2 have a near symmetrical skewness. From the upper sand unit most samples show near symmetrical and significant samples laid in the fine skewed interval. Relatively variable skewness observed from thin sections of well 7119/9-1, mostly near symmetrical, and some fine to very coarse skewed range.

Table 5.2: Summary of statistical analyses results of measured grain sizes; calculated inclusive standard deviation (sorting), left, and inclusive graphic skewness, right

Calculated sorting	7119/9-1 upper unit	7119/12-2 upper unit	7119/12-2 lower unit
v.well-sorted	1	1	-
Well-sorted	8	3	6
Moderately-sortied	4	2	2
Poorly-sorted	-	-	-

Calculated skewness	7119/9-1 upper unit	7119/12-2 upper	7119/12-2 lower
Strongly c. skewed	2	-	-
C. skewed	1	-	1
Near symm.	6	3	7
fine skewed	4	3	-
strongly f. skewed	-	-	-

Texture-Grain shape: - Based on observation of 100 points per thin section, roundness/angularity of detrital framework grains were determined using optical microscope. The sediments of the Stø Formation from both wells display predominantly of sub-angular and sub-rounded grains but significant angular and some rounded grains were also noted (Fig. 5.22). Likewise, all representative samples from both well display predominantly (more than 65% of the grains) non-spherical grains but some spherical grains were also noted (Fig. 5.23).

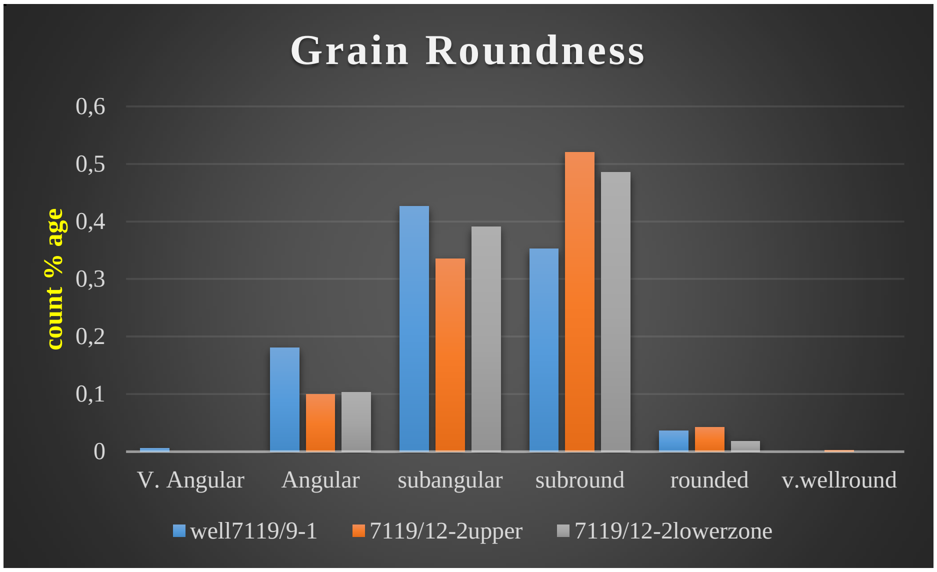

Figure 5.22: grain roundness based on observations of 100 points per thin section, of the three sand units.

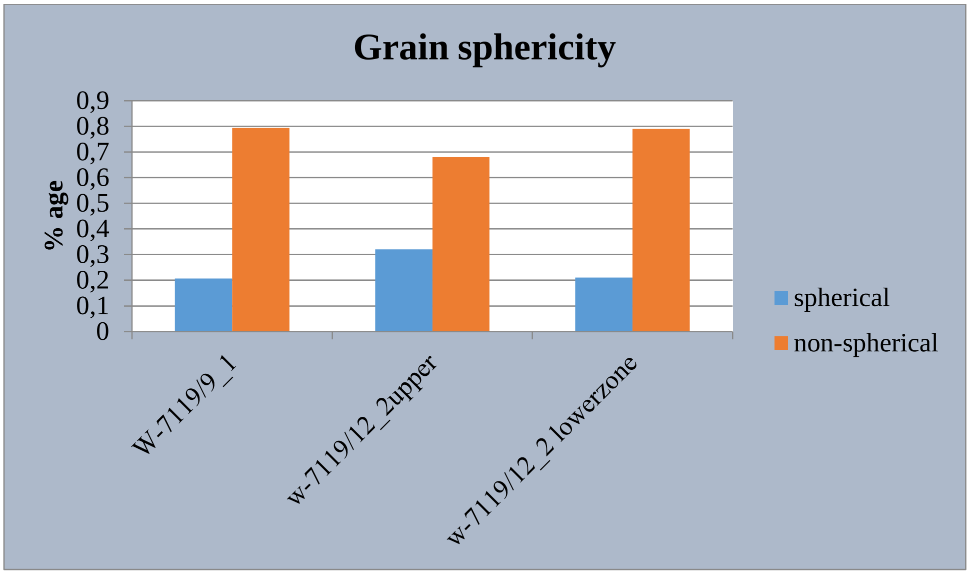

Figure 5.23: grain sphericity observations of thin sections. Mostly containing more than 65% non-spherical grains

Grain fabric: - grain-to-grain contact observation of some thin sections studied to establish the grain fabric, and indices of five descriptive terms (floating, point contact, long, concavo-convex, and sutured contacts) quantified as displayed in (Fig. 5.24). It was difficult to recognize type of grain contact in the abundantly quartz cemented thin section samples using optical microscope, so preferentially samples of less quartz cement content were counted. Long -contact observed to dominate in thin sections of well 7119/9-1, whereas dominantly of point contact from thin sections of well 7119/12-2. Quartz cement precipitating at grain contact might have contributed to recognize apparent long contact between sediment grains that is difficult to distinguish the true contact using optical microscope. Some fraction of concave-convex contact observed as well.

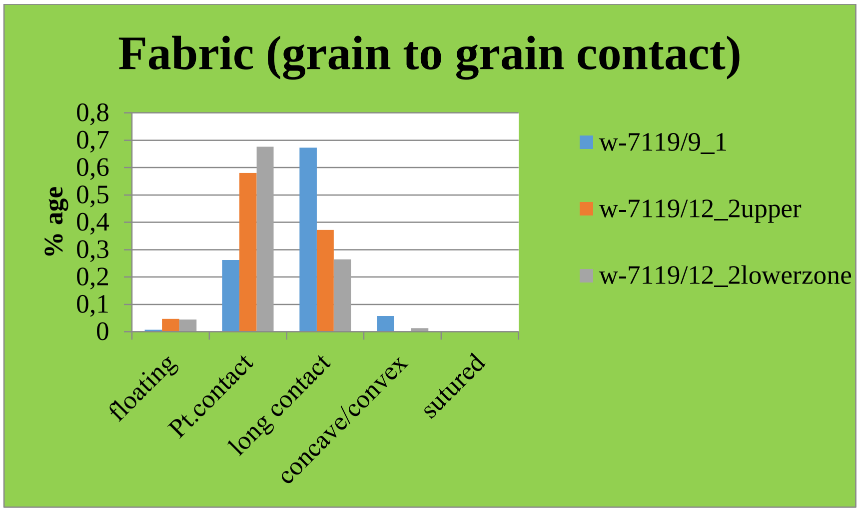

Figure 5.24: Figure displays statistics of quantitative indices of descriptive terms of grain contact relationship

5.2.2 Scanning Electron Microscopy (SEM) and Cathodoluminescence (CL)

Observation of thin sections using petrographic SEM and CL confirmed extensive quartz-overgrowth cement occurrences especially in the lower part of upper sand unit (FA-3) in well 7119/9-1, while less quartz cement in well 7119/12-2. Figure 5.25A and B below is CL and combined CL-Secondary Electron micrograph respectively from thin section-5 that shows thick quartz overgrowth. Figure 5.25C is combined CL-Secondary Electron micrograph from thin section-15 and shows newly growing quartz create rough surfaces on detrital quartz grains. Quartz cement counting using transmitted light microscope was based on observation of well-defined dust rims and well developed euhedral growth on detrital quartz grains. There is uncertainty that quartz cement could have been underestimated due to lack of such parameters.

An exceptionally higher porosity was observed in few thin sections especially from the top part of the upper sand unit in well 7119/9-1 unlike abundant quartz cementation in most thin section samples. An X-ray elemental mapping was done in some thin sections including from well 7119/12-2 if porosity preserving grain coating minerals exist. Figure 5.26A shows BSE image taken from thin section-2 where porosity constitutes 14% of the bulk volume, and its X-ray elemental mapping image (Fig. 5.26B). Thin illitic grain coatings partially to fully covering surfaces of detrital quartz grains can be noted. Similarly, BSE image from thin section-11 of same well (Fig. 5.27) show partial covering of detrital quartz grain by filamentous illite and limit authigenic quartz cement to grow.

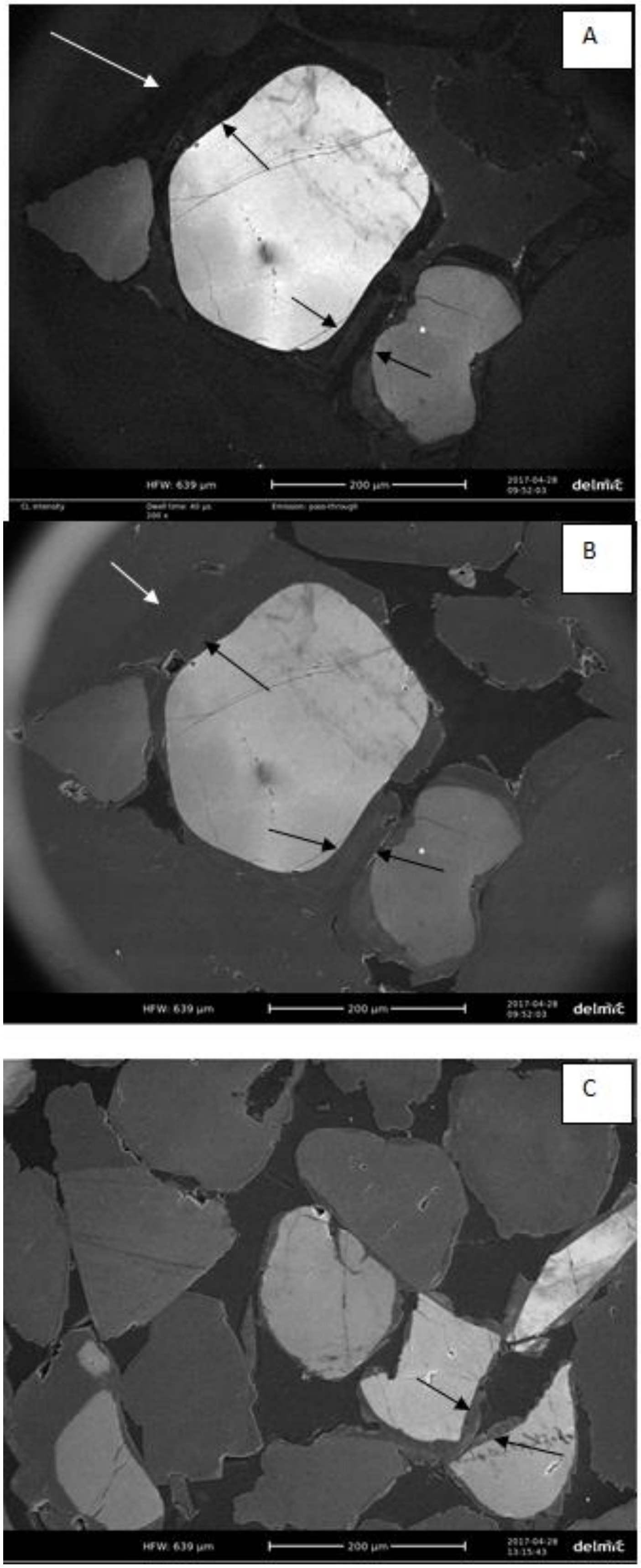

Figure 5.25: A) Is CL micrograph from thin section-5 of well 7119/9-1 where arrows indicate the boundary between authigenic and detrital quartz (authigenic quartz being very dark), B) Combined CL and Secondary Electron micrograph of (A). C) Is combined CL-Secondary Electron micrograph from thin section-15 of well 7119/12-2 shows authigenic quartz is not important to reduce porosity. Scale bar is 200um

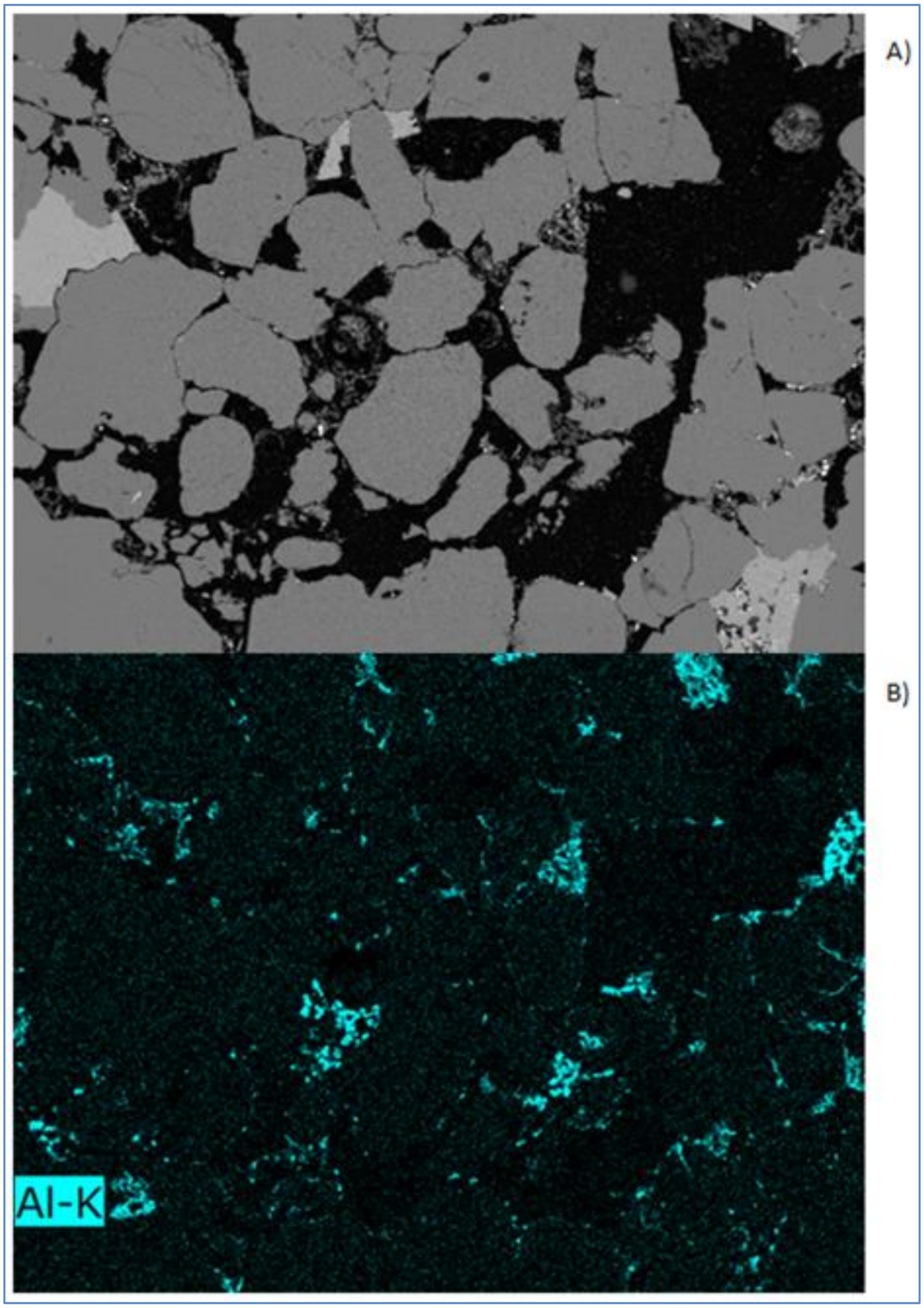

Figure 5.26: A) SEM backscattered micrograph from thin section-2, from the upper sand unit of well 7119/9-1, B) X-ray elemental mapping of micrograph shown in (A). Very thin illitic type grain coating is noticed on some detrital quartz grains (note the middle right corner of the micrograph).

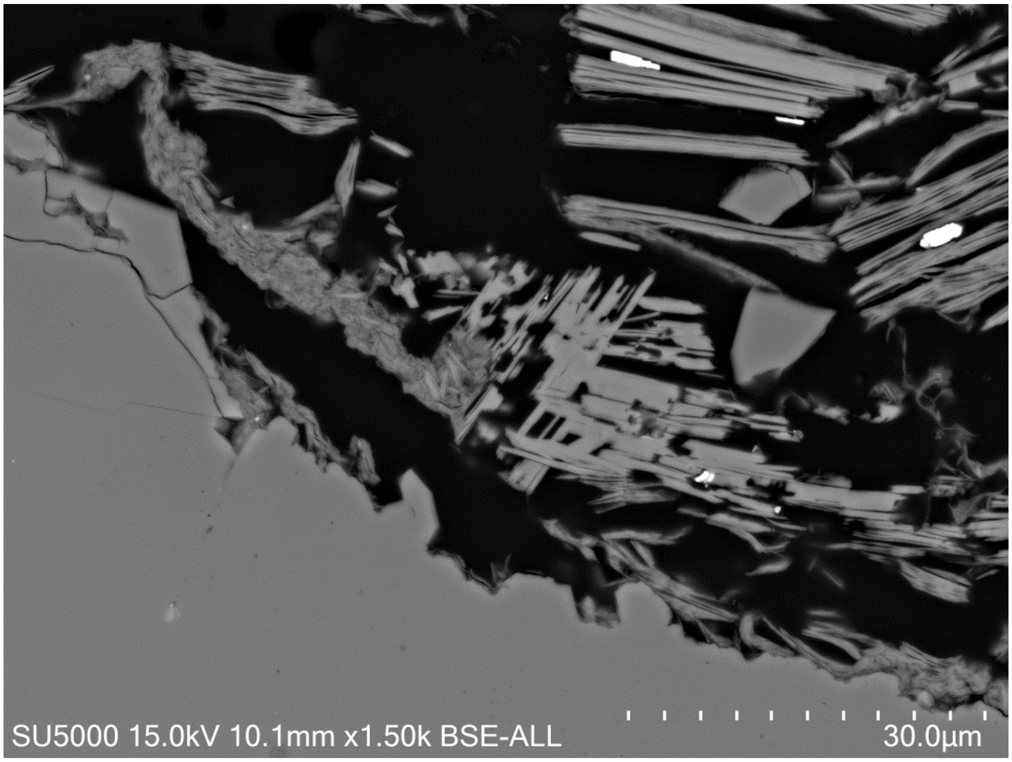

Figure 5.27: SEM BSE image from thin section-11 of well 7119/9-1. It shows thin, non-continuous illitic clay coats at the surface of detrital quartz grain. The non-coated part displays quartz overgrowth that is protruding into the pore-space and hence the illitic clay coat may have limited the growth of authigenic quartz.

During the SEM study, matrix composition and its occurrences between sand grains were analyzed as well. Authigenic kaolinite observed associated with dissolving muscovite (Fig. 5.28 A, B). It was commonly observed dispersed in pore-spaces. Vermicular form of kaolinite is also observed in some thin sections most commonly in the upper sand unit of well 7119/12-2. Detrital matrix of mostly illitic composition was observed in a pore filling form and few laminated form. Other accessory minerals of the framework grain such as solid feldspar that is difficult to discriminate with quartz using optical microscopy were observed. In addition, other minor mineral grain constituents and nature of some early cementing materials were studied. Compositionally ankerite was the most commonly observed carbonate cement appeared to occlude pore spaces (Fig. 5.29C), and some calcite, siderite, and dolomite. Pyrite commonly scattered with detrital matrix, framboidal pyrite filling intergranular pore spaces and intragranular fractures. Little iron oxide cement was also observed. Heavy minerals such as apatite, zircon, chlorite, and rutile were recognized (Fig. 5.29A). Figure 5.29B from thin section-15 shows combined needle like rutile minerals cemented by quartz.

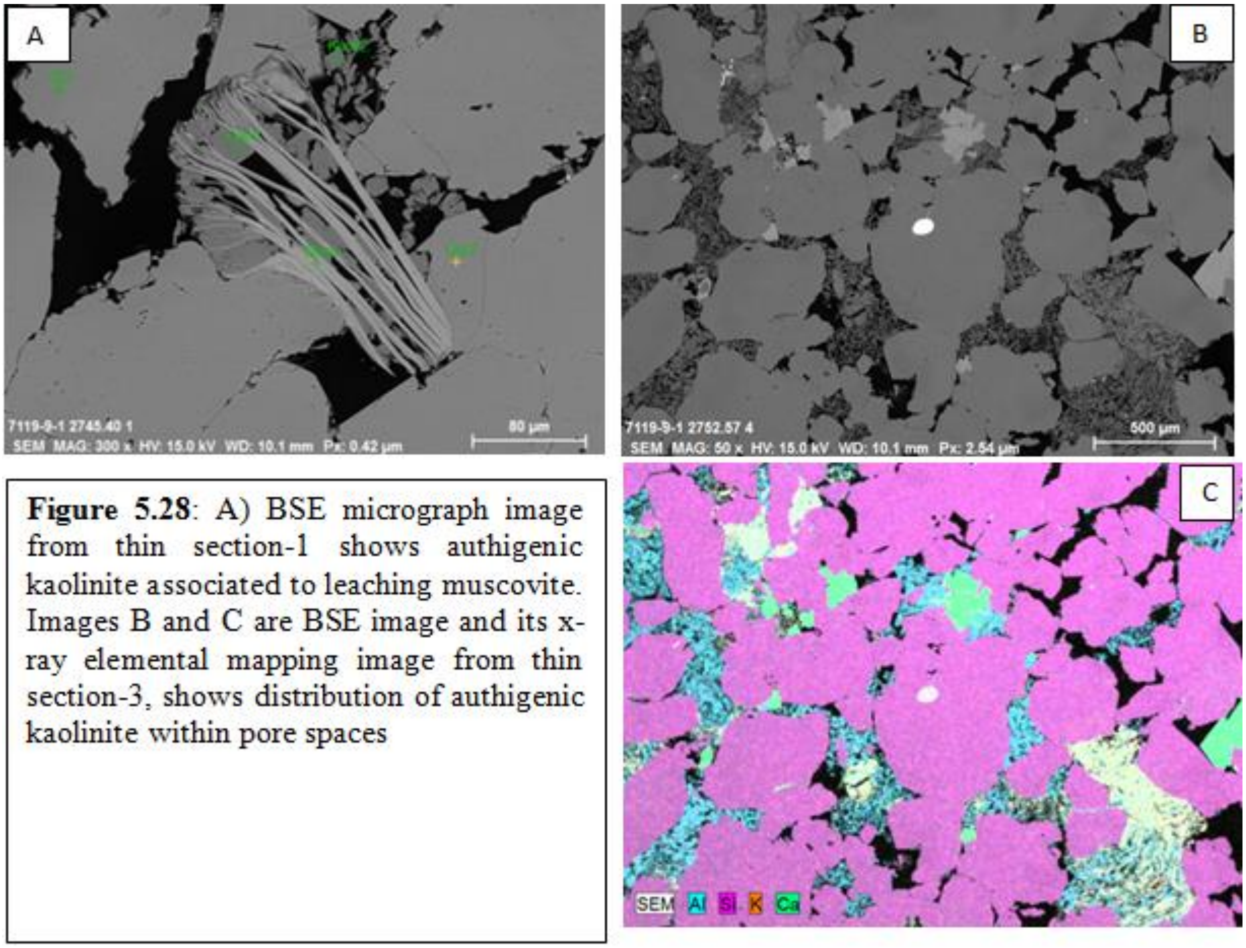

Figure 5.28: A) BSE micrograph image from thin section-1 shows authigenic kaolinite associated to leaching muscovite. Images B and C are BSE image and its x-ray elemental mapping image from thin section-3, shows distribution of authigenic kaolinite within pore spaces

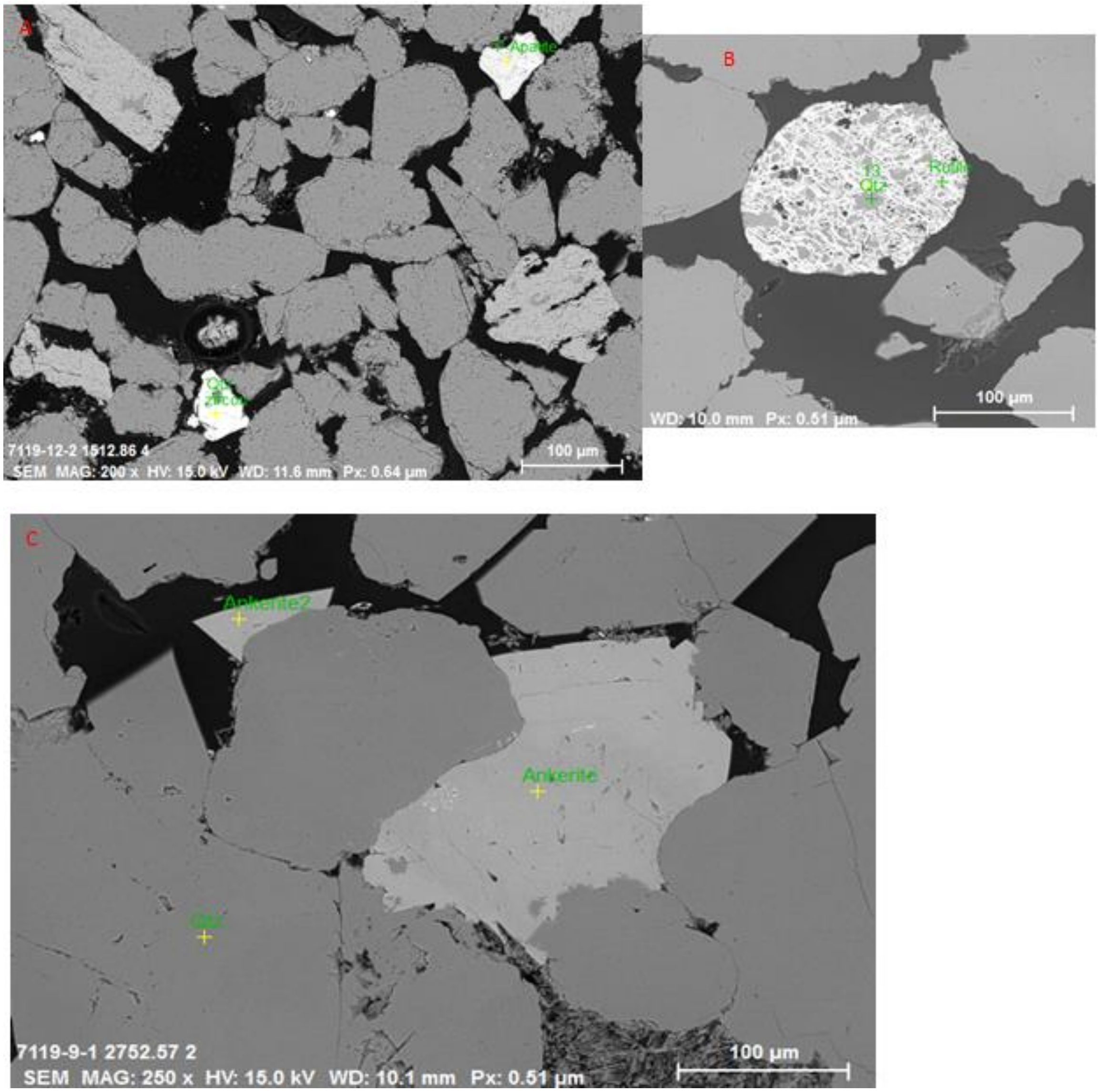

Figure 5.29: Figure displays minor mineral grain constituents such as apatite and zircon from thin section-26 (A), combined rutile and quartz thin section-15 (B), and ankerite, carbonate cement from- thin section-3 (C).

5.3 Petrophysical Properties

5.3.1 Lithology and correlation

Lithology discrimination of the Stø Formation was made based on combinations of gamma ray, neutron, and density logs (Fig. 5.30). Small intervals of coarsening up sequences with an overall fining up sequence can be noticed in the lower sand unit of well 7119/9-1. In the same unit of well 7119/12-2, gamma ray log is relatively blocky, and smoother. From the facies analyses of core samples FA-1 dominates in the lower sand unit. From the same Figure density log (blue curve) shows slight increase with increasing gamma ray log in both sand units. Cross over between density and neutron log show high negative separation in both units of well 7119/9-1, support sand units with pore spaces filled with light hydrocarbon (gas). However, incomparably higher density reading (>2.5 g/cm^3) in well 7119/9-1 than in well 7119/12-2.This could be linked to the presence of high quartz cement in well 7119/9-1, created indurated sand. In contrast, higher porosity and low quartz cement content, would give relatively lower density reading (<2.25 g/cm3, in well 7119/12-2.

Coarsening up sequence (decreasing density log) can be noticed at the bottom part of the upper sand unit in well 7119/12-2 while it decreases for the whole interval in well 7119/9-1. From the core sample observation this interval was described by facies associations-3 and 2 in well 7119/9-1, facies association-2 in well 7119/12-2. Density decreases to the top part in the later well while significant thickness is missing from the upper sand unit of well 7119/9-1. Middle Jurassic rifting favored uplift and erosion of the eastern platform in the SW Barents region and amplified structural highs as described in chapter two.

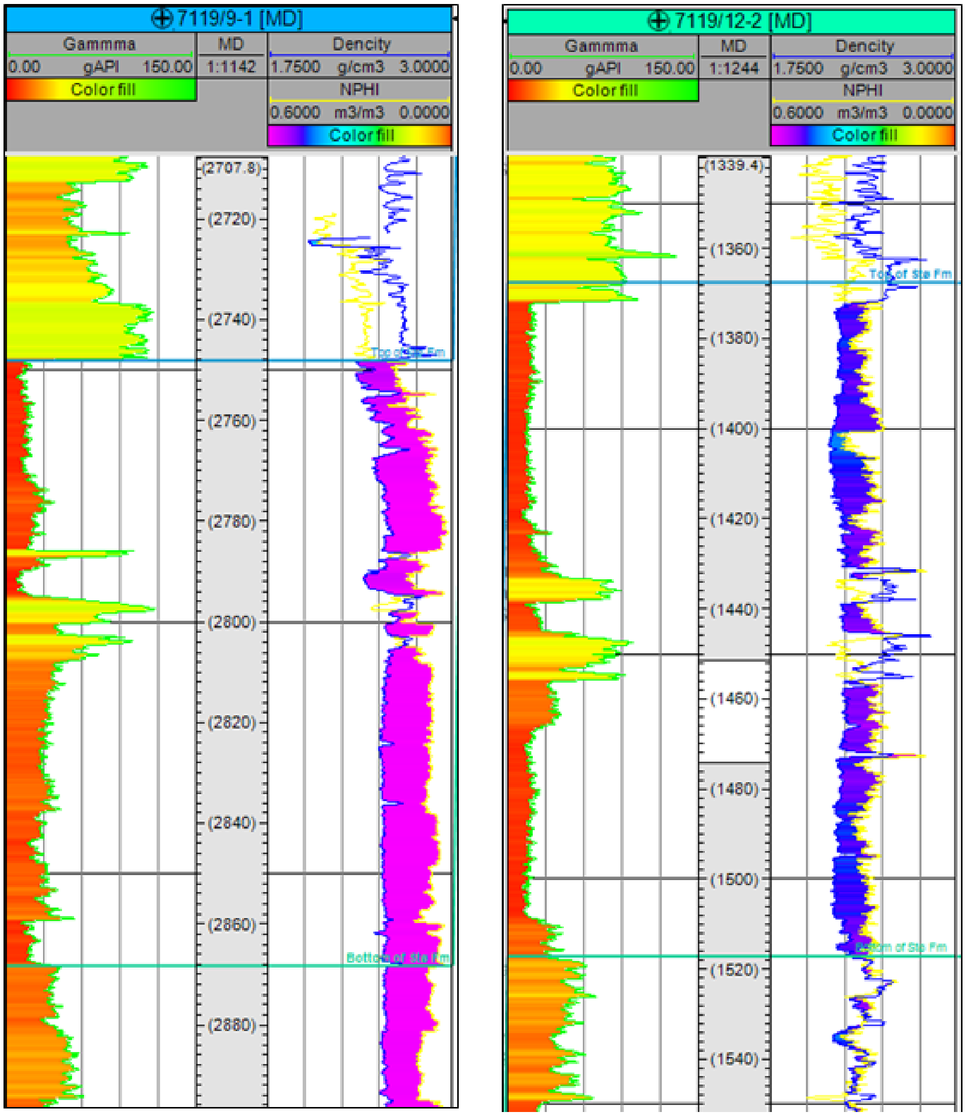

Figure 5.30: Display of gamma ray log and crossover between density and neutron porosity logs of study wells, Stø Formation marked interval. Minor coarsening upward with an overall fining sequence of the lower sand unit of 7119/9-1 can be observed. Low gamma ray reading, fining upward sequence in same unit of well 7119/12-2 can be noticed. Coarsening up sequence (decreasing density log) at the bottom part of upper unit in well 7119/12-2 and for the whole interval in well 7119/9-1 can be observed.

Shale volume estimation: - Figure 5.31 below displays the calculated shale volume for the interval of Stø Formation from gamma ray index. Almost null shale volume in the cored sand units can be observed and small shale volume generally <10% in the lower sand unit of well 7119/9-1. It reaches up to 60% in the intervening shaly horizons in 7119/9-1.

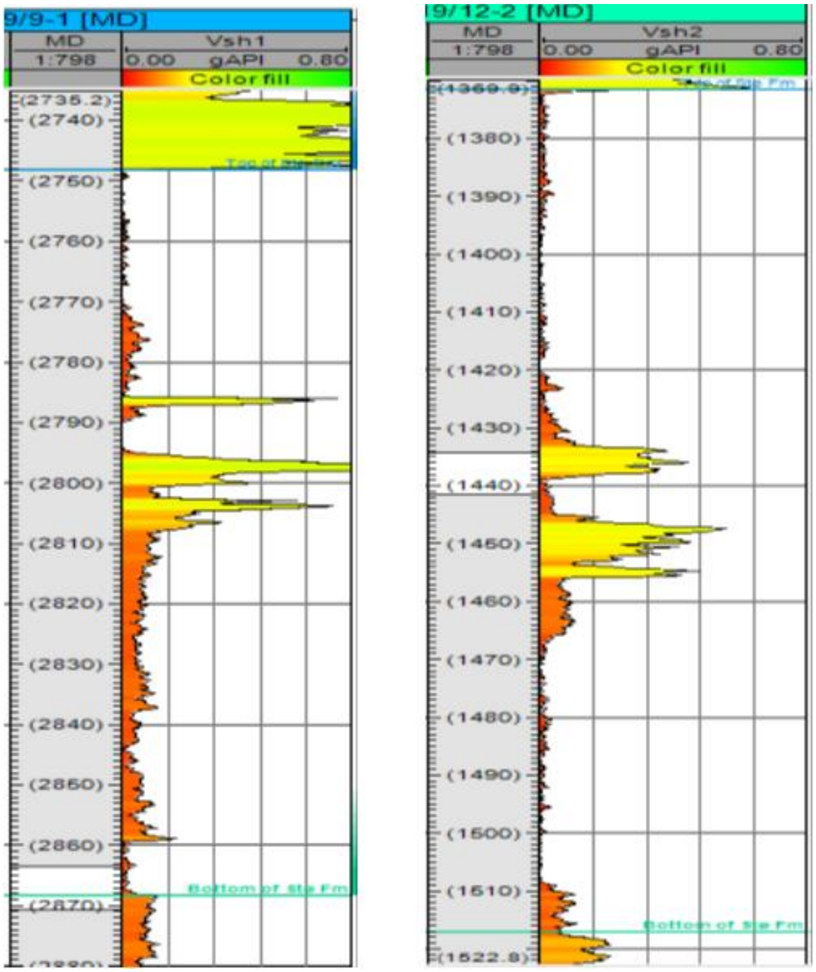

Figure 5.31: Calculated shale volume against depth plot (well-7119/9-1 left, and well-7119/12-2 right), Image is exaggerated horizontally

5.3.2 Compaction analyses

Geothermal Gradient: Geothermal gradients were calculated using the measured bottom-hole temperatures for both wells and taking an average surface temperature of 4°Cand plotted against depth (Fig. 5.32). A geothermal gradient of 33.25°C/km was calculated in 7119/9-1 while

30.59°C/km in 7119/12-2. The present depth interval of the Stø Formation is between 1378-1517m in well 7119/12-2 and 2745-2868m in 7119/9-1 that corresponds to an average temperature range of 45-55°C and 90-100°C respectively.

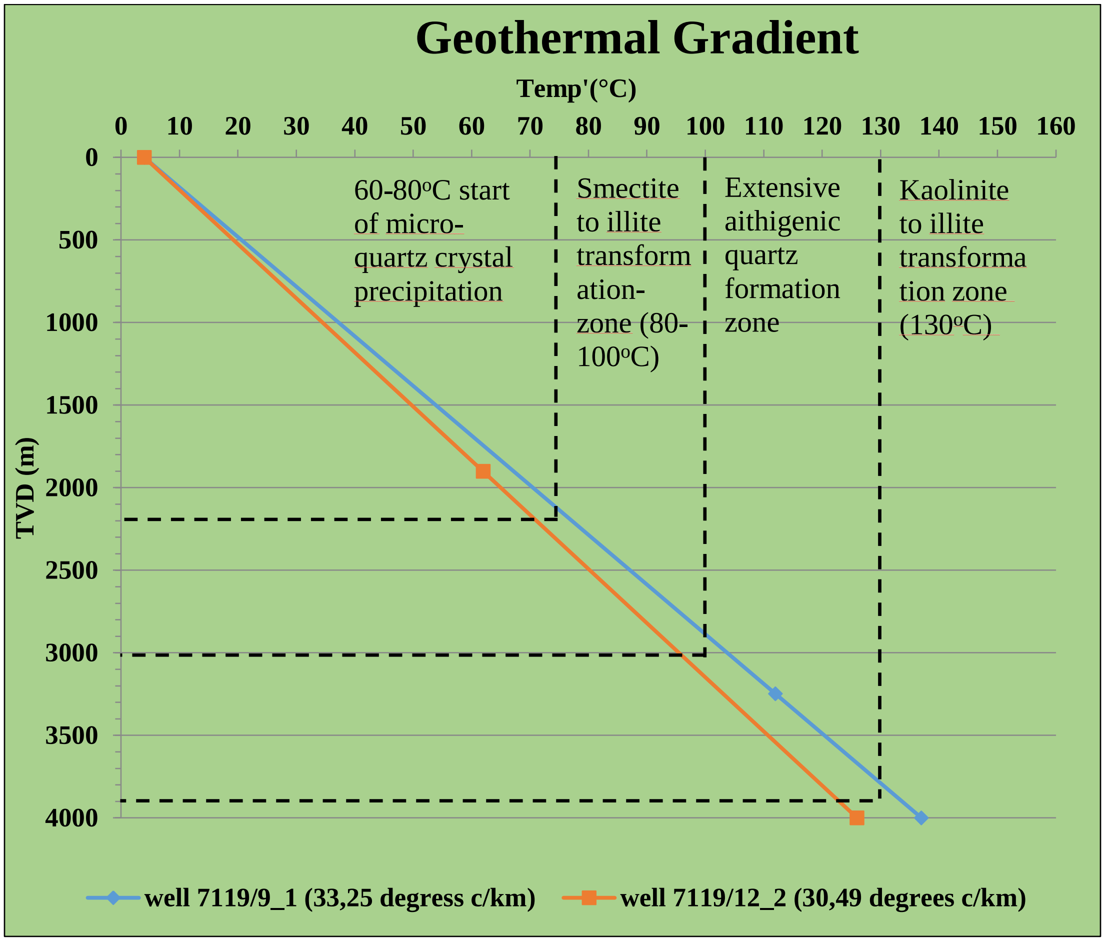

Figure 5.32: Figure displays calculated geothermal gradient using the measured bottom-hole temperature and 4°Cof mean surface temperature. Temperature zones of important chemical changes occurrences with increasing depth marked as well.

Transition zone: - Figure 5.33 below displays velocity log of both wells. Probable transition zone between mechanical and chemical compaction regime were marked (arrows) based on the observation of abrupt increase of velocity, and created major shift of velocity trend. In well 7119/12-2, a major shift indicated at a shallow depth about 1100m. This depth corresponds to a temperature range of 40-50°C as observed from the geothermal gradient (Fig. 5.32). Low velocity interval below the predicted transition zone in the same well observed. From the stratigraphic study Stø Formation is overlain by Fuglen and Hekkingen formations, with the later one is an important source rock in the western Barents Sea province.

Two abrupt increase of velocity in well 7119/9-1 were indicated as possible transition zone. The upper point lies at a depth of about 1800m which corresponds to temperature range of 60-70°C. Transition of mechanical to chemical compaction of siliciclastic sedimentary successions may differ significantly due to composition of sediment input (Bjørlykke, 1998).

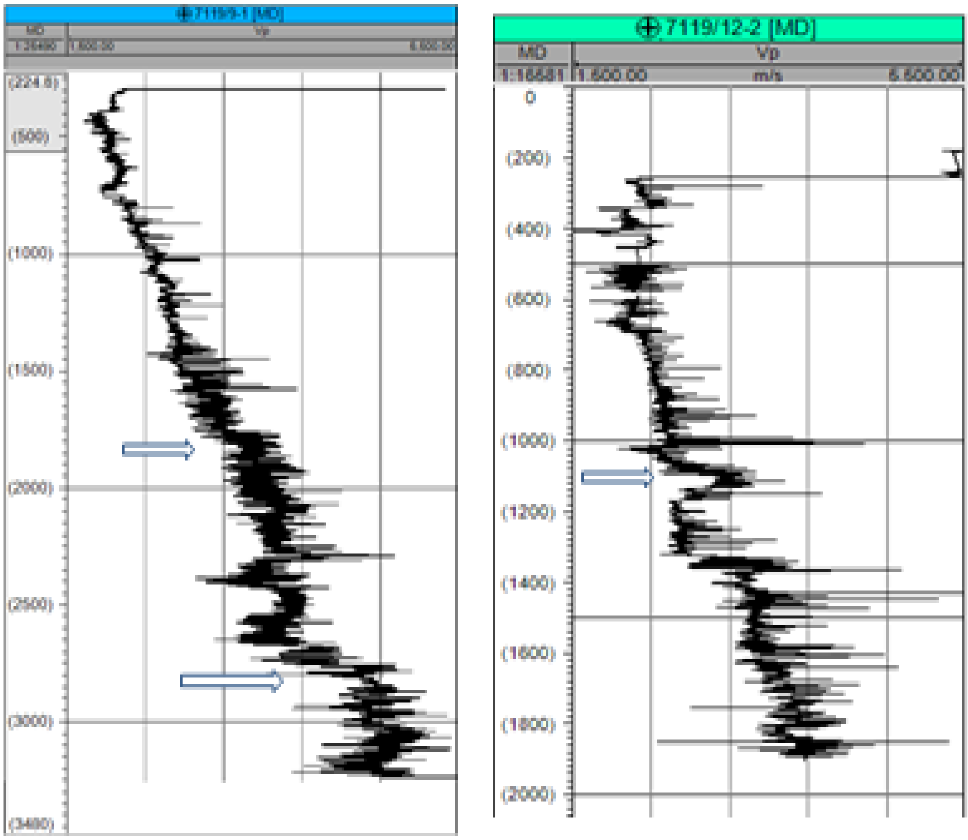

Figure 5.33: Possible transition zone of mechanical and chemical compaction inferred using velocity depth profile obtained from sonic log of study wells

Uplift Estimation

Uplift assessment using velocity profile from the shaly intervals and correlated with experimental compaction trend of kaolinite-silt 50:50 combination after (Mondol, 2009), was made in the two wells (Fig. 5.34). An uplift estimate of 750m and 500m from well 7119/9-1 and 7119/12-2 respectively can be noticed. Estimated uplift was compared with other estimations made on using multiple methods and close locations to study wells. Baig et al. (2016) estimated an exhumation between 200-900m in the location of wells of 7117/9-1*, 7119/7-1*, 7120/5-1*, and 7121/4-1*. His estimation is based on the average of sonic, shot gather, and vitrinite reflectance as mentioned in (Aven, 2017). An uplift estimate between 100 to 1050m for the same wells made (Henriksen et al., 2011). It is based on taking an average of several methods of thermal, compaction as well as apatite track analyses. * is to denote measurement retrieved from net exhumation maps instead of specific well.

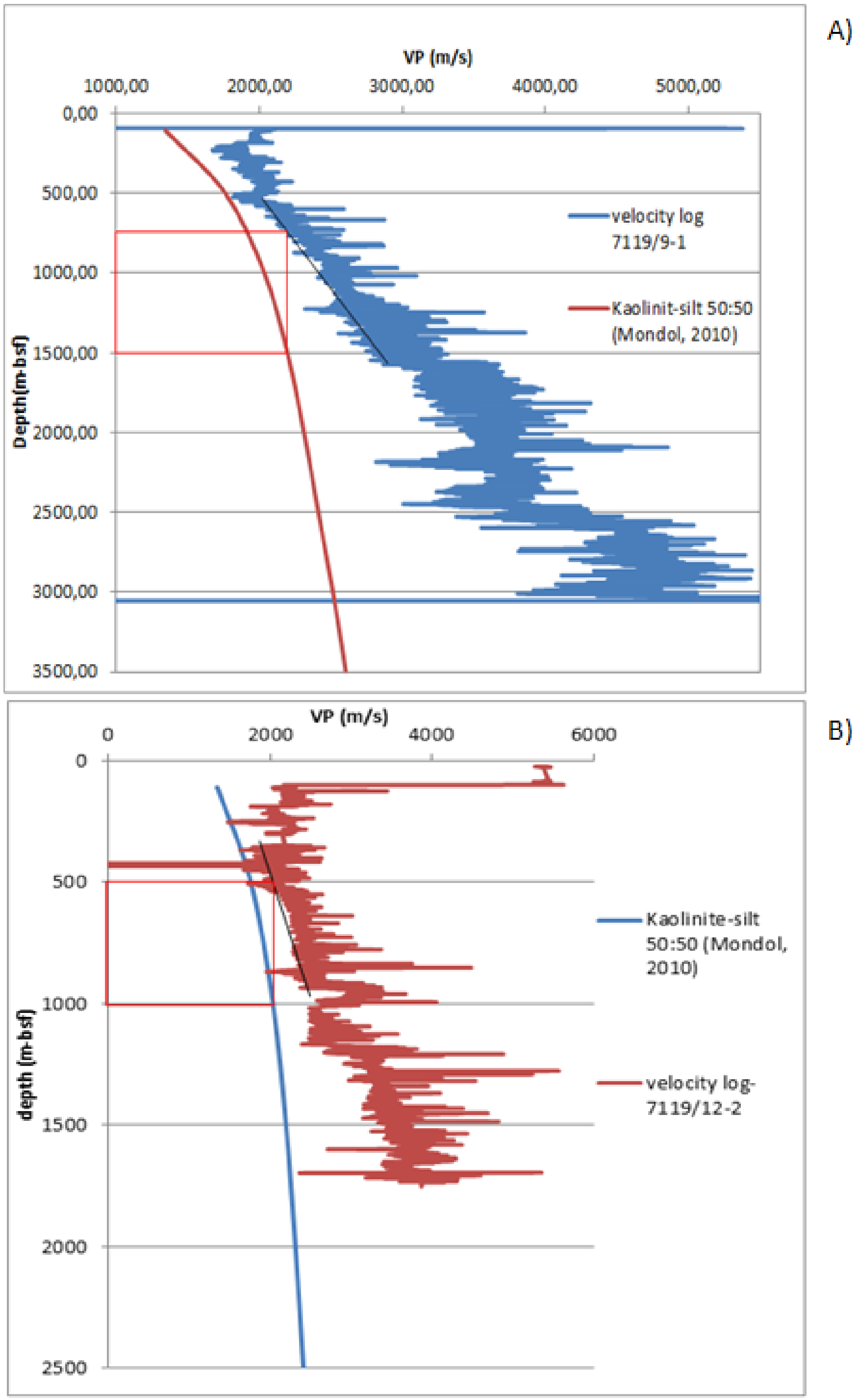

Figure 5.34: Display of velocity profiles of study wells superimposed with experimental compaction trend based on kaolinite-silt 50:50 compositions (Mondol, 2009). 750m uplift estimated from well 7119/9-1(A), and 500m from well 7119/12-2 (B).

5.3.3 Rock Physics Diagnostics

Cross-plot of total calculated porosity from density and neutron porosity logs versus velocity log for both wells (Fig. 5.35). Velocity log from well 7119/9-1 was transformed into fully water-saturated case from an estimated 20/80 ratio of hydrocarbon/water saturation using the Gaussian Fluid replacement method and keeping other parameters such as elastic properties as default. Data points from well 7119/9-1 form two trend lines with the lower unit points lay on the intermediate sand model curve implying higher pore filling minerals content. Data points from the upper sand unit of the same well (Marked area) lay above the intermediate sand model. Moreover, data points from both units of well 7119/12-2 show only little affected by contact cement.

Physical approach for quartz cement estimation from the velocity versus porosity cross-plot was performed picking data points from around thin section depths (Fig. 5.36). A better fit can be observed with the point counted quartz cement in well 7119/9-1 (Fig. 5.36A) although slight decrease with depth in contrary to the point count data. On the other hand, data points from well 7119/12-2, show higher values about two times higher than the amount of quartz cement obtained from point counting (Fig. 5.36B). Likewise, in well 7119/9-1 relatively higher gap between estimated and point counted quartz cement to the point where clean and coarser sand was observed. Nevertheless, (Hossain et al., 2014) described such method of quartz cement quantification works well for all porosity conditions. Pore-filling minerals content increases to the bottom part of upper sand unit (FA-3) in well 7119/9-1.

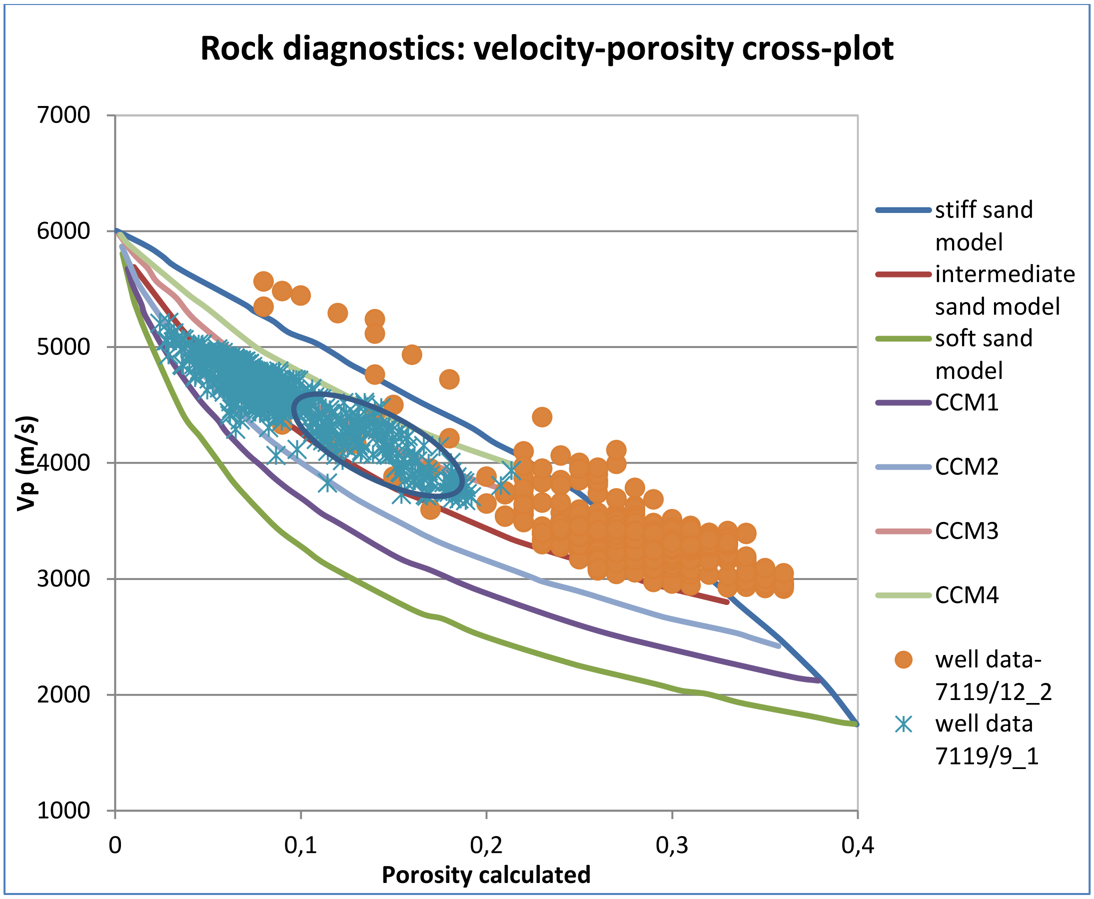

Figure 5.35: Figure displays cross-plots of total calculated porosity and velocity logs of study wells, upper unit in well 7119/9-1 (marked area). Velocity log from well 7119/9-1 was transformed into fully water saturated case using the Gaussian Fluid replacement method. Pore filling minerals and contact cement effect observed in well 7119/9-1 while pore filling cement is not important in well 7119/12-2. CCM is constant cement model

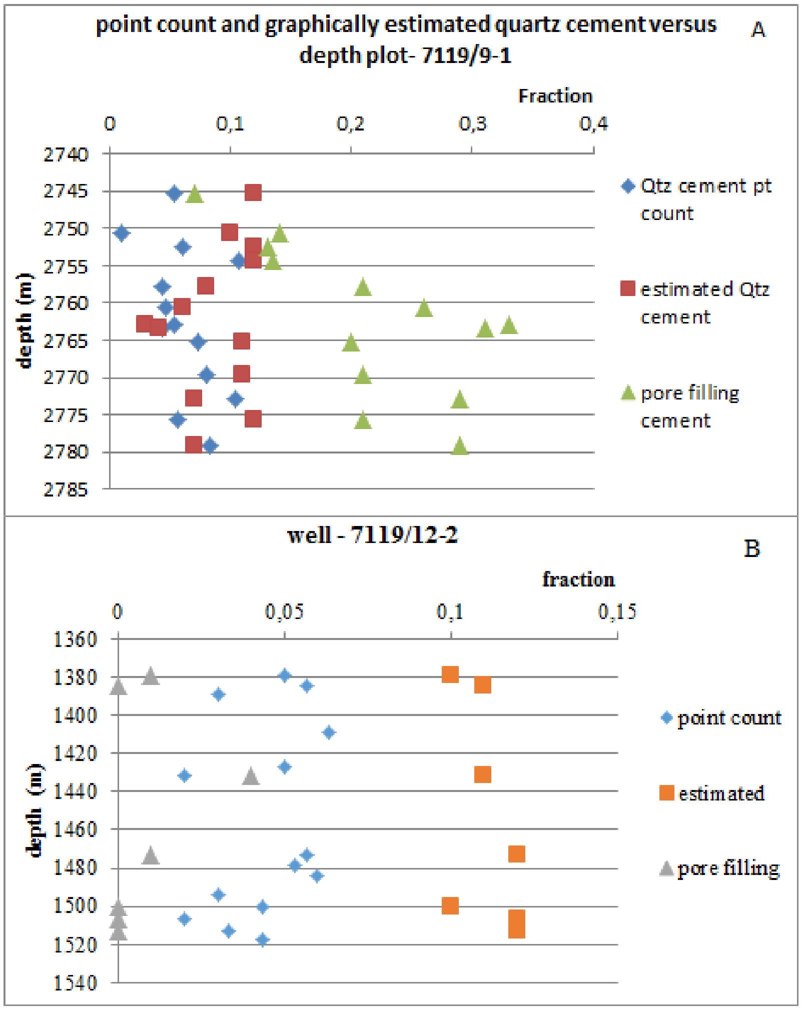

Figure 5-36: Figure displays point counted and graphically estimated quartz cement (contact cement) and estimated other pore filling minerals versus depth plot. Physical approach of quartz estimation used, after (Hossain et al., 2014)

Point counted versus calculated Porosity

Figure 5.37 below displays plot of calculated porosity and point counted porosity together against depth. There exists a good match in well 7119/9-1 and similar trend can be observed from well 7119/12-2. Calculated porosity in the non-cored sand unit of well 7119/9-1 remains generally low (<10%) and almost constant with depth. Sandstones with intermediate matrix content preserve higher porosity in deeper burial than clean sand by limiting quartz overgrowth cement (Bjørlykke et al., 1986). However, high density and velocity logs were observed in this sand unit implying chemical compaction effect. Similarly, a good correlation exists between measured and calculated porosity in the clean sand intervals of well 7119/12-2.

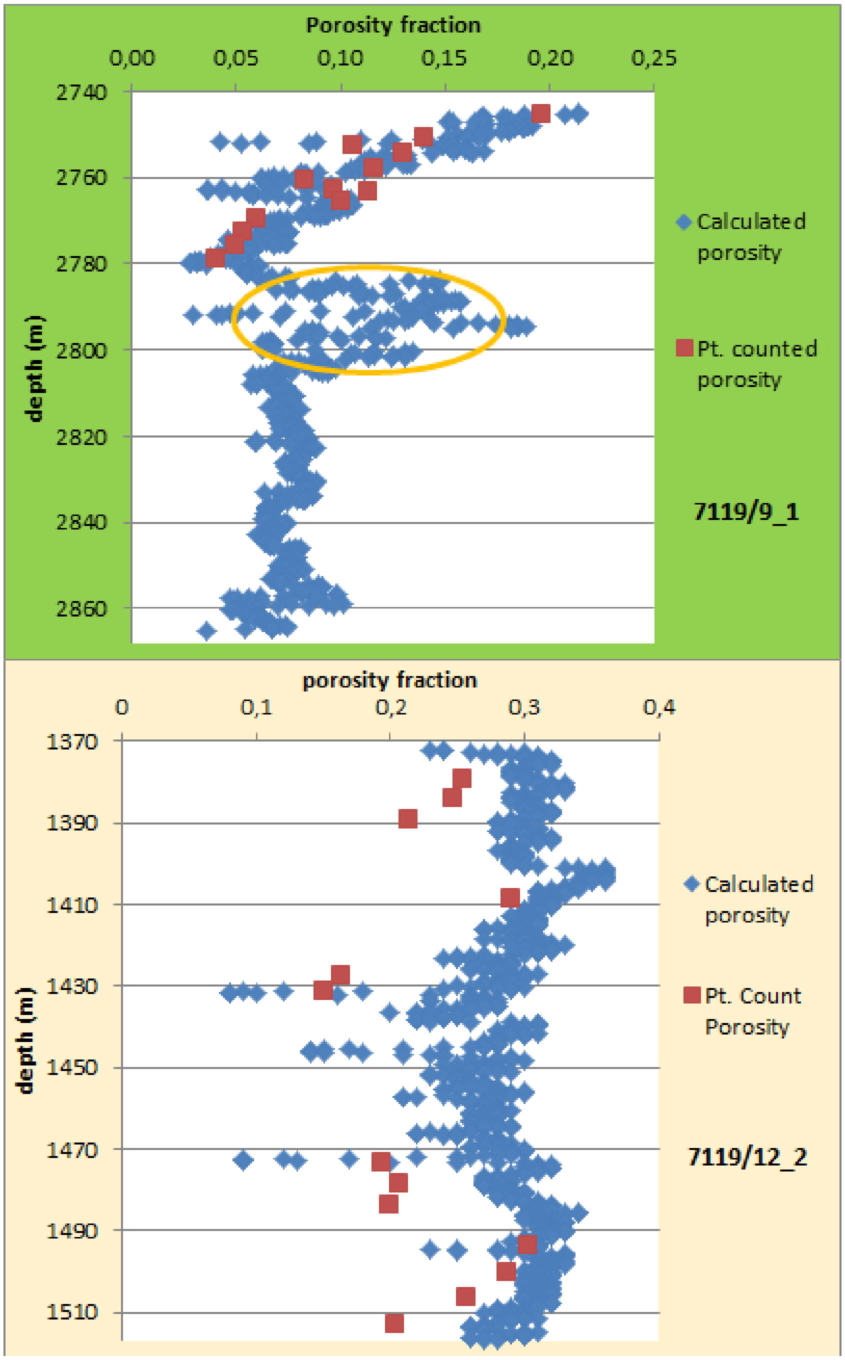

Figure 5.37: Plot of point counted and calculated porosity from density and neutron porosity logs of both wells. Yellow mark indicates shaly interval between sand units

6 DISCUSSIONS

High porosity (av. Por. = 22%) is observed in well 7119/12-2 while in well 7119/9-1 (av. Por. = 10%). This implies that the Stø Formation has best reservoir quality associated with well 7119/12-2 than well 7119/9-1. The main diagenetic processes (mechanical and chemical compaction) responsible for affecting the reservoir quality of Stø Formation sandstones including sedimentological processes will be discussed in the following section.

6.1 Sedimentary composition and depositional environment

The sediment composition of sandstones is controlled by initial composition of source rock, and different processes including weathering/erosion, transport, deposition and burial (Bjørlykke and Jahren, 2015). The Stø Formation is made up of almost exclusively of quartz, therefore it is considered as mineralogically supermature sandstone. Less stable sediment grains such as feldspar, mica and rock fragments constitute on average of less than 2% of the bulk rock volume. In addition, small fraction of authigenic and detrital matrix content was observed. X-ray diffraction and core observations also confirm mature and clean sand content of the Stø Formation. This indicated that the reservoir quality of the Stø Formation is mainly dictated by the framework detrital quartz grains response to both mechanical and chemical compaction processes as a function of burial depth. Feldspar, rock fragments and other accessory minerals thus play insignificant roles on the reservoir quality of these sandstones.

High quartz content of the Stø Formation could suggest sediment source from quartz rich to intermediate composition igneous, and quartzite as well as quartz arenite meta-sedimentary rocks. Less content of unstable minerals, could also suggest much agitation and winnowing of sediments, long transport distances implying a stable, passive continental shelf existed during the Stø Formation. Little heavy minerals content since heavy minerals could settle not far from source rock. Intermediate abrasion of sediment grains from the grain shape analyses also suggests long transport distance since rigid and fine grain content is not readily rounded.

Facies association-1 contains mud and organic draped plane parallel and cross laminations sedimentary structures, wavy mud drapes (double), intermediate bioturbation, and some wood fragments content suggesting mixed river and tide influenced shoreface depositional environment. Facies Association-2 mostly structureless, lighter color, fine-grained sand with little organic content suggests the sediments deposited in a relatively low energy, near shoreline environment. Gamma ray log also support this in which low, relatively smooth, cylindrical shape gamma in the upper sand unit suggest near shore deposition environments such as beach, and tidal distributary channel fill. For Facies association-3, the likely suggested depositional environment is shallow marine setting likely proximal lower shoreface environment. It is dominantly bioturbated, very fine, muddy sand intercalated with small units of clean, lighter, massive sand. It overlies the intervening shaly unit between the sand units deposited during maximum transgression. In addition, minor coarsening up sequences with an overall fining upward sequence observed in the gamma ray log of the lower sand unit in well 7119/9-1, which could suggest deposition in a prograding continental shelf and transgressive sea of shallow marine realm. From the petrographic grain size distribution analyses cross plot between calculated sorting and skewness (Fig. 6.1) which is used in different processes and deposition environment of sandstones (Bjørlykke, 2015) show dominantly of river influenced near shoreline environment. Depending on all the above observations, the three facies associations recognized suggested the gross depositional environment of the Stø Formation is shallow marine and deposition of sediments vary between lower to upper shoreface environments.

The depositional interpretations in this study are not far off compared to previously published works regarding the Stø Formation. three depositional environments with bases defined by transgressive episodes where the basal unit is present only in the western parts of the Hammerfest Basin, the middle unit representing maximum transgression and the highly variable uppermost unit owing to syn-depositional uplift and winnowing as well as later differential erosion in the Stø Formation was suggested (Worsley et al., 1988). In addition, sedimentological environments of the Stø Formation described ranging from transgressive, tidal, fluvial, and regressive shoreface in a variable relative sea level during an overall transgression of the basin (Klausen et al., 2017). Moreover, he described mix of reworked material and coarse-grained sediment supply from extrabasinal source areas including Caledonian provenance in the SW and

Fennoscandian provenance to the SE during the Stø Formation deposition, based on detrital zircon U-Pb geochronology data.

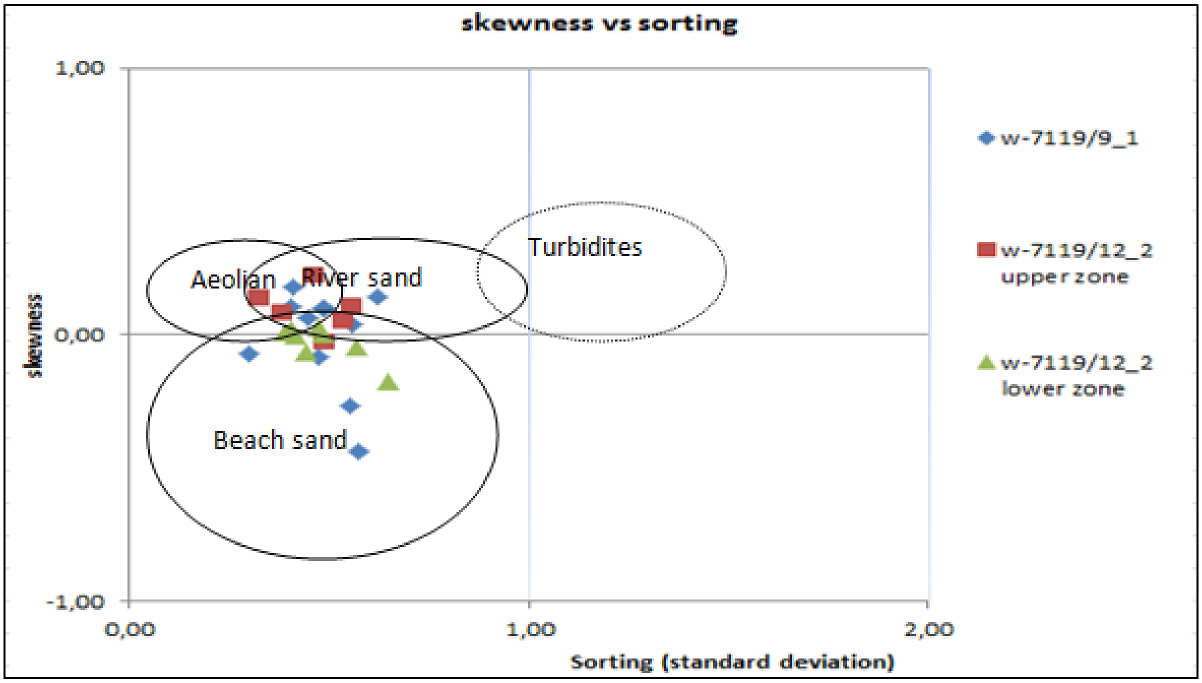

Figure 6.1: This cross plot between calculated sorting and skewness is used to distinguish different processes and deposition environments of sandstones (Bjørlykke, 2015). Note shapes are added for clarification only

6.2 Near Surface Alteration

There is an indication that the Stø Formation is affected by the meteoric water flushing. This is evidenced by the formation of authigenic kaolinite in the pore-spaces associated with dissolved muscovite (Fig. 5.28A, B). Optical microscope observation of thin sections result shows mostly no potassium feldspar content of the Stø sandstone (Fig. 5.6), which may suggest it was completely dissolved during shallow burial. In relative to that since muscovite is relatively stable much of the authigenic kaolinite observed to occur dispersed in pore spaces could be sourced from K-feldspar leaching. Little early diagenetic cement such as carbonate and iron oxide cement were observed on average of 1% from the bulk volume. Bioturbation was observed in the fine sand intervals especially in FA-3, which occurs at the bottom part of upper sand unit of well 7119/9-1.

6.3 Intermediate burial

Sediment compaction is function of mineral composition and textural characteristics of input sediments, which is in turn controlled by sediment provenance and depositional environment (Bjørlykke and Jahren, 2015). The Stø Formation recognized dominantly of quartz composition, well to moderately sorted, mostly fine-grained sand from the optical microscope inspection of thin sections. Mostly subangular to subrounded grain shape was observed, however unabling to properly delineate the quartz growth on detrital grains without dust rims might have introduced uncertainties on sediment texture descriptions.

6.3.1 Mechanical compaction

Reservoir porosity of the Stø Formation is dominantly controlled by mechanical compaction though some quartz cement recognized in well 7119/12-2 otherwise primarily chemical compaction control in well 7119/9-1. An average IGV of 29% was measured in the Stø reservoir sand of well 7119/12-2 whereas 19% in the other well. Supermature composition, well to moderately sorted, and fine to medium-grained sand content of the Stø Formation in both wells recognized, which could suggest high capability of preserving IGV/IGP against increased effective stress under intermediate burial depths, in which the first well is in agreement with. Low IGV values (<20%) in well 7119/9-1 recognized, though abundant quartz cementation observed as well, meaning mechanical compaction could have been stabilized at an average burial depth of 2000m. Only small fraction, up to 4% of quartz cement can effectively shut down mechanical compaction effect of reducing IGV and it typically reduced to only 25-30% or even more in shallow burial depths (1-2km) of well-sorted, quartz rich sandstones (Bjørlykke and Jahren, 2015). This discrepancy is likely associated with the uncertainty that quartz overgrowth might have been underestimated especially in the heavily cemented part of the Stø sandstone. There was difficulty of accurately determining quartz cement amount using optical microscope during thin sections inspection where it was based on looking well-defined dust rims on detrital quartz grains (Fig. 6.2). An IGV versus average grain size cross-plot (Fig. 5.18A) shows slight IGV increase with decreasing grain size in data point from well 7119/12-2 where less quartz cement observed which is in agreement with previous works such as (Chuhan et al., 2002, 2003) states coarser sand grains compact faster than fine grained sand. Otherwise, data points from well 7119/9-1 show the opposite that is associated with the above uncertainty. Relatively higher grains angularity was observed in the same well which may have contributed to the reduced IGV values since effective stress concentrated on grain edges so will be crushed and reduce IGV.

Present burial depth of the Stø Formation is on average 2700m in well 7119/9-1, and 1400m in well 7119/12-2. An uplift of 750m and 500m in the respective wells was estimated as displayed in (Fig. 5.34), and suggest deeper burial depths up to 3450m and 1900m respectively. This suggests that the Stø Formation had been buried to chemical compaction (quartz cementation) zone where it was described to occur at threshold temperature range of 70-80^{o}C corresponding to average burial depth of 2000m and typical temperature gradient of 25-35^{o}C (Bjørlykke and Jahren, 2015). This is in agreement with the observed quartz cement during petrographic observation of thin sections where heavy quartz cement noticed in the deeply buried Stø sandstone.

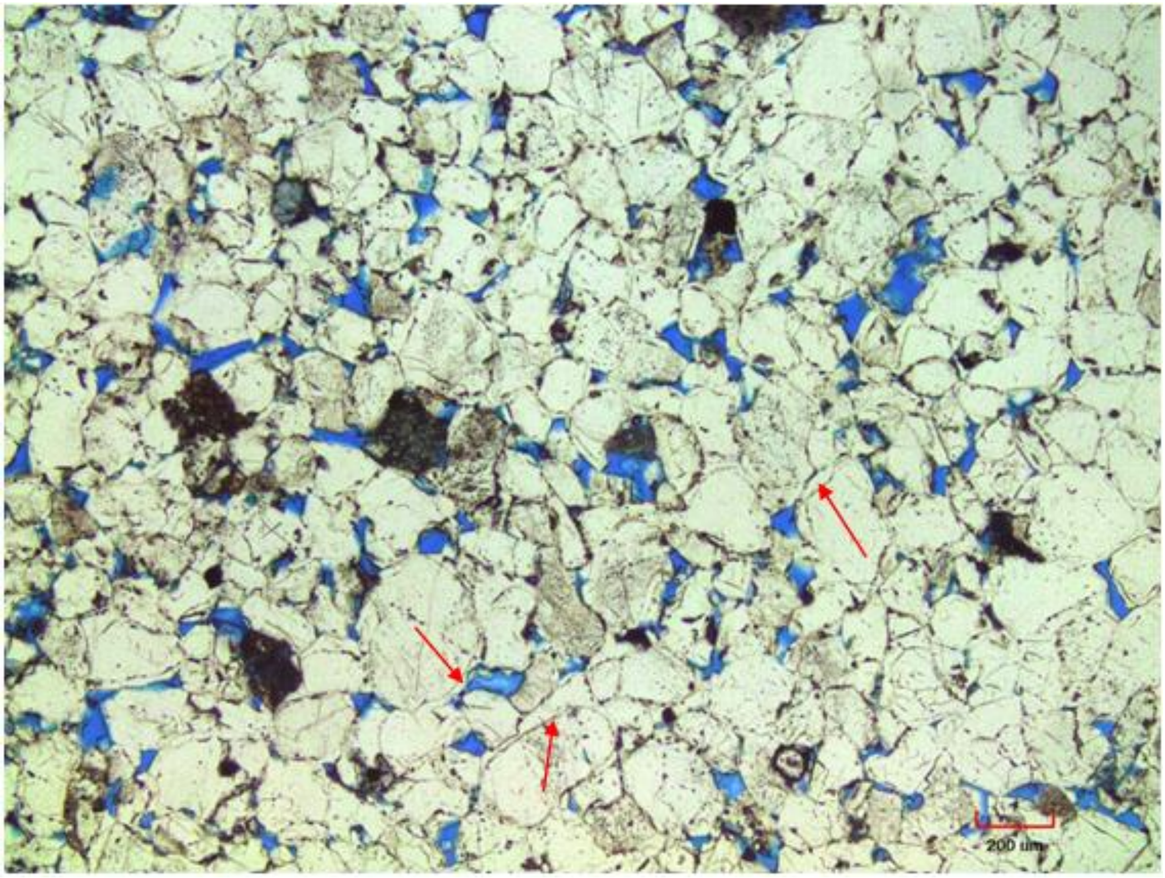

Figure 6.2: Figure displays plane polarized microscope image obtained from thin section-11, upper sand unit of well 7119/9-1. Arrows indicate clearly identified dust rims around detrital quartz grains, whereas it is difficult to observe in the much cement bound grains.

6.3.2 Chemical compaction

As described above reservoir porosity of the Stø Formation in well 7119/9-1 is dominantly controlled by chemical compaction (quartz cementation). This can be noticed in Figure 5.10 where the linearized porosity distribution among individual thin sections is in inverse relation with quartz cement. Petrographic (CL) observation, also confirmed extensive quartz cementation occurrence (Fig. 5.25A, B). Several macrostylolites were observed in the lower part of upper sand unit (FA-3) that suggests it is primary source of dissolved silica for the quartz cementation.

In addition, thin sections with high and low quartz cement content observed in relation to nearest stylolite occurrences (Fig. 5.11). Those of high quartz cement content located at a centimeter scale distance from the nearest stylolites than those of low quartz cement content at meter scale. Stylolites concentrated mostly at interfaces between the bioturbated, dark, muddy and lighter, clean sand units implying clay facilitated grain dissolution. From the petrophysical analyses, higher values of estimated pore-filling minerals (Fig. 5.36A) may suggest relatively higher clay minerals content of the dirty units since thin sections are derived from the cleaner intervals. Generally low matrix content of the Stø Formation was observed from the thin sections optical microscope study that could suggest clay-induced microstylolites is not important source of dissolved silica. This is supported by the low gamma ray and sand deposition under much reworking in the shore face environment from the sediment core interpretation. Similarly, quartz cement content observed to increase with decreasing grain size (Fig. 5.17B). Fine sand content is implying increased available surface area where authigenic quartz grows on.

Some thin sections were observed with exceptionally high porosity content in the abundantly quartz cemented upper sand unit of well 7119/9-1. Petrographic X-ray elemental mapping and SEM analyses (Fig. 5.26 and 5.27), thin illitic clay coating on detrital quartz grains noticed. This could suggest dissolved silica saturation is not the limiting factor for the growth of authigenic quartz on detrital grains. The rate of quartz cementation is function of temperature, time and quartz surface area available (Walderhaug, 1994, 1996, 2000). From the core sample analyses, FA-2 in well 7119/9-1 was suggested near shoreline deposition environment with subareal exposure. This implies relatively coarser sand content and higher permeability during deposition and the possibility of infiltrated illitic matrix content. It is suggested that there is potential for considerable porosity and permeability to be preserved in the deeply buried Stø Formation in the general Barents Sea region linked to illite clay coating (Hansen et al., 2017) . Furthermore, he mentioned that the illite clay could be originated from clay infiltration processes prior to final deposition in the proximal shallow marine provinces.

From the uplift analyses, it was suggested that the Stø Formation could have been buried to average depths of 3450 and 1900m. These correspond to average temperatures of 120-130^{o}C and 60-70^{o}C in wells 7119/9-1 and 7119/12-2 respectively. The Stø Formation is now at an average temperature of 50^{o}C in well 7119/12-2 below the threshold quartz cementation regime whereas it is at about 90-100^{o}C in the other well. This suggests the Stø Formation was not buried to elevated temperatures as well as for shorter period in the well location of 7119/12-2. However, uplift estimation was based on specific material (kaolinit-silt 50:50) experimental compaction trend (Mondol, 2009) and more accurate measurement could estimate deeper burial. Some quartz cementation was observed in this well though porosity is controlled primarily by mechanical compaction. The Stø Formation remains under elevated temperature in well 7119/9-1, which is in agreement with the extensive quartz cementation observed.

6.3.3 Clay minerals transformation

Only little fibrous pore bridging form of illite minerals was observed during Petrographic SEM analyses. It was hardly seen chlorite clay minerals as well. This was also supported by the X-ray diffraction analyses where only small fraction of mica/illite combination was observed in some of the powder samples and chlorite was not recognized. This may be is due to lack of iron rich clay mineral precursors such as smectite in the primary sediment composition which is important for the precipitation of authigenic illite at deeper burial of sandstones (Bjørlykke, 1998). From the sediment core analyses sandstone deposition at marine realm recognized for the Stø Formation, implying kaolinite formation was favored over smectite from the weathering of silicate minerals. Kaolinite/dickite dominates in the clay fraction of the bulk composition. Petrographic SEM analyses show kaolinite occurrences associated with leaching muscovite (Fig. 5.28A, B) and suggest that most potassium feldspar could have been leached out during deposition. From the optical microscope analyses only some of the thin sections counted to have little potassium feldspar minerals and negligible microcline feldspar in the X-ray diffraction analyses of powder samples which suggest kaolinite to illite transformation is not possible. Illite formation from kaolinite requires average temperature of 130^{o}C and it needs potassium ion to proceed in which mostly sourced from K-feldspar if present nearby (Bjørlykke and Jahren, 2015). In the absence of potassium, kaolinite remains stable even at higher temperatures.

6.3.4 Reservoir properties

Reservoir porosity of the Stø Formation varies mostly between 5 to 12% in well 7119/9-1, with an average of about 10%. Only small fraction of secondary porosity (av. of 0.3%) was counted commonly associated with dissolving plagioclase feldspar and rock fragments. Calculated porosity from density and neutron porosity logs show lower, generally less than 10% in the lower sand unit of this well. This may suggest sand unit is quartz cemented since it is supported by the high density greater than 2.5g/cm^3 and an average of 4598.25m/s velocity log readings though high negative separation between density and neutron porosity log cross over suggest porous sandstone of gas content.

Point counted porosity in well 7119/12-2 varies between 15-30% of the bulk volume with an average value of 22%. Only 0.2% is contributed from intra-granular dissolution of muscovite, feldspar, and some fractured rock fragments. Small fraction of quartz cement was observed in this well implying porosity is primarily controlled by mechanical compaction. Low density generally less than 2.25g/cm^3 and average 3361.74m/s velocity logs observed in the Stø interval of this well. This supports Stø Formation contains highly porous sand and affected by contact cement in this well location. Experimental compaction of Etive sand which is clean, well sorted sand from the North Sea region (Marcussen et al., 2010) shows an average of 2500m/s velocity to average burial depth of 2km. Generally, small fraction of matrix content, and little fibrous illite was recognized in the Stø Formation that suggests good reservoir permeability. Clean, quartz rich, well-sorted sand was observed from the petrographic analyses and was supported by the low gamma ray log. Sediment core sample study reveal bioturbated, very fine, muddy sand dominated at the bottom part of upper sand unit and more shaly sand in the lower sand unit from the gamma ray log in well 7119/9-1 could suggest limited vertical permeability. More importantly, much porosity is destroyed by quartz cementation in this well, which suggests degraded reservoir quality of the Stø sandstone.

7 CONCLUSIONS

- Petrographic mineralogical and textural composition show that the two sand units of the Stø Formation is quartz rich dominantly fine grained and well sorted sand. In addition, from the grain shape observation dominantly of intermediate roundness observed. X-ray diffraction bulk mineral composition also shows predominantly quartz composition. From the sediment core sample observation fine to medium grained mostly lighter sandstone content of the Stø Formation.

- Near surface diagenetic processes such as bioturbation is observed usually in the muddy sand intervals. Leaching of unstable minerals usually, muscovite associated with kaolinite observed during the SEM analyses implying most potassium feldspar could have been leached during deposition since it is relatively less stable. Carbonate cement dominantly of ankerite was also observed filling pore-spaces.

- Higher IGV values on average of 29% from both sand units in well 7119/12-2 was measured in contrast to low IGV values on average of 19% was measured in well 7119/9-1. uncertainty that quartz cement could have been underestimated due to lack of clear dust rims under optical microscope for some of the detrital quartz grains could likely result in the low IGV values observed.

- Illite coating of quartz grains recognized in some of high porosity counted thin sections in the deeply buried Stø sandstone of well 7119/9-1 though porosity is dominantly destroyed by quartz cementation. High density and velocity log readings in the lower sand unit of this well could imply less preserved porosity or cemented intervals with quartz.

- In general, this study indicated that quartz cement is an important porosity-occluding material in Stø Formation sandstones that have been buried deeper. Moreover, an increase in quartz cementation was noted as a function of burial depth while porosity decreases. This implies that the degree of quartz cementation is the main control on the reservoir properties. However, what the origin of quartz cement is an important question to be answered. Macrostylolites were observed at the interface between organic rich muddy sandstones and clean sandstones contacts. Strongly quartz cemented intervals were also noted close to this macrostylolites (~cm scale). This indicates that the distribution of macrostylolites influenced the processes of quartz cementation and controlled the location and amounts of quartz cement. The chemical compaction processes expressed through macrostylolites than microstylolites were probably the main process generating silica for local quartz cement. The supply of silica for quartz cement in the sandstones is thus dependent on the number of thin clay lamina within the reservoir sandstones (FA3).

- Further study should be performed based on huge data set in order to better constrain the potential reservoir porosity and permeability preservation due to illite grain coatings in the deeply buried Stø Formation.

References

Googlemaps: https://www.google.no/search?hl=en&q=google+maps&meta=&gws_rd=ssl

NPD factepages: http://factpages.npd.no/factpages/

Ajdukiewicz, J. M., and Lander, R. H., 2010, Sandstone reservoir quality prediction: The state of the art: AAPG bulletin, v. 94, no. 8, p. 1083-1091.

Ali, S. A., Clark, W. J., Moore, W. R., and Dribus, J. R., 2010, Diagenesis and reservoir quality: Oilfield Review, v. 22, no. 2, p. 14-27.

Aven, E., 2017, Is it possible to estimate the magnitude of uplift and erosion by the use of check-shot data and average velocity?: NTNU.

Avseth, P., Dvorkin, J., Mavko, G., and Rykkje, J., 2000, Rock physics diagnostic of North Sea sands: Link between microstructure and seismic properties: Geophysical Research Letters, v. 27, no. 17, p. 2761-2764.

Baig, I., Faleide, J. I., Jahren, J., and Mondol, N. H., 2016, Cenozoic exhumation on the southwestern Barents Shelf: Estimates and uncertainties constrained from compaction and thermal maturity analyses: Marine and Petroleum Geology, v. 73, p. 105-130.

Berger, G., Lacharpagne, J.-C., Velde, B., Beaufort, D., and Lanson, B., 1997, Kinetic constraints on illitization reactions and the effects of organic diagenesis in sandstone/shale sequences: Applied Geochemistry, v. 12, no. 1, p. 23-35.

Berglund, L., Augustson, J., Færseth, R., Gjelberg, J., and Ramberg-Moe, H., 1986, The evolution of the Hammerfest Basin: Habitat of Hydrocarbons on the Norwegian Continental Shelf. Graham & Trotman, London, p. 319-338.

Bjorlykke, K., and Egeberg, P., 1993, Quartz cementation in sedimentary basins: AAPG bulletin, v. 77, no. 9, p. 1538-1548.

Bjørlykke, K., 1998, Clay mineral diagenesis in sedimentary basins—a key to the prediction of rock properties. Examples from the North Sea Basin: Clay minerals, v. 33, no. 1, p. 15-34.

Bjørlykke, K., 2015, Introduction to Sedimentology, Petroleum Geoscience, Springer, p. 31-90.

Bjørlykke, K., Aagaard, P., Dypvik, H., Hastings, D., and Harper, A., 1986, Diagenesis and reservoir properties of Jurassic sandstones from the Haltenbanken area, offshore mid-Norway: Habitat of hydrocarbons on the Norwegian continental shelf, p. 275-286.

Bjørlykke, K., and Jahren, J., 2010, Sandstones and sandstone reservoirs, Petroleum Geoscience, Springer, p. 113-140.

-, 2015, Sandstones and sandstone reservoirs, Petroleum Geoscience, Springer, p. 119-149.

Bloch, S., Lander, R. H., and Bonnell, L., 2002, Anomalously high porosity and permeability in deeply buried sandstone reservoirs: Origin and predictability: AAPG bulletin, v. 86, no. 2, p. 301-328.

Boggs, S., 2009, Petrology of sedimentary rocks, Cambridge University Press.

Boles, J. R., and Franks, S. G., 1979, Clay diagenesis in Wilcox sandstones of southwest Texas: implications of smectite diagenesis on sandstone cementation: Journal of Sedimentary Research, v. 49, no. 1.

Chuhan, F. A., Kjeldstad, A., Bjørlykke, K., and Høeg, K., 2002, Porosity loss in sand by grain crushing—Experimental evidence and relevance to reservoir quality: Marine and Petroleum Geology, v. 19, no. 1, p. 39-53.

-, 2003, Experimental compression of loose sands: relevance to porosity reduction during burial in sedimentary basins: Canadian Geotechnical Journal, v. 40, no. 5, p. 995-1011.

Dalland, A., Worsley, D., and Ofstad, K., 1988, A lithostratigraphic scheme for the mesozoic and cenozoic and succession offshore mid-and northern norway, Oljedirektoratet.

Day-Stirrat, R. J., Milliken, K. L., Dutton, S. P., Loucks, R. G., Hillier, S., Aplin, A. C., and Schleicher, A. M., 2010, Open-system chemical behavior in deep Wilcox Group mudstones, Texas Gulf Coast, USA: Marine and Petroleum Geology, v. 27, no. 9, p. 1804-1818.

Dengo, C., and Røssland, K., 2013, Extensional tectonic history of the western Barents Sea: Structural and Tectonic Modelling and Its Application to Petroleum Geology, v. 1, p. 91-107.

Dimakis, P., Braathen, B. I., Faleide, J. I., Elverhøi, A., and Gudlaugsson, S. T., 1998, Cenozoic erosion and the preglacial uplift of the Svalbard–Barents Sea region: Tectonophysics, v. 300, no. 1, p. 311-327.

Doebelin, N., and Kleeberg, R., 2015, Profex: a graphical user interface for the Rietveld refinement program BGMN: Journal of applied crystallography, v. 48, no. 5, p. 1573-1580.

Doré, A., 1991, The structural foundation and evolution of Mesozoic seaways between Europe and the Arctic: Palaeogeography, Palaeoclimatology, Palaeoecology, v. 87, no. 1-4, p. 441-492.

-, 1995, Barents Sea geology, petroleum resources and commercial potential: Arctic, p. 207-221.

Doré, A., and Jensen, L., 1996, The impact of late Cenozoic uplift and erosion on hydrocarbon exploration: offshore Norway and some other uplifted basins: Global and Planetary Change, v. 12, no. 1-4, p. 415-436.

Doré, A., Lundin, E., Jensen, L., Birkeland, Ø., Eliassen, P., and Fichler, C., Principal tectonic events in the evolution of the northwest European Atlantic margin, *in* Proceedings Geological society, London, petroleum geology conference series1999, Volume 5, Geological Society of London, p. 41-61.

Dvorkin, J., and Nur, A., 1996, Elasticity of high-porosity sandstones: Theory for two North Sea data sets: Geophysics, v. 61, no. 5, p. 1363-1370.

Dypvik, H., 1983, Clay mineral transformations in Tertiary and Mesozoic sediments from North Sea: AAPG Bulletin, v. 67, no. 1, p. 160-165.

Ehrenberg, S., Aagaard, P., Wilsont, M., Frasert, A., and Duthiet, D., 1992, DEPTH-DEPENDENT TRANSFORMATION OF KAOL IN ITE TO D ICK ITE IN SANDSTONES OF THE NORWEGIAN CONTINENTAL SHELF.

Eldholm, O., Faleide, J. I., and Myhre, A. M., 1987, Continent-ocean transition at the western Barents Sea/Svalbard continental margin: Geology, v. 15, no. 12, p. 1118-1122.

Faleide, J., Gudlaugsson, S., Eldholm, O., Myhre, A., and Jackson, H., 1991, Deep seismic transects across the sheared western Barents Sea-Svalbard continental margin: Tectonophysics, v. 189, no. 1, p. 73-89.

Faleide, J., Vågnes, E., and Gudlaugsson, S., Late Mesozoic–Cenozoic evolution of the southwestern Barents Sea, *in* Proceedings Geological Society, London, Petroleum Geology Conference series1993, Volume 4, Geological Society of London, p. 933-950.

-, Late Mesozoic–Cenozoic evolution of the southwestern Barents Sea, *in* Proceedings Geological Society, London, Petroleum Geology Conference series1993b, Volume 4, Geological Society of London, p. 933-950.

Faleide, J. I., Gudlaugsson, S. T., and Jacquart, G., 1984, Evolution of the western Barents Sea: Marine and Petroleum Geology, v. 1, no. 2, p. 123IN1129IN5137-1128IN4136IN8150.

Faleide, J. I., Solheim, A., Fiedler, A., Hjelstuen, B. O., Andersen, E. S., and Vanneste, K., 1996, Late Cenozoic evolution of the western Barents Sea-Svalbard continental margin: Global and Planetary Change, v. 12, no. 1-4, p. 53-74.

Faleide, J. I., Tsikalas, F., Breivik, A. J., Mjelde, R., Ritzmann, O., Engen, O., Wilson, J., and Eldholm, O., 2008, Structure and evolution of the continental margin off Norway and the Barents Sea: Episodes, v. 31, no. 1, p. 82-91.

Faleide, J. I., Vågnes, E., and Gudlaugsson, S. T., 1993a, Late Mesozoic-Cenozoic evolution of the south-western Barents Sea in a regional rift-shear tectonic setting: Marine and Petroleum Geology, v. 10, no. 3, p. 186-214.

Folk, R. L., 1980, Petrology of sedimentary rocks, Hemphill Publishing Company.

Folk, R. L., and Ward, W. C., 1957, Brazos River bar: a study in the significance of grain size parameters: Journal of Sedimentary Research, v. 27, no. 1.

Gabrielsen, R., 1990, Characteristics of joints and faults: Barton & Stephansson. publ. Balkema, Rotterdam, p. 11-17.

Gabrielsen, R., Færseth, R., Steel, R., Idil, S., and Kløvjan, O., 1990a, Architectural styles of basin fill in the northern Viking Graben: Tectonic Evolution of the North Sea Rifts. Clarendon Press, Oxford, p. 158-179.

Gabrielsen, R. H., Faerseth, R. B., and Jensen, L. N., 1990b, Structural Elements of the Norwegian Continental Shelf. Pt. 1. The Barents Sea Region, Norwegian Petroleum Directorate.

Gabrielsen, R. H., Foerseth, R., Hamar, G., and Rønnevik, H., 1984, Nomenclature of the main structural features on the Norwegian Continental Shelf north of the 62nd parallel, Petroleum Geology of the North European Margin, Springer, p. 41-60.

Gee, D., Bogolepova, O., and Lorenz, H., 2006, The Timanide, Caledonide and Uralide orogens in the Eurasian high Arctic, and relationships to the palaeo-continents Laurentia, Baltica and Siberia: Geological Society, London, Memoirs, v. 32, no. 1, p. 507-520.

Glørstad-Clark, E., Birkeland, E., Nystuen, J., Faleide, J., and Midtkandal, I., 2011, Triassic platform-margin deltas in the western Barents Sea: Marine and Petroleum Geology, v. 28, no. 7, p. 1294-1314.

Glørstad-Clark, E., Faleide, J. I., Lundschien, B. A., and Nystuen, J. P., 2010, Triassic seismic sequence stratigraphy and paleogeography of the western Barents Sea area: Marine and Petroleum Geology, v. 27, no. 7, p. 1448-1475.

Gudlaugsson, S., Faleide, J., Johansen, S., and Breivik, A., 1998, Late Palaeozoic structural development of the south-western Barents Sea: Marine and Petroleum Geology, v. 15, no. 1, p. 73-102.

Hansen, H. N., 2016, Reservoir characterization of the Stø formation in the Hammerfest Basin, SW Barents Sea.

Hansen, H. N., Løvstad, K., Müller, R., and Jahren, J., 2017, Clay coating preserving high porosities in deeply buried intervals of the Stø Formation: Marine and Petroleum Geology, v. 88, p. 648-658.

Harwood, J., Aplin, A. C., Fialips, C. I., Iliffe, J. E., Kozdon, R., Ushikubo, T., and Valley, J. W., 2013, Quartz cementation history of sandstones revealed by high-resolution SIMS oxygen isotope analysis: Journal of Sedimentary Research, v. 83, no. 7, p. 522-530.

Henriksen, E., Ryseth, A., Larssen, G., Heide, T., Rønning, K., Sollid, K., and Stoupakova, A., 2011, Tectonostratigraphy of the greater Barents Sea: implications for petroleum systems: Geological Society, London, Memoirs, v. 35, no. 1, p. 163-195.

Hossain, Z., and MacGregor, L., 2014, Advanced rock-physics diagnostic analysis: A new method for cement quantification: The Leading Edge, v. 33, no. 3, p. 310-316.

Hossain, Z., Mukerji, T., Dvorkin, J., and Fabricius, I. L., 2011, Rock physics model of glauconitic greensand from the North Sea: Geophysics, v. 76, no. 6, p. E199-E209.

Hower, J., Eslinger, E. V., Hower, M. E., and Perry, E. A., 1976, Mechanism of burial metamorphism of argillaceous sediment: 1. Mineralogical and chemical evidence: Geological Society of America Bulletin, v. 87, no. 5, p. 725-737.

Jackson, H., Faleide, J., and Eldholm, O., 1990, Crustal structure of the sheared southwestern Barents Sea continental margin: Marine Geology, v. 93, p. 119-146.

Jacobsen, V. W., and van Veen, P., 1984, The Triassic offshore Norway north of 62 N, Petroleum geology of the north European margin, Springer, p. 317-327.

Jahren, J., and Ramm, M., 2009, The porosity-preserving effects of microcrystalline quartz coatings in arenitic sandstones: Examples from the Norwegian continental shelf: Quartz Cementation in Sandstones. Spec. Publ, v. 29, p. 271-280.

Jensen, L., and Sørensen, K., 1992, Tectonic framework and halokinesis of the Nordkapp Basin, Barents Sea: Structural and tectonic modelling and its application to petroleum geology. Norwegian Petroleum Society (NPF) Special Publication, v. 1, p. 109-120.

Johansen, S., Ostisty, B., Birkeland, Ø., Fedorovsky, Y., Martirosjan, V., Christensen, O. B., Cheredeev, S., Ignatenko, E., and Margulis, L., 1992, Hydrocarbon potential in the Barents Sea region: play distribution and potential: Arctic Geology and Petroleum Potential, Norwegian Petroleum Society (NPF), Special Publication, v. 2, p. 273-320.

Klausen, T. G., Müller, R., Sláma, J., Olaussen, S., Rismyhr, B., and Helland-Hansen, W., 2017, Depositional history of a condensed shallow marine reservoir succession: stratigraphy and detrital zircon geochronology of the Jurassic Stø Formation, Barents Sea: Journal of the Geological Society, p. jgs2017-2024.

Lander, R. H., Larese, R. E., and Bonnell, L. M., 2008, Toward more accurate quartz cement models: The importance of euhedral versus noneuhedral growth rates: AAPG bulletin, v. 92, no. 11, p. 1537-1563.

Lander, R. H., and Walderhaug, O., 1999, Predicting porosity through simulating sandstone compaction and quartz cementation: AAPG bulletin, v. 83, no. 3, p. 433-449.

Lanson, B., Beaufort, D., Berger, G., Baradat, J., and Lacharpagne, J.-C., 1996, Illitization of diagenetic kaolinite-to-dickite conversion series: Late-stage diagenesis of the Lower Permian Rotliegend sandstone reservoir, offshore of the Netherlands: Journal of Sedimentary Research, v. 66, no. 3.

Larsen, R., Fjaeran, T., and Skarpnes, O., 1993, Hydrocarbon potential of the Norwegian Barents Sea based on recent well results.

Larssen, G., Elvebakk, G., Henriksen, L. B., Kristensen, S., Nilsson, I., Samuelsberg, T., Svånå, T., Stemmerik, L., and Worsley, D., 2002, Upper Palaeozoic lithostratigraphy of the Southern Norwegian Barents Sea: Norwegian Petroleum Directorate Bulletin, v. 9, p. 76.

Marcussen, Ø., Maast, T. E., Mondol, N. H., Jahren, J., and Bjørlykke, K., 2010, Changes in physical properties of a reservoir sandstone as a function of burial depth–The Etive Formation, northern North Sea: Marine and Petroleum Geology, v. 27, no. 8, p. 1725-1735.

Mavko, G., Mukerji, T., and Dvorkin, J., 2009, The rock physics handbook: Tools for seismic analysis of porous media, Cambridge university press.

McBride, E. F., 1989, Quartz cement in sandstones: a review: Earth-Science Reviews, v. 26, no. 1-3, p. 69-112.

Milliken, K., 2003, Late diagenesis and mass transfer in sandstone shale sequences: Treatise on geochemistry, v. 7, p. 407.

Mondol, N. H., 2009, Porosity and permeability development in mechanically compacted silt-kaolinite mixtures, SEG Technical Program Expanded Abstracts 2009, Society of Exploration Geophysicists, p. 2139-2143.

-, 2015, Well Logging: Principles, Applications and Uncertainties, Petroleum Geoscience, Springer, p. 385-425.

Mondol, N. H., Bjørlykke, K., and Jahren, J., 2008, Experimental compaction of clays: relationship between permeability and petrophysical properties in mudstones: Petroleum Geoscience, v. 14, no. 4, p. 319-337.

Mondol, N. H., Bjørlykke, K., Jahren, J., and Høeg, K., 2007, Experimental mechanical compaction of clay mineral aggregates—Changes in physical properties of mudstones during burial: Marine and Petroleum Geology, v. 24, no. 5, p. 289-311.

Mørk, A., Embry, A. F., and Weitschat, W., 1989, Triassic transgressive-regressive cycles in the Sverdrup Basin, Svalbard and the Barents Shelf, Correlation in hydrocarbon exploration, Springer, p. 113-130.

Nichols, G., 2009, Sedimentology and stratigraphy, John Wiley & Sons.

NPD, 2014, Petroleum activity on the Norwegian Continental Shelf, Norwegian Petroleum Directorate FactPages, Volume 2017.

-, 2016, Undiscovered resources Volume 2017.

Nyland, B., Jensen, L., Skagen, J., Skarpnes, O., and Vorren, T., 1992, Tertiary uplift and erosion in the Barents Sea: magnitude, timing and consequences: Tectonic Modelling and Its Implication to Petroleum Geology; Larsen, RM, Brekke, H., Larsen, BT, Talleras, E., Eds, p. 153-162.

Olaussen, S., Dalland, A., Gloppen, T., and Johannessen, E., 1984, Depositional environment and diagenesis of Jurassic reservoir sandstones in the eastern part of Troms I area, Petroleum Geology of the North European Margin, Springer, p. 61-79.

Paxton, S., Szabo, J., Ajdukiewicz, J., and Klimentidis, R., 2002, Construction of an intergranular volume compaction curve for evaluating and predicting compaction and porosity loss in rigid-grain sandstone reservoirs: AAPG bulletin, v. 86, no. 12, p. 2047-2067.

Pedersen, J. H., Karlsen, D. A., Lie, J. E., Brunstad, H., and di Primio, R., 2006, Maturity and source-rock potential of Palaeozoic sediments in the NW European Northern Permian Basin: Petroleum Geoscience, v. 12, no. 1, p. 13-28.

Peltonen, C., Marcussen, Ø., Bjørlykke, K., and Jahren, J., 2009, Clay mineral diagenesis and quartz cementation in mudstones: The effects of smectite to illite reaction on rock properties: Marine and Petroleum Geology, v. 26, no. 6, p. 887-898.

Pettijohn, F., 1957, Sedimentary rocks, FJ Pettijohn.

Pittman, E. D., and Larese, R. E., 1991, Compaction of lithic sands: experimental results and applications (1): AAPG Bulletin, v. 75, no. 8, p. 1279-1299.

Powers, M. C., 1953, A new roundness scale for sedimentary particles: Journal of Sedimentary Research, v. 23, no. 2.

Puchkov, V. N., 1997, Structure and geodynamics of the Uralian orogen: Geological Society, London, Special Publications, v. 121, no. 1, p. 201-236.

Roberts, D., 2003, The Scandinavian Caledonides: event chronology, palaeogeographic settings and likely modern analogues: Tectonophysics, v. 365, no. 1, p. 283-299.

Ronnevik, H., Beskow, B., and Jacobsen, H. P., 1982, Structural and stratigraphic evolution of the Barents Sea.

Ryseth, A., Augustson, J. H., Charnock, M., Haugerud, O., Knutsen, S.-M., Midbøe, P. S., Opsal, J. G., and Sundsbø, G., 2003, Cenozoic stratigraphy and evolution of the Sørvestsnaget Basin, southwestern Barents Sea: Norwegian Journal of Geology/Norsk Geologisk Forening, v. 83, no. 2.

Rønnevik, H., and Jacobsen, H.-P., 1984, Structural highs and basins in the western Barents Sea, Petroleum Geology of the North European Margin, Springer, p. 19-32.

Santin, C. E., Abel, M., Goldberg, K., and De Ros, L. F., 2009, PSAutomatic Detection of the Degree of Compaction in Reservoir Rocks Based on Visual Knowledge.

Sharp, J. M., and McBride, E. F., 1989, Sedimentary petrology—a guide to paleohydrogeologic analyses, example of sandstones from northwest Gulf of Mexico: Journal of Hydrology, v. 108, p. 367-386.

Skjold, L. J., van Veen, P., Kristensen, S.-E., and Rasmussen, A. R., 1998, Triassic sequence stratigraphy of the southwestern Barents Sea.

Spencer, A., Home, P., and Berglund, L., 1984, Tertiary structural development of the western Barents Shelf: Troms to Svalbard, Petroleum Geology of the North European Margin, Springer, p. 199-209.

Steel, R. J., and Worsley, D., 1984a, Petroleum Geology of the North European Margin, Graham and Trotman London, p. 109-135.

-, 1984b, Svalbard's post-Caledonian strata—an atlas of sedimentational patterns and palaeogeographic evolution, Petroleum geology of the North European margin, Springer, p. 109-135.

Szabo, J., and Paxton, S., 1991, Intergranular volume (IGV) decline curves for evaluating and predicting compaction and porosity loss in sandstones: AAPG Bulletin (American Association of Petroleum Geologists);(United States), v. 75, no. CONF-910403--.

van de Kamp, P. C., 2008, Smectite-illite-muscovite transformations, quartz dissolution, and silica release in shales: Clays and Clay Minerals, v. 56, no. 1, p. 66-81.

Walderhaug, O., 1992, Magnitude of uplift of the Stø and Nordmela Formations in the Hammerfest Basin-a diagenetic approach: Norsk Geologisk Tidsskrift, v. 72, no. 3, p. 321-323.

Walderhaug, O., 1994, Temperatures of quartz cementation in Jurassic sandstones from the Norwegian continental shelf--evidence from fluid inclusions: Journal of Sedimentary Research, v. 64, no. 2.

-, 1996, Kinetic modeling of quartz cementation and porosity loss in deeply buried sandstone reservoirs: AAPG bulletin, v. 80, no. 5, p. 731-745.

-, 2000, Modeling quartz cementation and porosity in Middle Jurassic Brent Group sandstones of the Kvitebjørn field, northern North Sea: AAPG bulletin, v. 84, no. 9, p. 1325-1339.

Wilson, M. D., and Pittman, E. D., 1977, Authigenic clays in sandstones: recognition and influence on reservoir properties and paleoenvironmental analysis: Journal of Sedimentary Research, v. 47, no. 1.

Wood, R., Edrich, S., and Hutchison, I., 1989, Influence of North Atlantic Tectonics on the Large-Scale Uplift of the Stappen High and Loppa High, Western Barents Shelf: Chapter 36: North Sea and Barents Shelf.

Worden, R., and Morad, S., 2003, Clay minerals in sandstones: controls on formation, distribution and evolution, Wiley Online Library.

Worsley, D., 2008, The post-Caledonian development of Svalbard and the western Barents Sea: Polar Research, v. 27, no. 3, p. 298-317.

Worsley, D., Johansen, R., and Kristensen, S., 1988, The mesozoic and cenozoic succession of Tromsøflaket: A lithostratigraphic scheme for the Mesozoic and Cenozoic succession offshore mid-and northern Norway. Norwegian Petroleum Directorate Bulletin, v. 4, p. 42-65.

Yin, H., Nur, A., and Mavko, G., Critical porosity—a physical boundary in poroelasticity, *in* Proceedings International journal of rock mechanics and mining sciences & geomechanics abstracts1993, Volume 30, Elsevier, p. 805-808.

Ziegler, P. A., 1988, Evolution of the Arctic-North Atlantic and the Western Tethys: A visual presentation of a series of Paleogeographic-Paleotectonic maps: AAPG memoir, v. 43, p. 164-196.

Appendices

Appendix-1A

Sediment core logging from the Stø interval of well 7119/9-1

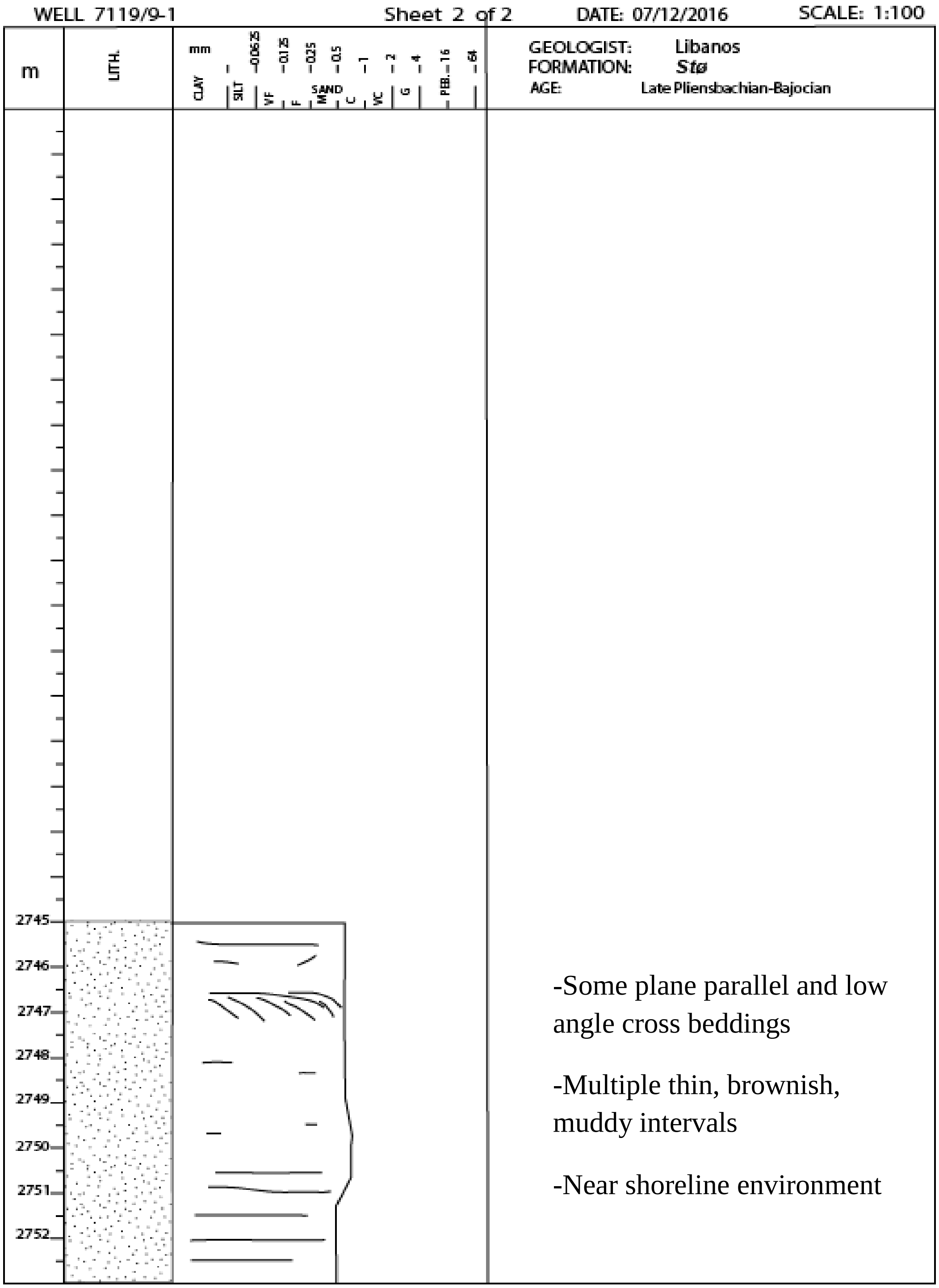
WELL 7119/9-1 Sheet 2 of 2 DATE: 07/12/2016 SCALE: 1:100

GEOLOGIST: Libanos
FORMATION: **Stø**
AGE: Late Pliensbachian-Bajocian

-Some plane parallel and low angle cross beddings

-Multiple thin, brownish, muddy intervals

-Near shoreline environment

WELL 7119/9-1 Sheet 1 of 2 DATE: 07/12/2016 SCALE: 1:100

GEOLOGIST: Libanos
FORMATION: *Stø*
AGE: Late Pliensbachian-Bajocian

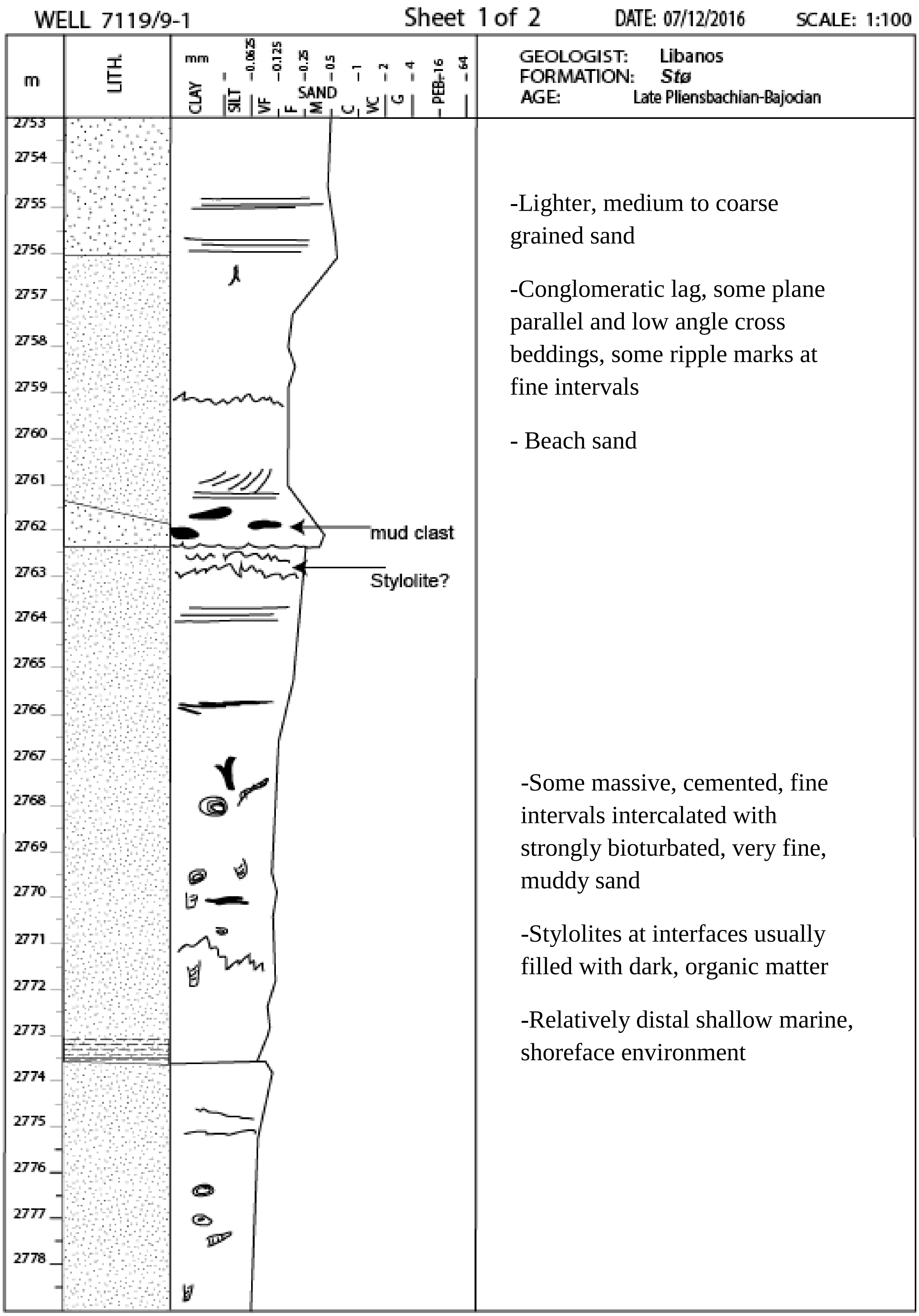

-Lighter, medium to coarse grained sand

-Conglomeratic lag, some plane parallel and low angle cross beddings, some ripple marks at fine intervals

- Beach sand

-Some massive, cemented, fine intervals intercalated with strongly bioturbated, very fine, muddy sand

-Stylolites at interfaces usually filled with dark, organic matter

-Relatively distal shallow marine, shoreface environment

Appendix 1B

Sediment core logging from the Stø interval of well 7119/12-2

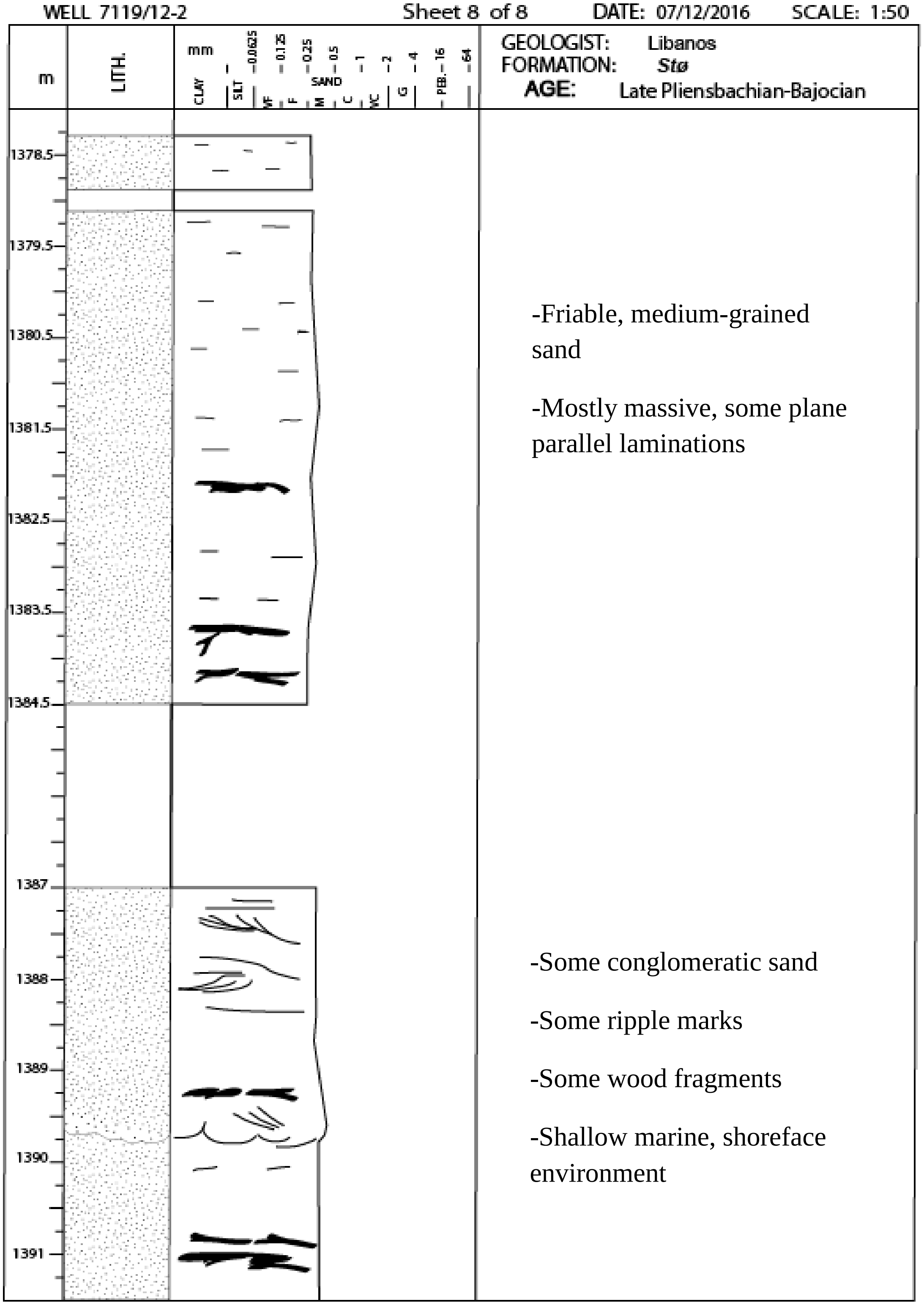

WELL 7119/12-2 Sheet 8 of 8 DATE: 07/12/2016 SCALE: 1:50

GEOLOGIST: Libanos

FORMATION: *Stø*

AGE: Late Pliensbachian-Bajocian

-Friable, medium-grained sand

-Mostly massive, some plane parallel laminations

-Some conglomeratic sand

-Some ripple marks

-Some wood fragments

-Shallow marine, shoreface environment

WELL 7119/12-2 Sheet 7 of 8 DATE: 07/12/2016 SCALE: 1:50

GEOLOGIST: Libanos
FORMATION: *Stø*
AGE: Late Pliensbachian-Bajocian

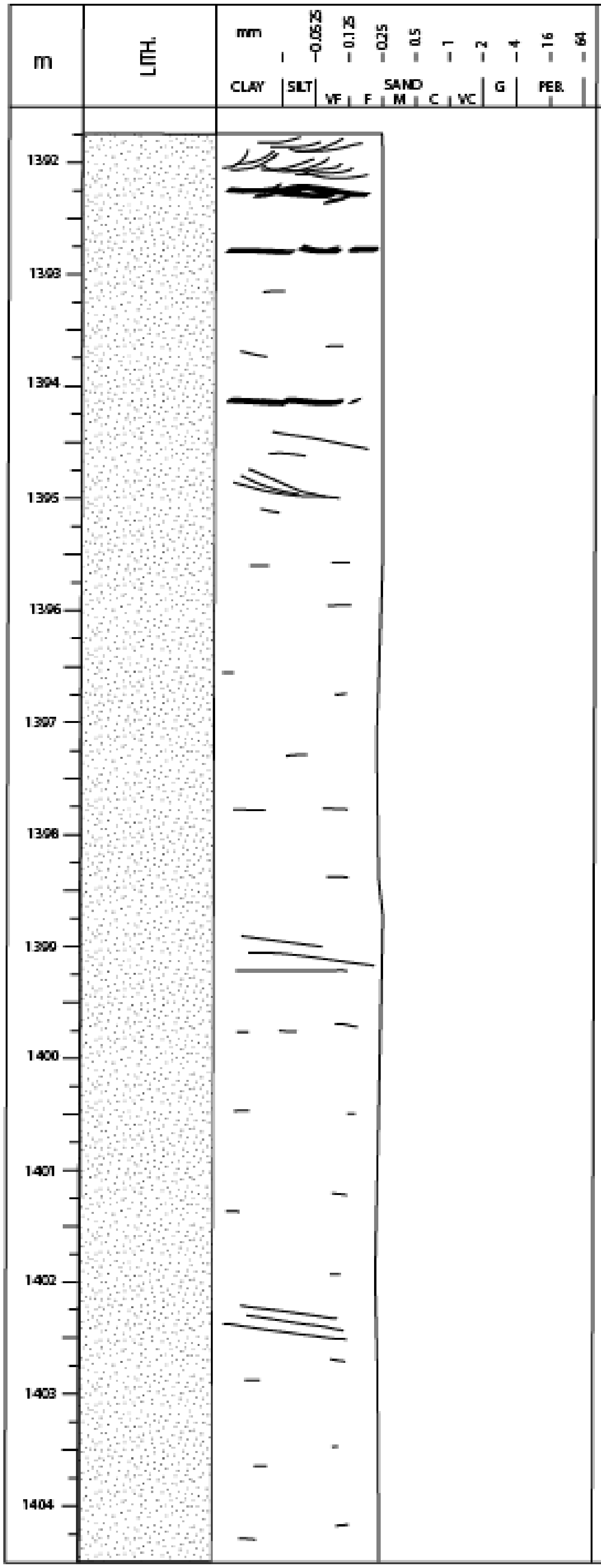

-Lighter, fine to medium sand

-Mostly massive with some plane parallel and low angle laminations, some planar and trough ripple marks

-Near shoreline environment

WELL 7119/12-2 SHEET 6 OF 8 DATE: 07/12/2016 SCALE: 1:50

GEOLOGIST: Libanos
FORMATION: *Stø*
AGE: Late Pliensbachian-Bajocian

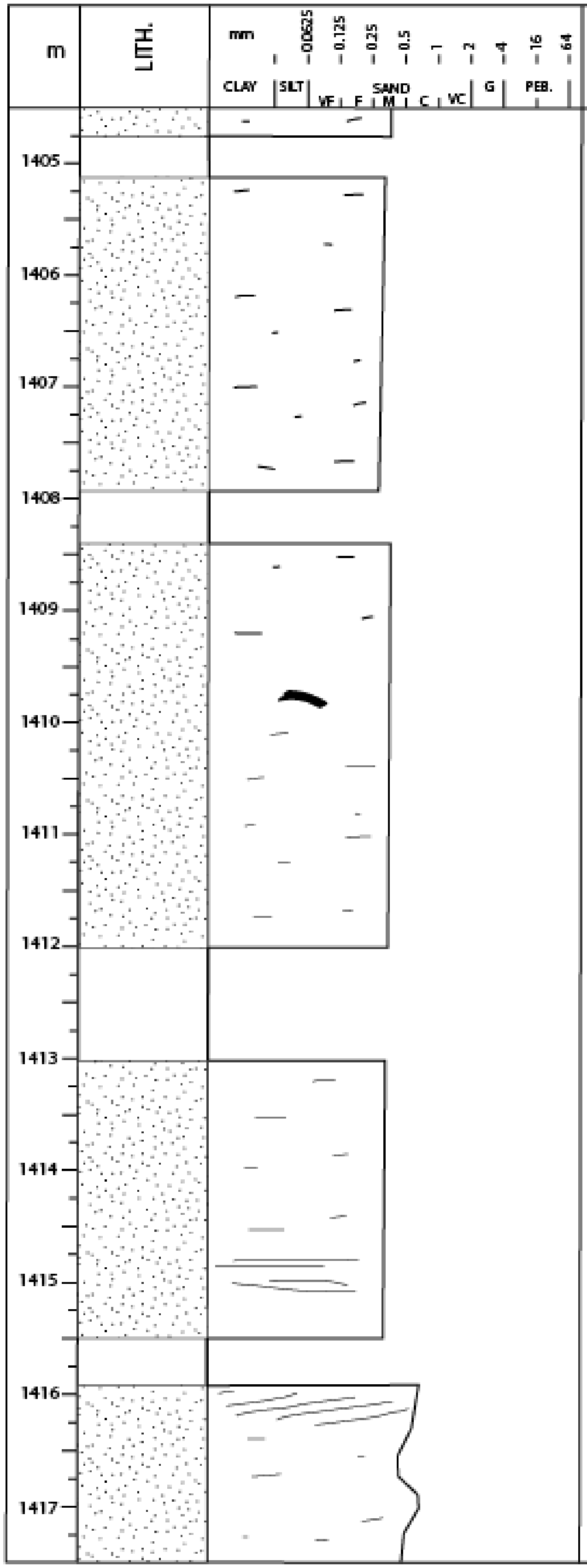

-Mostly massive, friable, medium grained sand

-Some plane parallel laminations, ripple marks

-Near shoreline environment

-Some plane parallel and low angle cross laminations

-Some conglomeratic lag

-Beach sand

WELL: 7119/12-2 Sheet 5 of 8 DATE: 07/12/2016 SCALE: 1:50

GEOLOGIST: Libanos
FORMATION: Stø
AGE: Late Pliensbachian-Bajocian

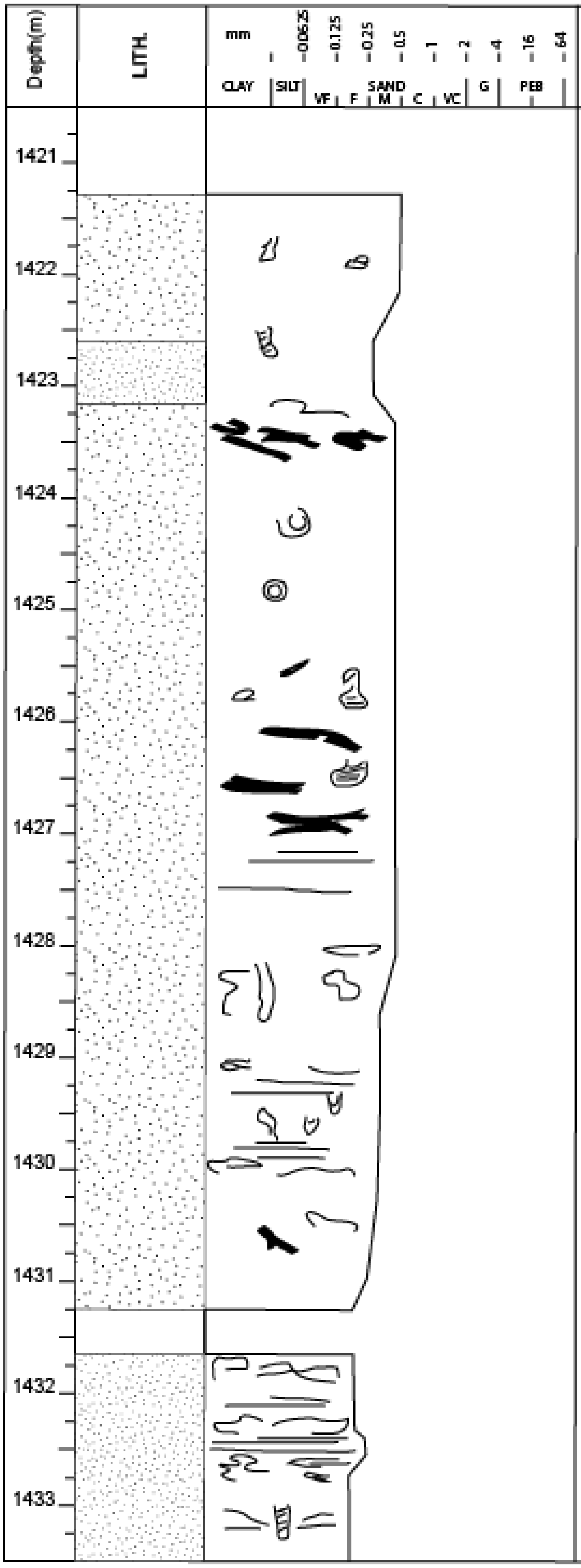

L-lighter, mostly massive, medium grained sand

-Hard shell fragments,

-Some bioturbation (burrows)

-Limited lane parallel laminations

-Near shoreline shoreface environment

-Intermediate bioturbation, fine sand interval

-Some preserved plane parallel laminations, wavy beddings

-Proximal shoreface environment

WELL: 7119/12-2 Sheet 4 of 8 DATE: *07/12/2016* SCALE: 1:50

GEOLOGIST: Libanos
FORMATION: ***Stø***
AGE: Late Pliensbachian-Bajocian

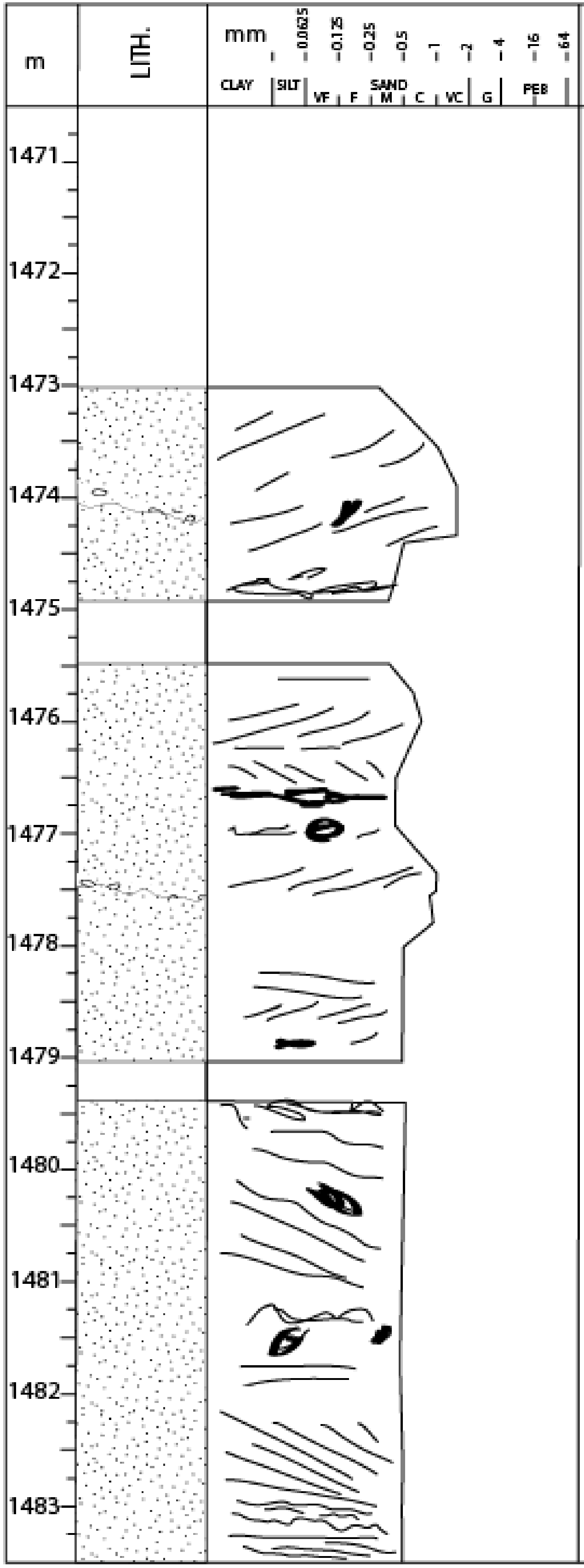

-Cross beddings, mud and organic drapes

-Some bioturbation (burrows), wood fragments

-Distributary channel fill

-River influence

-Shoreface environment

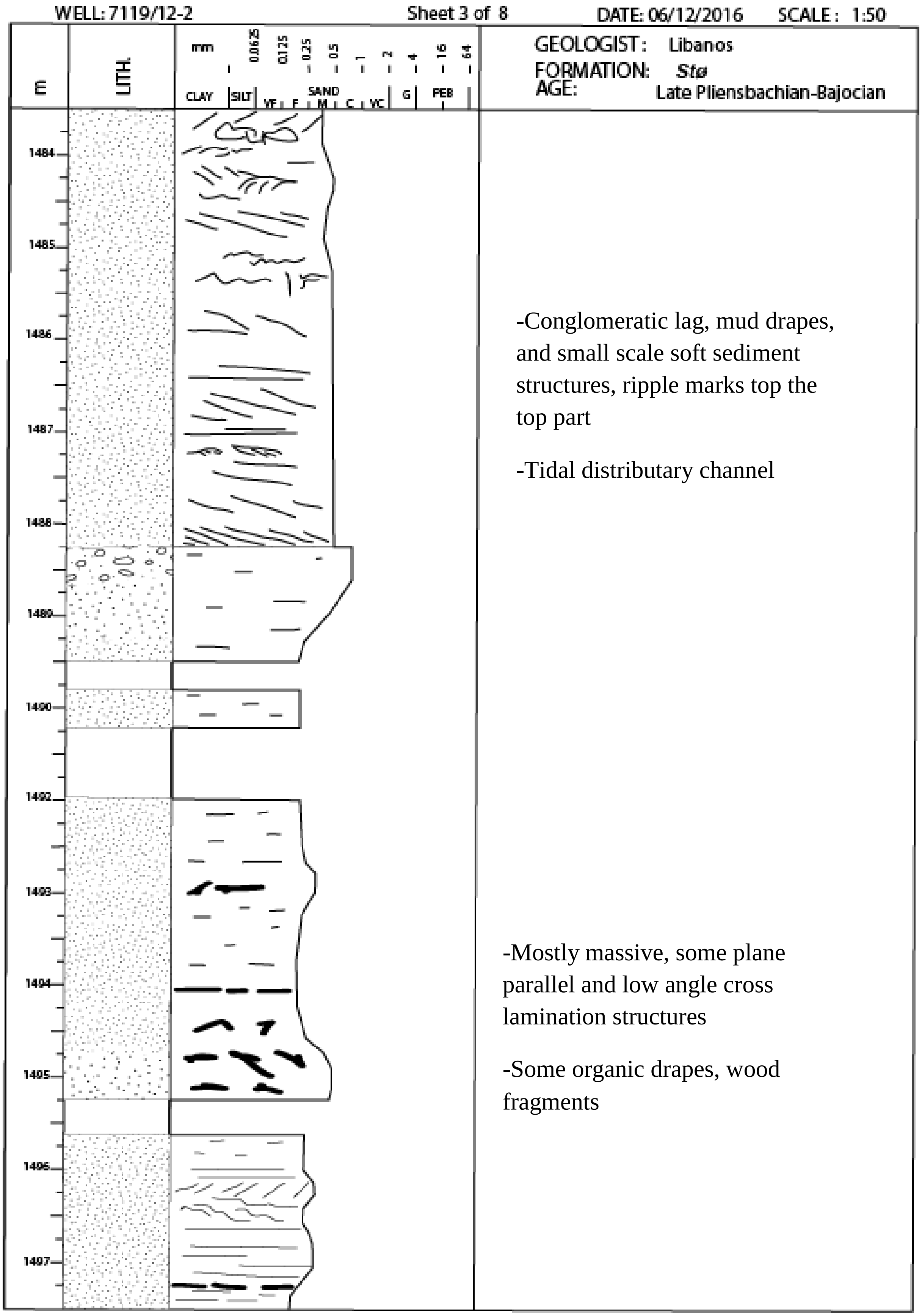

-Conglomeratic lag, mud drapes, and small scale soft sediment structures, ripple marks top the top part

-Tidal distributary channel

-Mostly massive, some plane parallel and low angle cross lamination structures

-Some organic drapes, wood fragments

WELL: 7119/12-2 Sheet 2 of 8 DATE: 06/12/2016 SCALE: 1:50

GEOLOGIST: Libanos
FORMATION: *Stø*
AGE: *Late Pliensbachian-Bajocian*

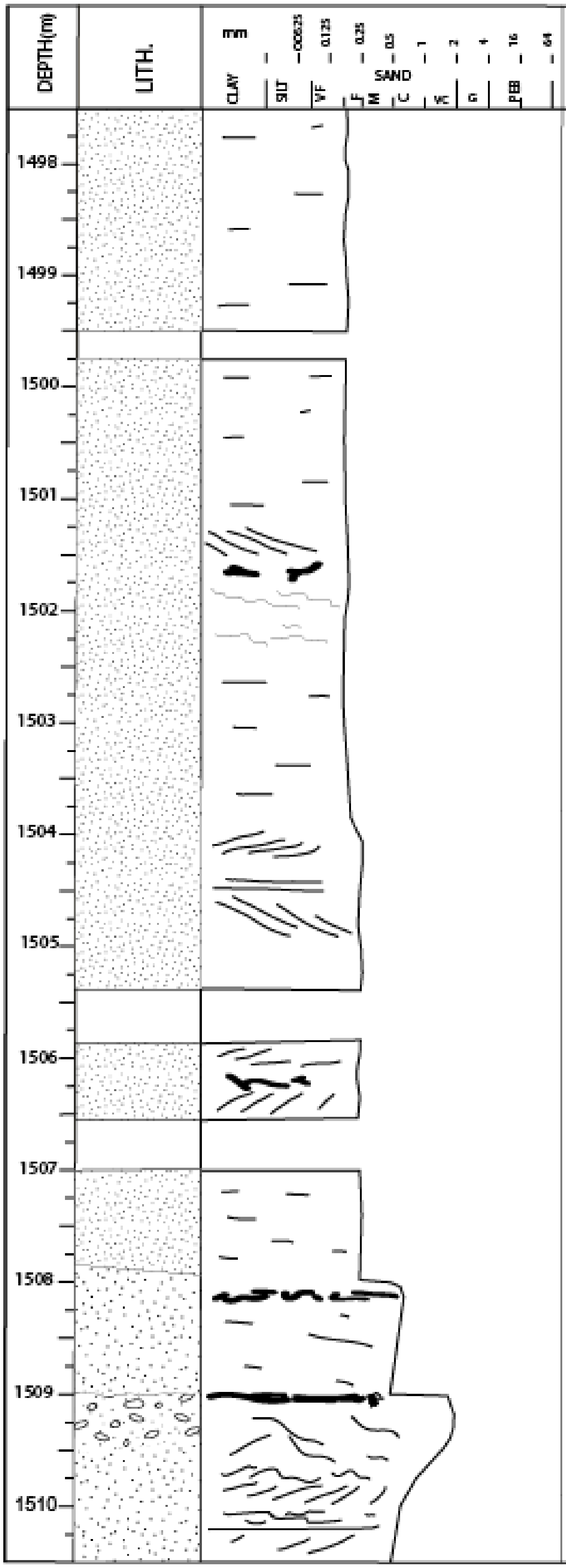

-Lighter, friable, massive, fine sand

-Some plane parallel and cross lamination structures

-Some wood fragments, organic drapes

-Friable, loose sand, organic and mud drapes, wood fragments

-Cross laminations sedimentary structures

WELL: 7119/12-2 Sheet 1 of 8 DATE: 06/12/2016 SCALE: 1:50

GEOLOGIST: Libanos
FORMATION: *Stø*
AGE: Late Pliensbachian-Bajocian

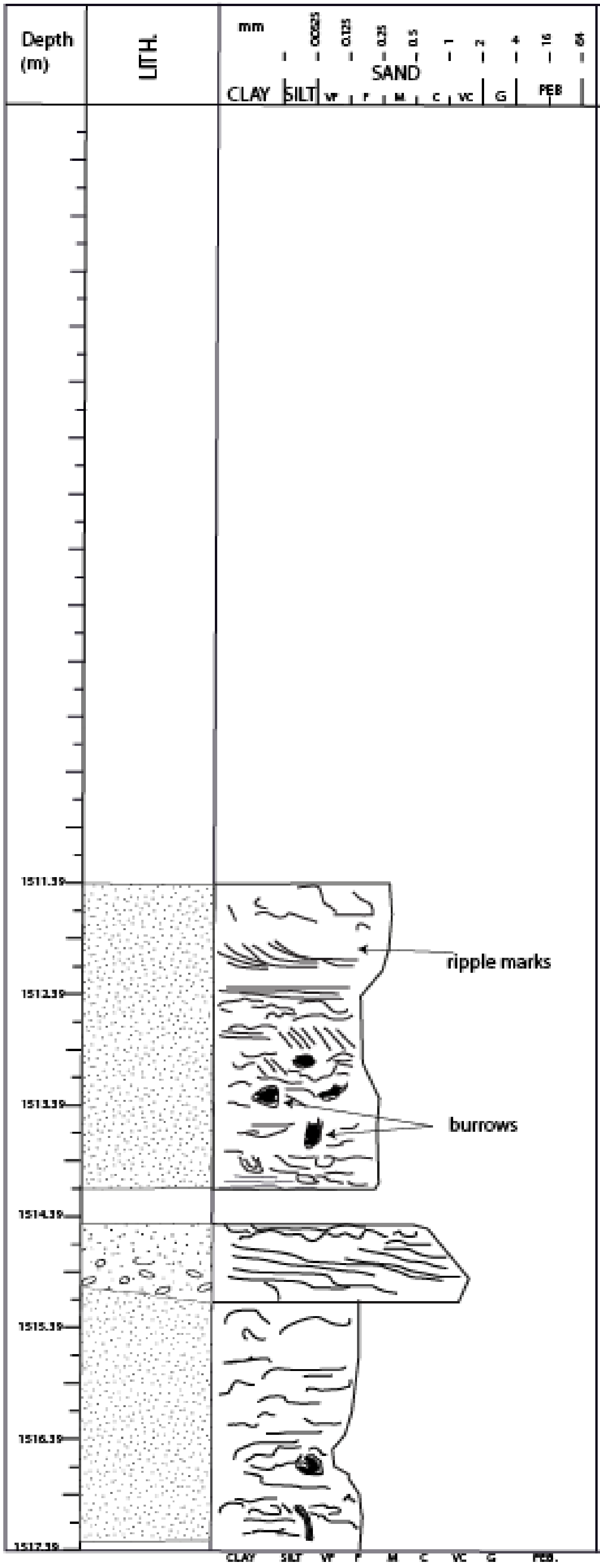

-Fine to medium-grained sand, mud drapes, plane parallel and low angle cross laminations, ripple marks, and some bioturbation

- Tidal influence shoreface environment

-Intermediate bioturbation, fine sand

-Mud drapes, wavy laminations,

Appendix-2

Petrographic point counted results based on thin sections inspection from both wells.

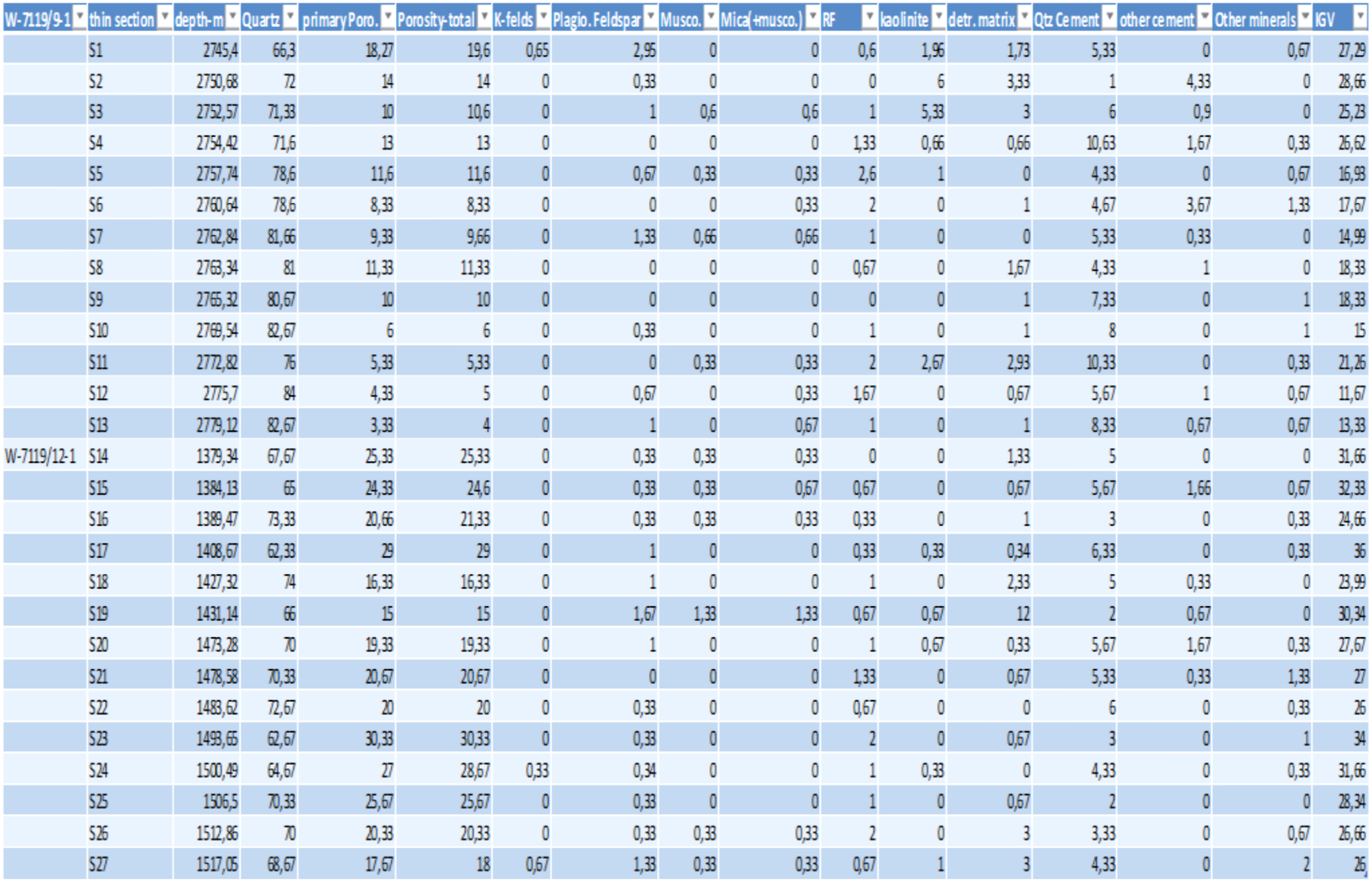

W-7119/9-1	thin section	depth-m	Quartz	primary Poro.	Porosity-total	K-felds	Plagio. Feldspar	Musco.	Mica(+musco.)	RF	kaolinite	detr. matrix	Qtz Cement	other cement	Other minerals	IGV
	S1	2745,4	66,3	18,27	19,6	0,65	2,95	0	0	0,6	1,96	1,73	5,33	0	0,67	27,29
	S2	2750,68	72	14	14	0	0,33	0	0	0	6	3,33	1	4,33	0	28,66
	S3	2752,57	71,33	10	10,6	0	1	0,6	0,6	1	5,33	3	6	0,9	0	25,23
	S4	2754,42	71,6	13	13	0	0	0	0	1,33	0,66	0,66	10,63	1,67	0,33	26,62
	S5	2757,74	78,6	11,6	11,6	0	0,67	0,33	0,33	2,6	1	0	4,33	0	0,67	16,93
	S6	2760,64	78,6	8,33	8,33	0	0	0	0,33	2	0	1	4,67	3,67	1,33	17,67
	S7	2762,84	81,66	9,33	9,66	0	1,33	0,66	0,66	1	0	0	5,33	0,33	0	14,99
	S8	2763,34	81	11,33	11,33	0	0	0	0	0,67	0	1,67	4,33	1	0	18,33
	S9	2765,32	80,67	10	10	0	0	0	0	0	0	1	7,33	0	1	18,33
	S10	2769,54	82,67	6	6	0	0,33	0	0	1	0	1	8	0	1	15
	S11	2772,82	76	5,33	5,33	0	0	0,33	0,33	2	2,67	2,93	10,33	0	0,33	21,26
	S12	2775,7	84	4,33	5	0	0,67	0	0,33	1,67	0	0,67	5,67	1	0,67	11,67
	S13	2779,12	82,67	3,33	4	0	1	0	0,67	1	0	1	8,33	0,67	0,67	13,33
W-7119/12-1	S14	1379,34	67,67	25,33	25,33	0	0,33	0,33	0,33	0	0	1,33	5	0	0	31,66
	S15	1384,13	65	24,33	24,6	0	0,33	0,33	0,67	0,67	0	0,67	5,67	1,66	0,67	32,33
	S16	1389,47	73,33	20,66	21,33	0	0,33	0,33	0,33	0,33	0	1	3	0	0,33	24,66
	S17	1408,67	62,33	29	29	0	1	0	0	0,33	0,33	0,34	6,33	0	0,33	36
	S18	1427,32	74	16,33	16,33	0	1	0	0	1	0	2,33	5	0,33	0	23,99
	S19	1431,14	66	15	15	0	1,67	1,33	1,33	0,67	0,67	12	2	0,67	0	30,34
	S20	1473,28	70	19,33	19,33	0	1	0	0	1	0,67	0,33	5,67	1,67	0,33	27,67
	S21	1478,58	70,33	20,67	20,67	0	0	0	0	1,33	0	0,67	5,33	0,33	1,33	27
	S22	1483,62	72,67	20	20	0	0,33	0	0	0,67	0	0	6	0	0,33	26
	S23	1493,65	62,67	30,33	30,33	0	0,33	0	0	2	0	0,67	3	0	1	34
	S24	1500,49	64,67	27	28,67	0,33	0,34	0	0	1	0,33	0	4,33	0	0,33	31,66
	S25	1506,5	70,33	25,67	25,67	0	0,33	0	0	1	0	0,67	2	0	0	28,34
	S26	1512,86	70	20,33	20,33	0	0,33	0,33	0,33	2	0	3	3,33	0	0,67	26,66
	S27	1517,05	68,67	17,67	18	0,67	1,33	0,33	0,33	0,67	1	3	4,33	0	2	26,

***** X-ray diffraction pattern of powder samples analyzed for bulk mineral composition

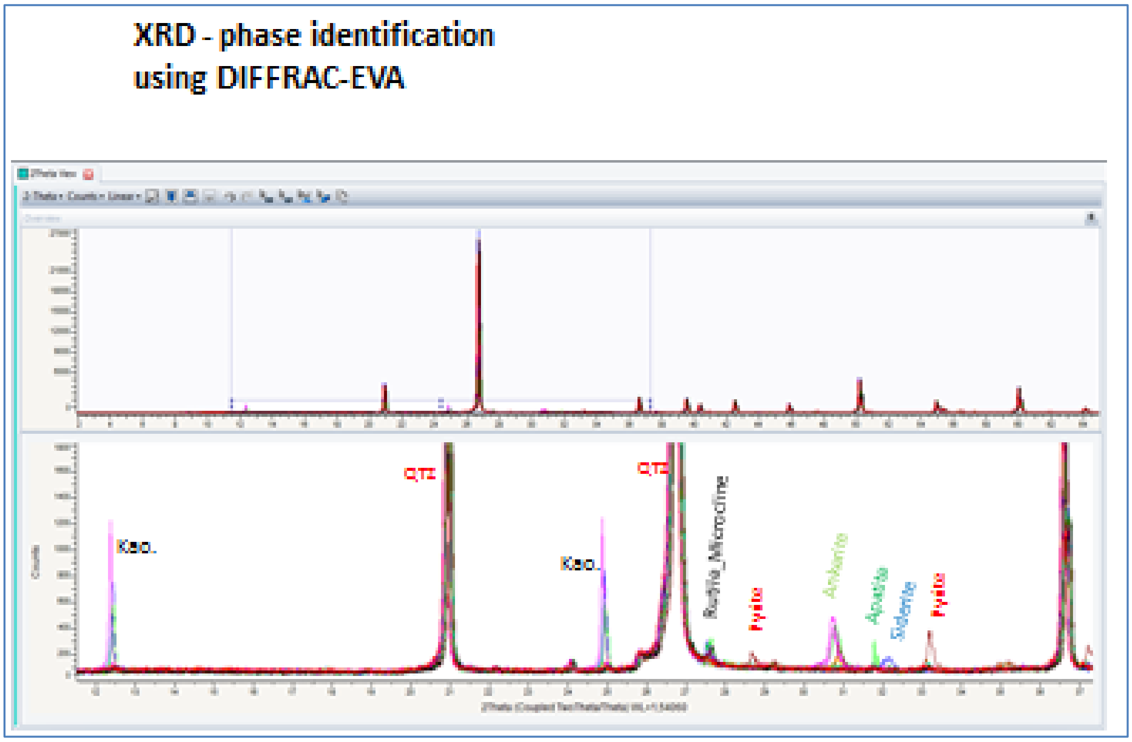

XRD - phase identification using DIFFRAC-EVA

.